Mesoscopic modeling and simulation on the forming process of textile composites

Dawei Wang

To cite this version:

Dawei Wang. Mesoscopic modeling and simulation on the forming process of textile composites. Materials. Université de Lyon, 2016. English. NNT : 2016LYSEI108 . tel-01974016

HAL Id: tel-01974016
https://theses.hal.science/tel-01974016v1

Submitted on 8 Jan 2019

N°d'ordre NNT : 2016LYSEI108

THÈSE de DOCTORAT DE L'UNIVERSITÉ DE LYON

préparée au sein de
l'Institut National des Sciences Appliquées de Lyon

École Doctorale 162
Mécanique, Énergétique, Génie civil, Acoustique

Spécialité de doctorat
MÉCANIQUE

Soutenue publiquement le 03 Novembre 2016, par :

Dawei WANG

MESOSCOPIC MODELING AND SIMULATION ON THE FORMING PROCESS OF TEXTILE COMPOSITES

(MODELISATION ET SIMULATION A L'ECHELLE MESOSCOPIQUE DE LA MISE EN FORME DE RENFORTS COMPOSITE)

Devant le jury composé de :

P. BOISSE	Professeur (INSA de Lyon)	Directeur
F. BOUSSU	Professeur (Ensait de Roubaix)	Rapporteur
M. BUENO	Professeur (Université de Mulhouse)	Rapporteur
N. NAOUAR	Chargé de Recherches CNRS (INSA de Lyon)	Examinateur
O. POLIT	Professeur (Université Paris 10-Nanterre)	Examinateur
E. VIDAL-SALLE	Professeur (INSA de Lyon)	Examinateur

Département FEDORA - INSA Lyon - Ecoles Doctorales - Quinquennal 2016-2020

SIGLE	ÉCOLE DOCTORALE	NOM ET COORDONNÉES DU RESPONSABLE
CHIMIE	**CHIMIE DE LYON** http ://www.edchimie-lyon.fr Sec. : Renée EL MELHEM Bâtiment Blaise Pascal 3$^{\text{ème}}$ étage 04.72.43.80.46 Insa : R. GOURDON secretariat@edchimie-lyon.fr	**M. Stéphane DANIELE** Institut de Recherches sur la Catalyse et l'Environnement de Lyon IRCELYON-UMR 5256 Équipe CDFA 2 avenue Albert Einstein 69626 Villeurbanne cedex directeur@edchimie-lyon.fr
E.E.A.	**ÉLECTRONIQUE, ÉLECTROTECHNIQUE, AUTOMATIQUE** http ://edeea.ec-lyon.fr Sec. : M.C. HAVGOUDOUKIAN eea@ec-lyon.fr	**M. Gérard SCORLETTI** École Centrale de Lyon 36 avenue Guy de Collongue 69134 ECULLY Tél. : 04.72.18 60.97 Fax : 04.78.43.37.17 Gerard.scorletti@ec-lyon.fr
E2M2	**EVOLUTION, ECOSYSTEME, MICROBIOLOGIE, MODÉLISATION** http ://e2m2.universite-lyon.fr Sec. : Bâtiment Atrium- UCB Lyon 1 Tél. : 04.72.44.83.62 Insa : S. REVERCHON secretariat.e2m2@univ-lyon1.fr	**Mme Gudrun BORNETTE** CNRS UMR 5023 LEHNA Université Claude Bernard Lyon 1 Bât Forel 43 bd du 11 novembre 1918 69622 VILLEURBANNE Cédex Tél : 06.07.53.89.13 e2m2@ univ-lyon1.fr
EDISS	**INTERDISCIPLINAIRE SCIENCES-SANTE** http ://www.ediss-lyon.fr Sec. : Safia AIT CHALAL Bâtiment Atrium - UCB Lyon 1 Tél. : 04.72.44.83.62 Insa : M. LAGARDE Safia.ait-chalal@univ-lyon1.fr	**Mme Emmanuelle CANET-SOULAS** INSERM U1060, CarMeN lab, Univ. Lyon 1 Bâtiment IMBL 11 avenue Jean Capelle INSA de Lyon 69621 VILLEURBANNE Tél. : 04.72.68.49.09 Fax : 04.72.68.49.16 Emmanuelle.canet@univ-lyon1.fr
INFOMATHS	**INFORMATIQUE ET MATHÉMATIQUES** http ://infomaths.univ-lyon1.fr Sec. : Renée EL MELHEM Bâtiment Blaise Pascal 3$^{\text{ème}}$ étage infomaths@univ-lyon1.fr	**Mme Sylvie CALABRETTO** LIRIS - INSA de Lyon Bat Blaise Pascal 7 avenue Jean Capelle 69622 VILLEURBANNE Cedex Tél. : 04.72.43.80.46 Fax : 04.72.43.16.87 Sylvie.calabretto@insa-lyon.fr
Matériaux	**MATÉRIAUX DE LYON** http ://ed34.universite-lyon.fr Sec. : M. LABOUNE PM : 71.70 Fax : 87.12 Bâtiment Saint-Exupéry Ed.materiaux@insa-lyon.fr	**M. Jean-Yves BUFFIERE** INSA de Lyon MATEIS Bâtiment Saint-Exupéry 7 avenue Jean Capelle 69621 VILLEURBANNE Cedex Tél. : 04.72.43.71.70 Fax : 04.72.43.85.28 Ed.materiaux@insa-lyon.fr
MEGA	**MÉCANIQUE, ÉNERGÉTIQUE, GÉNIE CIVIL, ACOUSTIQUE** http ://edmega.universite-lyon.fr/ Sec. : M. LABOUNE PM : 71.70 Fax : 87.12 Bâtiment Saint-Exupéry mega@insa-lyon.fr	**M. Philippe BOISSE** INSA de Lyon Laboratoire LAMCOS Bâtiment Jacquard 25 bis avenue Jean Capelle 69621 VILLEURBANNE Cedex Tél. : 04.72.43.71.70 Fax : 04.72.43.72.37 Philippe.boisse@insa-lyon.fr
ScSo	**ScSo**[*] http ://recherche.univ-lyon2.fr/scso/ Sec. : Viviane POLSINELLI Sec. : Brigitte DUBOIS Insa : J.Y. TOUSSAINT viviane.polsinelli@univ-lyon2.fr	**Mme Isabelle VON BUELTZINGLOEWEN** Université Lyon 2 86 rue Pasteur 69365 LYON Cedex 07 Tél. : 04.78.77.23.86 Fax : 04.37.28.04.48

[*] ScSo : Histoire, Géographie, Aménagement, Urbanisme, Archéologie, Science politique, Sociologie, Anthropologie

Acknowledgment

At the end of my Ph.D study, I would like to thank those people who made this thesis possible and give me this unforgettable experience.

Foremost, I would like to express my sincere gratitude to my supervisor Professor Philippe BOISSE for the support of my Ph.D study and research, for his patience and immense knowledge. I am really grateful for his effort to guide me in the scientific field.

I would like to thank Professor Emmanuelle VIDAL-SALLE and Dr. Naim NAOUAR who helped me in my research process. Appreciation should be also going to Jérome ADRIEN, Philippe CHAUDET and Paul VALVERDE who offered me the help on experiments.

I am thankful to my colleague and friend Ismael AZEHAF, for the experience sharing of work and life in the past three years. I am very grateful to my fellow labmates : Julien COLMARS, Charlotte FLORIMOND, SaSa GAO, Eduardo GUZMAN MALDONADO, Nahiene HAMILA, Biao LIANG, Sylvain MATHIEU, Quentin STEER, Anh Tuan TA, Jie WANG, Hu XIONG, Wenfeng YE, Lv ZHAO, for the stimulating discussions and all the fun we have had in the last three years.

I acknowledge the financial support provided by China Scholarship Council (CSC) in pursuing my PhD study in France. I also pay thanks to my research laboratory, LaMCoS, Insa de Lyon, for the financial and technical support.

Last but not the least, I would like to thank my family : my parents Peixian WANG and Cuixiu ZHANG, as well as my sister Yajie WANG, who are always there to support me.

Abstract

This thesis is devoted to the mesoscopic study on the performance of textile reinforcements. F.E. simulation is carried out on a mesoscale model for the fibrous material, based on which two kinds of new deformation modes are developed. The first one is a longitudinal compression mode, which is used to reflect the small stiffness when the yarn is compressed longitudinally. The incompatibility problem between the small longitudinal compression stiffness and the large tension stiffness are solved by three different strategies : constraining the critical step time, adding the nonlinear tension part, or using a new strategy to update the stress. The second one is transverse expansion mode that could reflect the influence from longitudinal deformation to transverse deformation. This deformation could be found in tomography view but was ignored by the former researches. An experiment is designed to measure the expansion magnitude, and the geometrical inverse fitting process is applied to measure the value of the longitudinal-transverse Poisson ratio. The parameters of the mesoscale model are measured by a series of mechanical experiments and the simulation results are verified by the tomography methodology.

KEYWORDS: Composites, textile reinforcements, forming process, mechanical properties, finite element method, mesoscopic modeling, hypo elastic, tomography, longitudinal compression, transverse expansion

Résumé

Ce travail de thèse est consacré à l'étude des renforts textiles techniques 2D à l'échelle mésoscopique. La méthode des éléments finis est utilisée pour résoudre un problème aux limites, fortement non linéaire, dans le domaine du renfort fibreux. Deux nouveaux modes de déformations pour le comportement des mèches de renforts ont été développés et caractérisés. Le premier mode est la compression longitudinale, qui permet de traduire la faible rigidité des mèches lorsqu'elles subissent une dilatation négative dans le sens des fibres. La relation conflictuelle sur le plan numérique entre la rigidité en tension, très forte, et la rigidité en compression longitudinale, très faible, peut être résolue via trois méthodes : réduction du pas de temps critique, addition de la contribution en tension ou avec une nouvelle stratégie pour l'actualisation du champ de contrainte. Le second mode de déformation est la dilatation transversale des mèches considérée comme conséquence directe de la compression longitudinale. Ce phénomène d'expansion de matière dans les directions transverses peut être observé avec un essai de compression longitudinale in-situ sous tomographie X et est communément ignorer. Un protocole expérimental a été mise en place pour mesurer cette dilatation transversale des mèches et un coefficient de Poisson a pu être caractérisé par identification inverse. Une campagne expérimentale a permis d'identifier les paramètres matériau du modèle mésoscopique et les résultats de simulations sont comparés aux images issues d'essai mécanique in situ sous tomographe.

MOTS CLÉS : Composites, renforts tissés, mise en forme, propriétés mécaniques, méthode par éléments finis, modélisation mésoscopique, hypoélasticité, tomographie, compression longitudinale, dilatation transversale

Table des matières

Table des figures

Liste des tableaux

Chapitre 1

Introduction

This chapter gives the introduction of composite. The definition of composite and textile reinforcement, as well as several common used matrix are introduced in section 1.1. An unbalanced woven composite which is called tapas fabric is chosen as an example to introduce the most important mechanical properties of textile reinforcement (tension, in-plane shear, compaction etc.). The mechanical characteristic of this fabric is well exhibited, and will be used in the following chapters. At last the well known numerical approaches, including kinematic and Finite Element (F.E.) simulation for composite are briefly mentioned in section 1.4.

Contents

1.1 Introduction to composite material

1.1.1 Definition of composite material

(a) Mud bricks **(b)** Aero engine blade

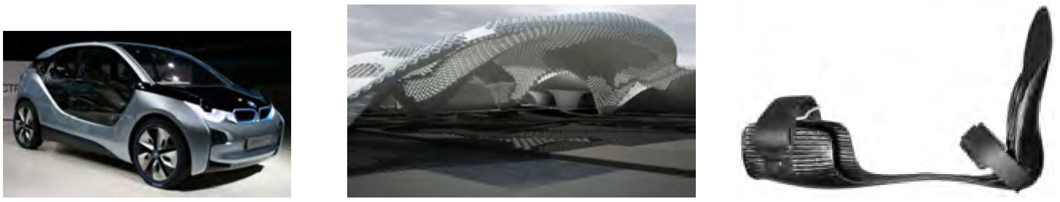

(c) Composite-body BMW i3 [BIR 13] **(d)** Construction [MIN 10] **(e)** Leg protector

FIGURE 1.1 – The applications of composites in multiply fields

According to the commonly acceptable definition, the material made up of several different continuous materials is called composite material or composite. This definition is so broad that even the brick with straw fibers (FIG. 1.1a) can be classified as an ancient composite. The combination of different materials brings composite specific benefits, such as large strength-weight ratio, the resistance to corrosion or sometimes the capability to dampen vibrations, *etc.* All these result in the explosive growth in the demand of composite, not only in aeronautic or automotive area (the BMW i3 in FIG. 1.1c is the first mass produced composite car in production, and it is made from dry, carbon non-crimp fabric preforms that are resin transfer molded [SLO 14]), but also for construction industry and even the domain of medicine. Composite has a large family, and we are interested in those composites consisting of reinforcement (loading bearing constituent) and matrix (constraining the relative movement of reinforcement).

1.1.2 Types of reinforcement

Reinforcements mainly come in three geometries : continuous fiber, discontinuous fiber and particulate. The arrangement of these fibers is of utmost importance for the mechanical performance of composite. The continuous fibers are usually arranged in one direction or two perpendicular directions, but more complex arrangements also exist ; the discontinuous ones are short, they are distributed in the matrix randomly or regularly ; for the particulates, their shapes can be spherical or sheet, regular or irregular while their

Material	Young's modulus (GPa)	Tensile strength (GPa)	Density (g/cm^3)
E-Glass	80	2	2.55
S-Glass	90	4.8	2.5
Alumina	300	2	3.3
Carbon	$200 \sim 800$	2.9	2

TABLE 1.1 – Properties of common material for fibers

distribution may be random or rhythmic. All these kinds of reinforcements are created from sources such as glass, carbon and aramid, which are favored in different occasions in light of their own advantages and disadvantages. *E.g.* glass fiber is low cost and has an outstanding ability to stretch, thus is useful for flexible applications such as snowboards, helicopter blades and ballistics where high impact damage exist. Carbon fiber is stiffer and stronger, and is conductive electrically and thermally. Moreover, the size of carbon fiber does not change with temperature, while the glass fiber does. The major pain for carbon fiber is the high cost, roughly 10 times more expensive than glass fiber. Similar with carbon fiber, aramid fiber is thermally stable in dimensions, but has better resistance to impact and abrasion damage. Nonetheless, it absorbs moisture thus is sensitive to the environment.

This thesis concerns the properties of the textile reinforcement. In most cases, the fibers and yarns are not straight arranged in the fabric, and the waviness of a fiber is described by the term crimp. It is defined as the difference between the straightened yarn length and the distance between the ends of the yarn while in the fabric :

$$C = \frac{L_y - L_f}{L_f} \tag{1.1}$$

where C is the crimp value, L_y is the length of straightened yarn and L_f is the corresponding length of fabric. Crimp concerns the stability of the fabric. *E.g.*, small crimp value normally leads to a loose and unstable structure but improves the mechanical properties of the fabric. Moreover, crimp also influences the drapability and permeability[ARB 11] of the fabric. The objective of this section is giving up-to-date information of the most common textile reinforcement formation such as the woven fabric, braid, knitted fabric, as well as non-woven and interlock ones.

At the mention of textile fabric, woven reinforcement is surely the first thought since it is the most traditional one. For example, the application of woven composite on cloths can be dated back to thousands of years ago. Industrial method to obtain the woven fabric is called weaving, which interlaces the yarns on the weaving machine (also called loom). Five common woven patterns are shown in FIG. 1.2.

Plain woven fabric. Plain is the simplest kind of woven style. The warp yarn and weft yarn pass over and under each other alternatively to form the whole fabric. It has

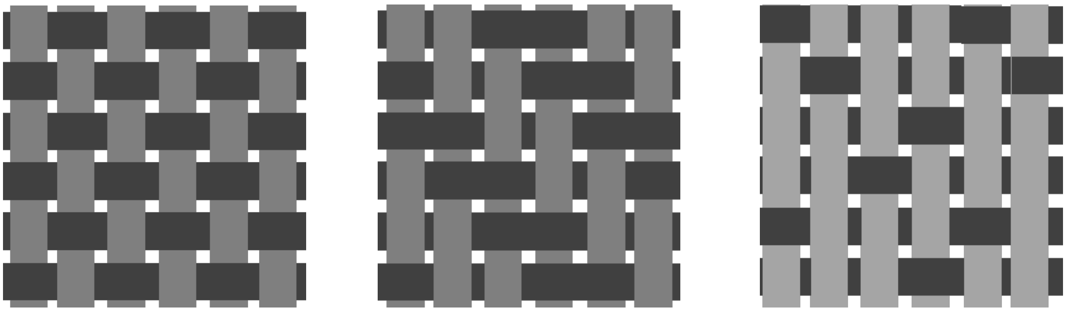

(a) Plain **(b)** Twill **(c)** Satin

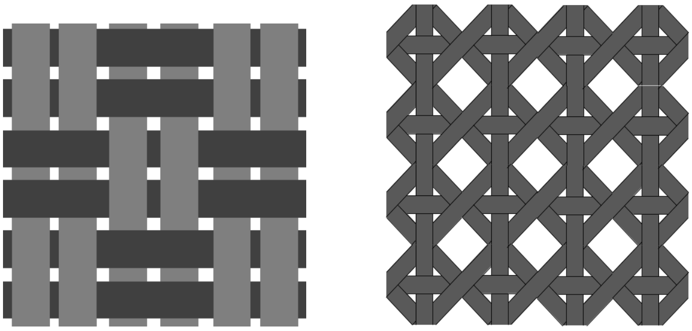

(d) Basket **(e)** Multiaxial

FIGURE 1.2 – Examples of woven fabric

quite good permeability but low mechanical properties. The high crimp in this fabric makes it quite stable, but on the other hand, quite difficult to drop.

Twill woven fabric. Twill is another common woven fabric. In a twill fabric, one or more warp yarns pass over and under more than one weft yarns regularly. The twill fabric has a reduced crimp level and smoother surface comparing with plain, so its drapability is better, and this is a notable advantage when the fabric is formed into complex shapes. Although the interlocking between warp and weft yarns are not as tight as those in plain fabric, its stability reduces just a litter bit.

Satin woven fabric. Satin is a more complex weaving style. The number of weft yarns over and under warp yarns are not balanced any more : the ratio can be as large as 8 :1. Since there are fewer intersections between orthogonal yarns, the satin is very flat. The low crimp leads to outstanding mechanical properties and drapability, but poor permeability. The largest disadvantage of satin concerns its weak stability : the interlocking level of warp and weft is too low to fix their positions. Careful attention should be paid to the slide of yarns, especially in the multilayer cases.

Other derivated weave diagrams The plain, twill and satin are three fundamental weave diagrams, but there are also some other derivated weave diagrams such as basket weave and multiaxial woven fabric.

Basket woven fabric. For those yarns or fibers with large linear density (hex) or sectional area, it is easy to have the problem of excessive crimping during weaving.

The basket can be a good choice to avoid this problem, since it provide a small crimp structure. This weaving style is quite similar with plain except that two or more warps interlace with two or more wefts. FIG. 1.2 shows an example of 2 × 2 interlacing. Similar to the discussion on satin fabric, basket also has the shortcoming of poor stability.

Multiaxial woven fabric. Multiaxial woven fabric consists of three or more yarn sets. The structure generally has large rectangular or hexagonal openings thus the volume fraction is small. Since the yarns exist in more than two directions, multiaxial structures are more stable than the biaxial ones.

Besides the woven fabric, the non-crimp fabric (NCF), knitted fabric, braid fabric and interlock fabric (FIG. 1.3) are also common used textile reinforcement in industry.

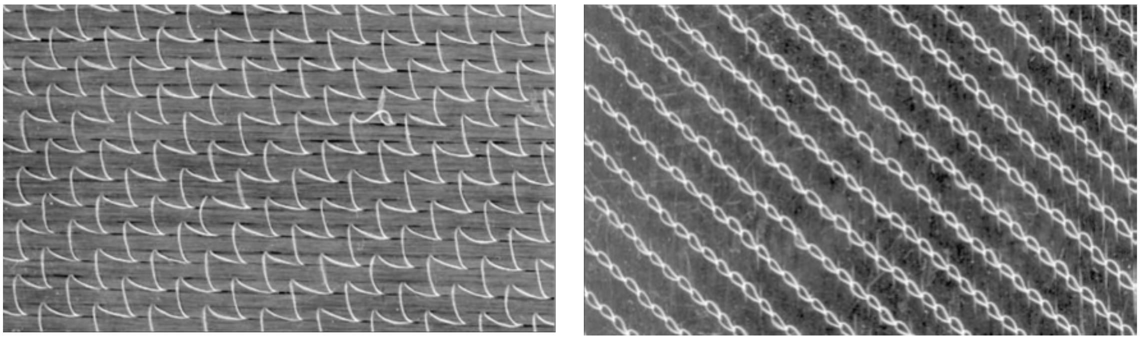

(a) Examples of Non Crimp Fabric [BEL 11]

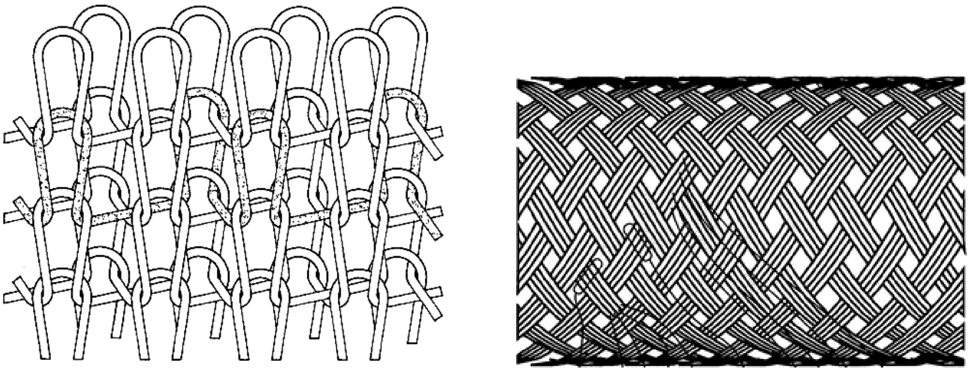

(b) Knitted fabric

(c) Braid fabric

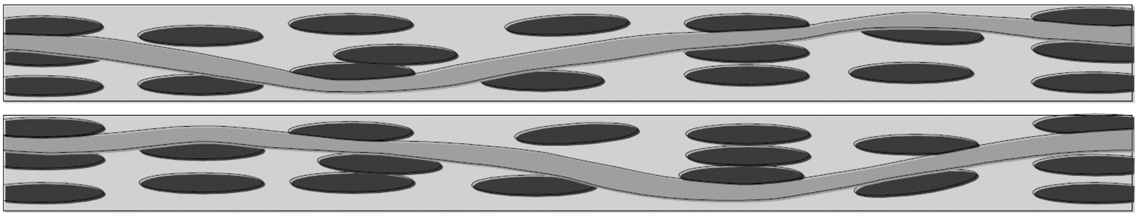

(d) The cross sections of interlock fabric G1151 of Hexcel [BAD 08b]

FIGURE 1.3 – Several common used textile fabrics

NCF. The term of non crimp implies the structural yarns in the fabric will keep straight, and they are in fact held in place by non-structural stitching threads (so this fabric is also called stitched fabric). There is no interlacement between layers which is a large advantage. Small crimp brings attractive benefits : first of all, the straight fibers allow a fluent flow and uniform distribution of resin in the fabric [ADA 87]. Less resin-poor and resin-rich areas make the structure lighter and more stable ; secondly, without obvious crimps, the fabric has better mechanical properties such as higher tensile stiffness ; thirdly, the weaving process of NCF is simpler than other kind of textile reinforcement, and the forming operations such as cutting are easier since the structure is hold together by stitching threads ; last but not the least, the smooth surface of NCF can be a significant advantage in applications.

Knitted fabric. Knitted fabric consists of yarn loops by the interloping technology. In a basic knitting type (FIG. 1.3b), a row of loops formed from a long continuous yarn can be called a course. It is connected to the previously formed course in the interloping process. The vertical columns of loops are called wale. So course and wale are two basic concept for knitted fabric, *e.g.*, the course density (number of courses per unit length along the wale direction) or wale density (number of wales per unit length along the course direction) are usually used to characterize the knitted fabrics. Knitted fabrics provide more elasticity than other kinds of fabrics because of their specific structures. And the way the yarns are looped together in knitted fabric means that less yarns are used, thus they are much lighter than woven fabrics.

Braid fabric. Braid fabric has a rope like structure. There are one set of yarns in the common braid style, in which the yarns are inter-weaved together by a diagonally overlapping pattern. The excellent elongation characteristic as well as flexibility is the most important advantages of braid fabrics.

Interlock fabric. To manufacture a stable textile reinforcement with high thickness, interlock fabric (3D fabric) is proposed (FIG. 1.3d). It is first developed nearly 30 years ago in an attempt to replace expensive high temperature metal alloys in aircraft brakes [MOU 99]. 3D fabric is preferred because of its ability to produce complex near-net-shape. Moreover, 3D woven composites have high ballistic impact damage resistance and low-velocity impact damage tolerance [LUN 95].

1.1.3 Types of matrix

The matrix in composite is basically continuous and homogeneous. Besides holding the reinforcement into a solid, it also protects the surface of the composite from damage and transfer the stress to the fibers in the structure. There are three kinds of common matrix material. They are organic (the most famous organic matrix is polymer, including thermoset organic, thermoplastic organic, rubber), metal and ceramic. The matrix of organics are light and have resistance to atmospheric and other forms of corrosion, and are non-electrical conductive. The metallic matrix is composed of light metals such as aluminum or titanium that is resistant to fire or other high-temperature environment, as well as radiation damage. Ceramic matrix receives attention in recent years, its advantages over traditional matrix mainly lie in its extreme thermal shock resistance, chemical inertness and super hardness.

Among all the matrix materials mentioned above, the polymer is the dominant one in most composites products. It can be thermosetting or thermoplastic. The thermosetting polymer is called thermoset, and it is soft or viscous and could change irreversibly into insoluble polymer network by curing. The advantage of thermoset is that it is better suited to high-temperature applications up to the decomposition temperature, and is generally stronger than thermoplastic polymer, yet it is more brittle. Thermoplastic polymer is also called engineering plastic. Its advantage is that the processing of thermoplastic is reversible : the resin becomes flowable above a specific temperature and it solidifies at lower temperature. So the resin can be formed into other shapes at the processing temperature.

1.2 Preforming technology for textile composite

Many automated processing methods have been developed to manufacture the composite components and products, such as Automated Tape Laying (ATL) and Automated Fiber Placement (AFP). Both of them rely on costly pre-impregnated materials. Autoclave is used to provide appropriate temperature and pressure for the preforming of composites, but this equipment is expansive and most importantly, it limits the size of the composite products. What's more, autoclave is energy consuming since the whole inner space of the autoclave should be heated to conduct the heat to the composite product. Considering all these, some new technologies such as Liquid Composite Molding has attracted the attention of researchers in recent years [MAC 56, ROB 81, ROB 84, Van 91, EBE 97, POT 01, IVA 01, IVA 02, TAB 03, BAH 04, DUR 05, YAN 14]. The Resin transfer molding (RTM) and Vacuum Assisted Resin Transfer Molding (VARTM) as well the Thermoforming process for thermoplastic prepregs will be introduced here.

1.2.1 Liquid Composite Molding (LCM)

Among the technologies to produce the composite components and parts, Resin Transfer Molding (RTM) is most commonly used to fabricate the composite components and parts. During this process, the dry fabric is stamped into an enclosed metal mould to get the preform with specific shape, followed by the injection of thermosetting resin. A schematic diagram of RTM is shown in FIG. 1.4. Comparing to those more traditional fabrication technology such as Compacting Prepreg or Autoclave, RTM is preferable for some reasons [SON 03]. First of all, the reinforcement with high air void contents can be compressed and fabricated with high volume fraction (vf) ; secondly, it is capable of fabricate parts with high complex shapes ; last but not least, RTM avoids hand lay-up thus is more efficient, and at the same time, the exposure of operators to harmful volatile is

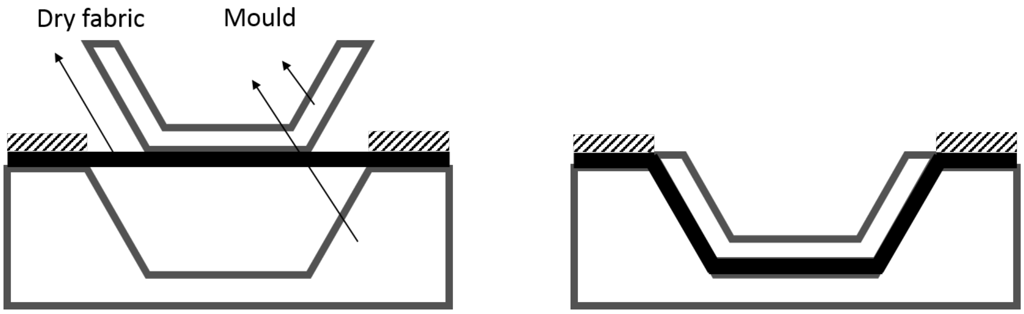

(a) RTM : initial state **(b)** RTM : preforming

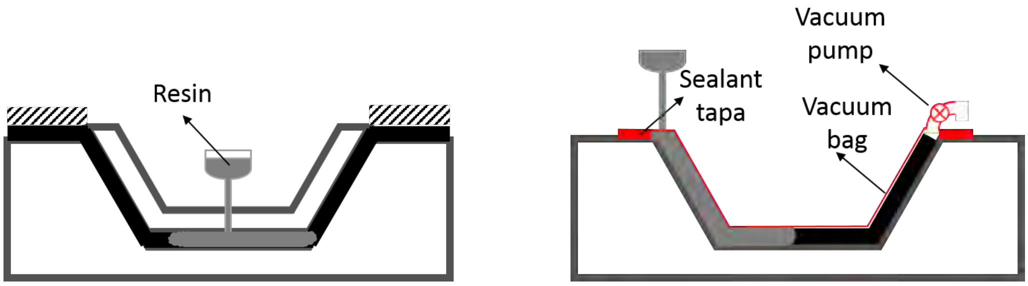

(c) RTM : injecting resin **(d)** VARTM

FIGURE 1.4 – RTM and VARTM

also reduced.

It seems that the most obvious shortcoming of RTM comes from the high cost of metal molds, which stimulates the development of Vacuum Assisted Resin Transfer Molding (VARTM) in recent years. As is shown in FIG. 1.4d, the upper mold in RTM is replaced by a vacuum bag. The air is firstly pumped out to provide a pressure environment until the dry fabric is compressed to the desired volume fraction ; due to the negative pressure state in the bag, resin can be injected into the bag with relative high speed (thus VARTM is also more time efficient than RTM). Both RTM and VARTM are composed of two stages : the preforming and the injection of liquid resin (so they are called Liquid Composite Molding, or LCM).

1.2.2 Thermo-forming process

The thermo-forming technology is applied on the forming process of prepregs. As is shown in FIG. 1.5, it contains four parts : first of all, the thermoplastic prepreg is heated to the melting temperature and becomes soft ; then it is stamped into the mold. There are usually three kinds of technologies to force the prepreg into the mold : the thermo-vacuum forming, the thermo-compression forming and the thermo-stamping ; in the third step, the deformed prepreg is consolidated ; at last, the product cools down and solidifies.

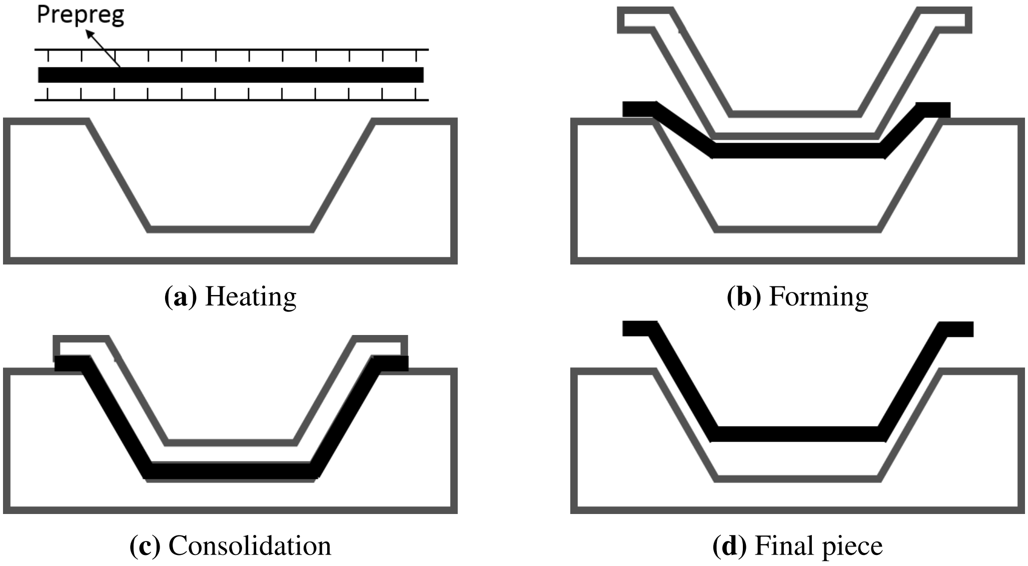

(a) Heating **(b)** Forming

(c) Consolidation **(d)** Final piece

FIGURE 1.5 – Thermo-forming process for prepregs [BOI 04]

1.3 Deformation mechanisms of textile composite

The important reasons for that textile composites are favored in automobile and aircraft industries are the fibrous features of the textile reinforcement. The tension performance will be firstly introduced since it provides the main resistance for the whole structure ; followed by the in-plane shear that contributes to the flexibility of fabric layer ; the bending stiffness of fabric is small but important for the generation and development of surface wrinkles ; the biaxial performance is also highlighted here because it reflects the weaving feature of woven fabric ; last but not the least, the transverse compaction performance of fabric layers is described.

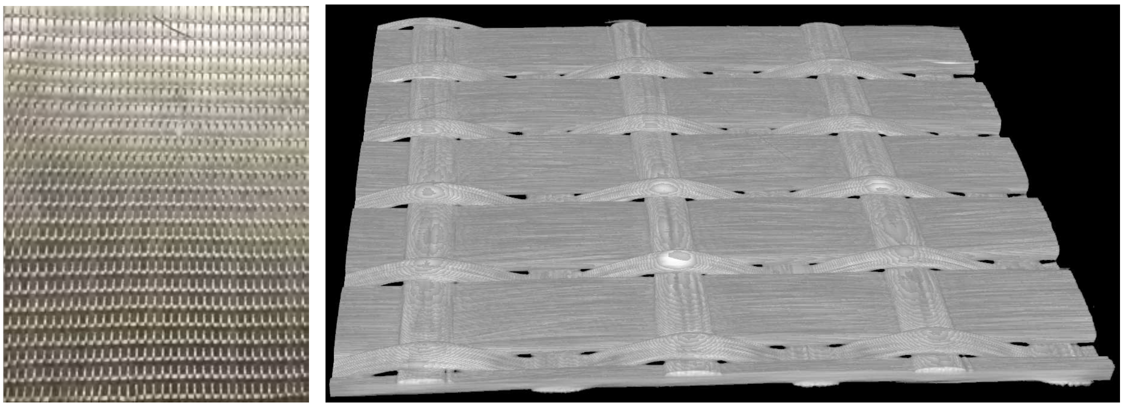

(a) Image of tapas fabric **(b)** Tapas fabric observed in tomography experiment

FIGURE 1.6 – Tapas fabric in this study

All the introductions will be based on a fabric named *tapas fabric* (FIG. 1.6). This fabric has small density value (its area density is 0.522 kg/m^2, and the density of the glass fiber is 2204 kg/m^3), thus is quite light. As will be shown, it has large tension strength, small in-plane shear stiffness as well as other outstanding mechanical properties. There are three kinds of yarns in this fabric : the largest one is called warp yarn and is much larger than the others and occupies most of the surface area of tapas fabric ; the yarn parallel to warp yarn is called binder ; the weft yarn is orthogonal to them. The thickness of tapas fabric is around 0.72 mm.

1.3.1 Tension

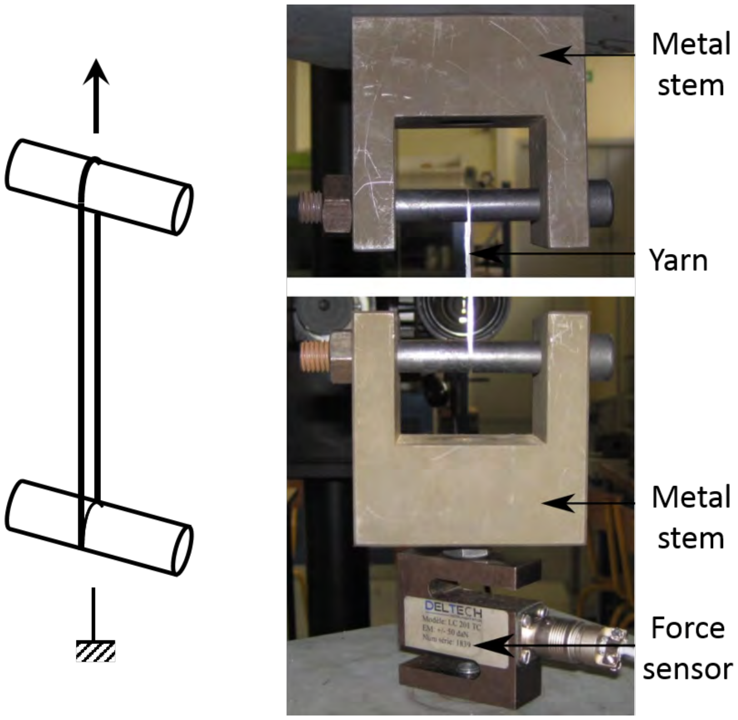

FIGURE 1.7 – An experiment setup for the tension test on yarn [FLO 13]

Uni axial tension is one of the most important deformations for textile fabric, because the tension stiffness provides the main resistance of composites. Manufacture process and simulation studies require a precise tension stiffness of the yarns and fabric layer. In the tension experiment on yarns, it should be ensured that the samples are fixed firmly (the yarns are normally slender and slippery). Charlotte FLORIMOND [FLO 13] used the experimental setup in FIG.1.7 to solve this problem. Besides the tension phenomenon of single yarns, the measurement of the tension stiffness for fabric is also measurement. This is because the stretch of fabric is a very normal phenomenon in the forming process of composite material, and the tension stiffness value of fabric is a important parameter for the macroscopic simulation of composite material.

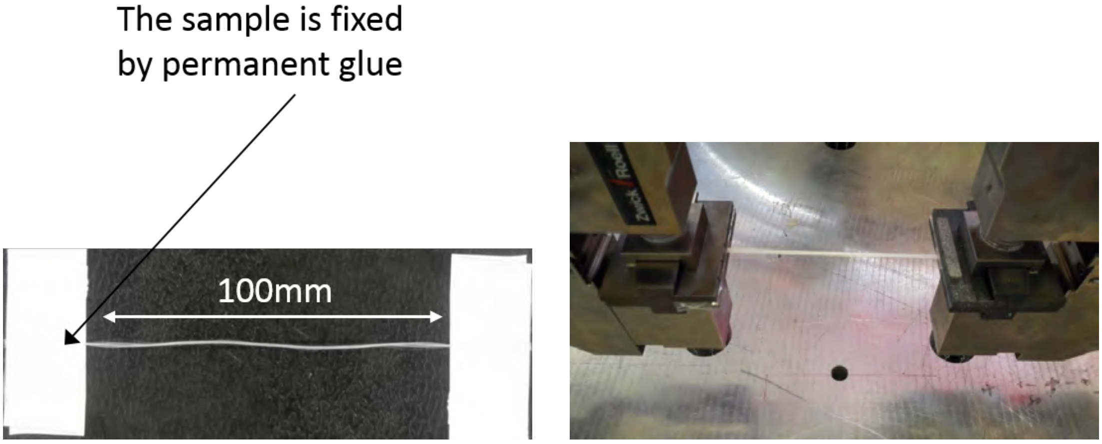

(a) The yarn is fixed by permanent glue to avoid the slide **(b)** Setup of tension test on the yarn of tapas fabric

FIGURE 1.8 – Tension test on the yarn of tapas fabric

For tapas fabric in this study, all the tension experiments are carried out on the Zwick Meca Bi-axes of LaMCoS, INSA de Lyon. To measure the tension stiffness of the yarns in tapas fabric, the three kinds of yarns are used as tension samples. To constrain the slide of the yarn, the ends of the yarn are fixed on plate by permanent glue to increase the friction when the sample is clamped by the clips (FIG.1.8a). To measure the tension stiffness of the fabric, fabric samples of 20 mm × 5 mm are used as tension samples. The stretching speed in the experiment is 2 mm/min, which is slow enough to avoid the dynamic interference. The strain can be calculated from the displacement d and the initial length L_0 :

$$\varepsilon_l = ln\frac{L_0 + d}{L_0} \tag{1.2}$$

so ε_l is the so called true strain along the yarn.

The tensile curves of the three yarns in tapas fabric are shown in FIG. 1.9a. All tensile curves begin with a nonlinear part, which can be explained by the rearrangement of the fibers. After the short nonlinear part, the tension performance of the yarn becomes linear. The tension stiffness of the yarn could be obtained by measuring the slope of the linear part : the tension stiffness values of the warp yarn, binder yarn and weft yarn in tapas fabric are around 19000 N, 2340 N, 2740 N separately. So warp yarn has a much large stiffness than the weft yarn, and tapas fabric is a high-unbalanced fabric. This feature of unbalance brings tapas fabric some specific deformation performances, *e.g.*, the asymmetric s-shape deformation [BAR 16] or out-of-plane deformation of the specimen in a bias extension experiment, which will be discussed in the next part.

The tension stiffness curves of the tapas fabric in warp and weft directions are shown in FIG. 1.9b. It is noted that the unit is $N/yarn$, which means the stiffness of the fabric is divided by the number of yarns in the concerning directions. Two conclusions can be

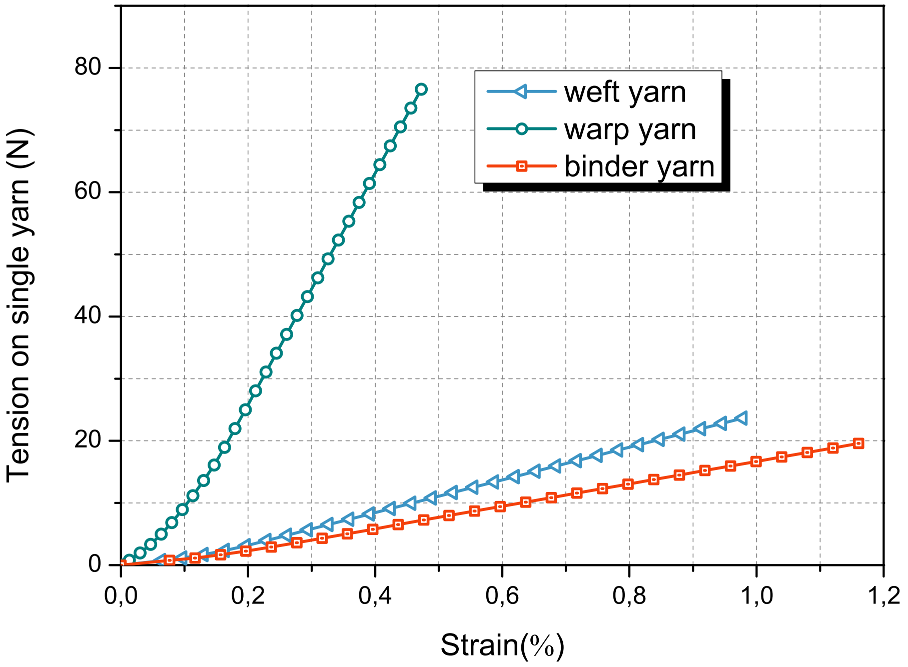

(a) Tentile stiffnesses of the yarns in tapas fabric

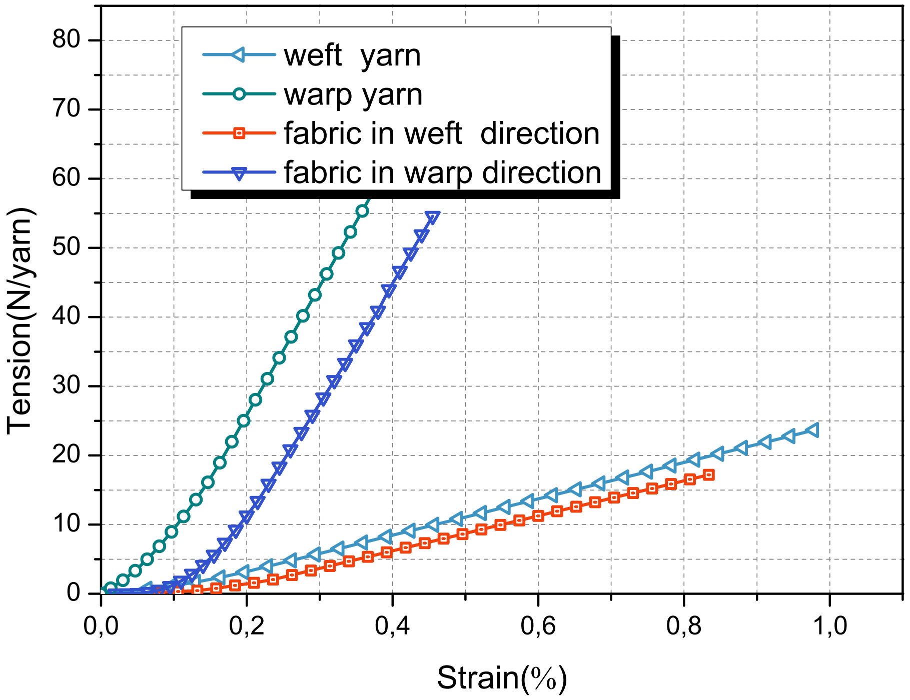

(b) The tensile stiffness of the tapas fabric

FIGURE 1.9 – The tensile stiffness of tapas yarns and fabric

drawn : the nonlinear part of fabric in warp direction is larger that of warp yarn, similarly, the nonlinear part of fabric in weft direction is larger that of weft yarn, which can be explained by the weaving nature of the woven structure ; as to the magnitude of tension stiffness, the fabric and the yarn have close stiffness values.

1.3.2 In-plane shear

In spite of the fact that the in-plane shear stiffness is tiny comparing to the tensile stiffness, the importance of the in-plane shear for the drapability cannot be overstated. *E.g.*, the locking angle has been proved an important concept that influces the generation and development of surface wrinkles (FIG. 1.10). The experimental identification of in-plane shear resistance, according to the benchmark reached since the year of 2003 [CAO 08], is realized through two kind of pure shear experiments : Picture Frame Test and Bias Extension Test.

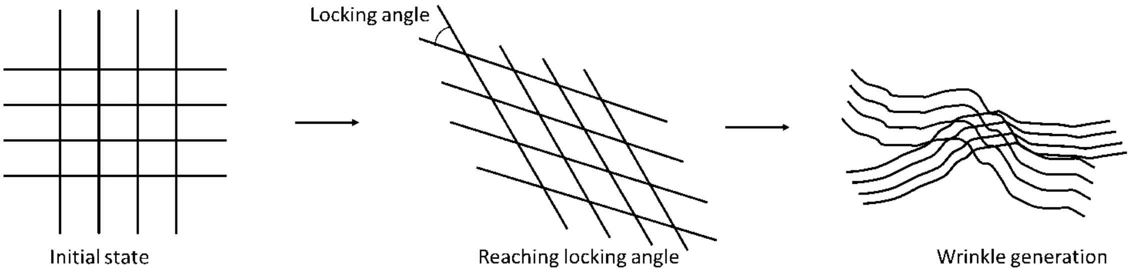

FIGURE 1.10 – The locking angle and the generation of wrinkle [PRO 97]

Picture frame test

The diagram of the picture frame test is shown in FIG. 1.11. The sample is cut into square and fixed in a pin joint frame which is stretched diagonally to realize a pure shear deformation. An ideal picture frame test fulfills the following assumptions : the shear strain distributes homogeneously on the fabric ; the shear of the fabric is the same with the frame, which is expressed as the function of displacement d :

$$\gamma = \frac{\pi}{2} - 2cos^{-1}\left(\frac{\sqrt{2}L_{frame}+d}{2L_{frame}}\right) \tag{1.3}$$

In an ideal test, the external power provided by the machine is assumed to be equal with the power absorbed by the sheared fabric :

$$F \cdot \dot{d} = L_{frame}^2 \cdot C_s \cdot \dot{\gamma} \tag{1.4}$$

where C_s is the normalized torque. Taking the geometry of the frame into account :

$$C_s = F \cdot \frac{L_{frame}}{L_{frame}^2} \cdot sin\left(\frac{\alpha}{2}\right) \tag{1.5}$$

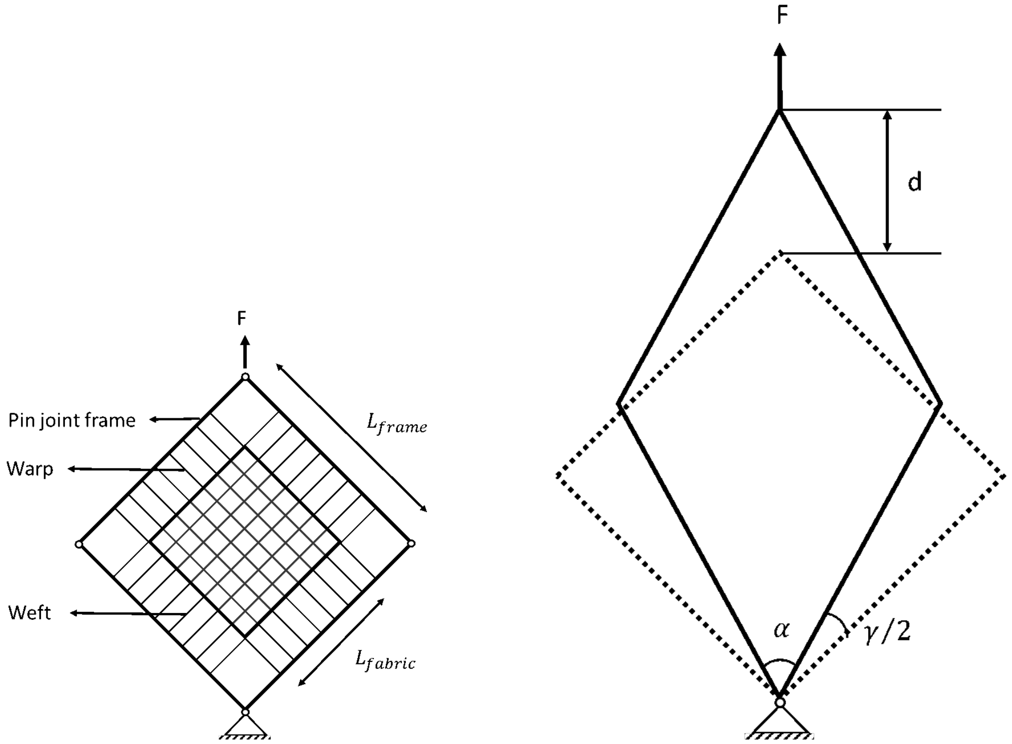

(a) Setup of shear sample **(b)** Deformed sample

FIGURE 1.11 – Diagram for the picture frame test

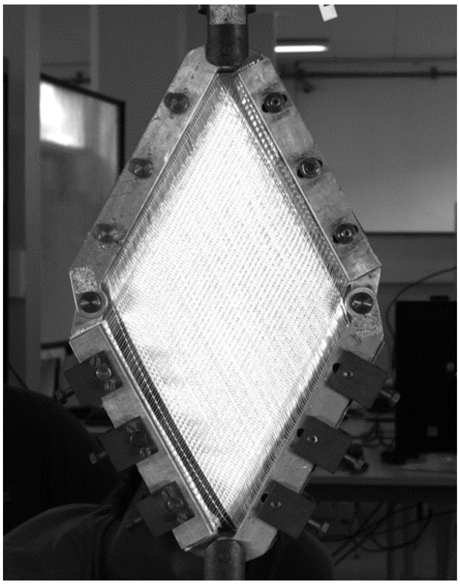

FIGURE 1.12 – The setup of picture frame experiment on Zwick Meca 10kN

For tapas fabric in this study, the sample of tapas fabric fixed by the metal frame in

FIG. 1.12. The borders of the sample are sticked with sheetmetals by permanent glue. The metal frame is fixed diagonally to make sure there is no shear deformation when the sample is fixed on the frame. It is noted that when the sample is fixed in a tight state, tension will be serious during the picture frame test. On the other hand the shear of the sample will be smaller than the frame if the fabric is fixed too loose. The experiment is carried out on a traction-compression equipment (Zwick Meca 10kN, LaMCoS, INSA de Lyon). Considering that the shear stiffness of the composite fabrics are normally small, the force sensor in the experiment should have a high sensitivity, so an extra force sensor (up to 500 N) is used.

The yarns in the fabric does not distribute homogeneously in the sample at the beginning of the experiment, so in some areas, the weaving is loose while in other areas it is too tight which introduces tension of the yarn during experiment. To homogenize the distribution of yarns, a cyclic loading is quite necessary. FIG. 1.13 shows an example of the cyclic loading for the picture frame experiments of tapas fabric, as can be seen, the loading force becomes smaller after several loading cycles.

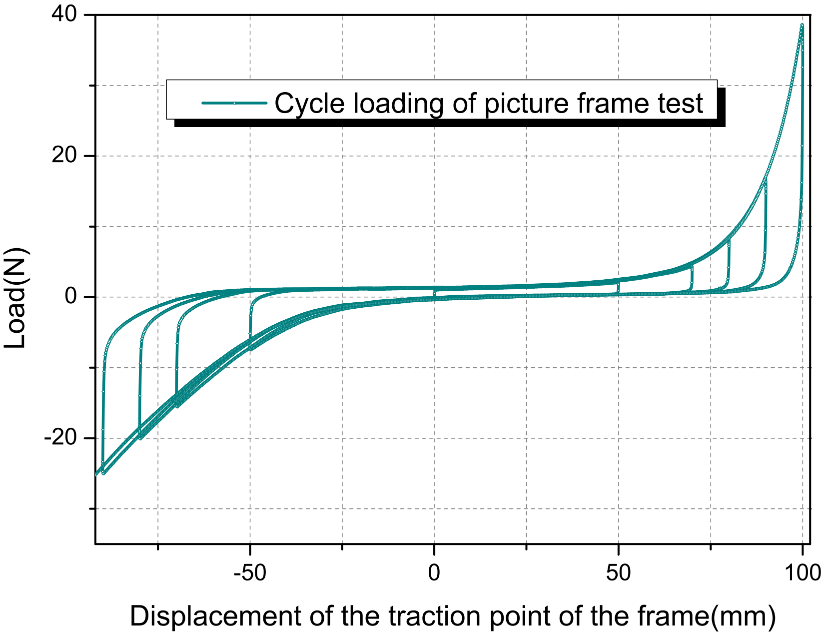

FIGURE 1.13 – The cyclic loading results of the picture frame experiments

One of the trickiest parts of picture frame experiment is the large tension appearing during the shear. On one hand, the tension of yarn is inevitable since it transforms the loading force from the metal frame to the fabric. On the other hand, the tension stiffness of the fabric is thousand times larger than its shear stiffness, so the tension of fabric or yarn could perturbed the measurement of shear stiffness. The perturbation can be serious, and this shortcoming is one important reason that the bias extension experiment is preferred by some researchers. The shear stiffness of tapas fabric measured by the picture frame experiment is shown in FIG. 1.17. This result is compared with the stiffness curve measured by another test that is called bias extension experiment, and it seems that the tension of the yarns in the picture frame experiments makes the result larger.

Bias extension test

Bias extension experiment is an alternative for picture frame test. As is seen in FIG. 1.14a, a rectangular sample is fixed by two grippers. Yarns are oriented $\pm 45^o$ to the loading direction. Displacements are applied on the grippers to stretch the sample, and the tensile force are measured by the sensors on the grippers. Bias extension is favored by many researchers for its simplicity comparing with picture frame test, especially in the aspect of experimental set-up.As is revealed in the experiments, the deformed fabric has three kinds of distinct zones : the zones A are the triangles next to the grippers, and they retain their shape all along ; zone B is located at the center of the sample, and it undergoes a pure shear deformation ; the transition regions between A and B also experience pure shear, and they are marked as C. The shear strain of C is half of the one of B. In an ideal bias extension test, the in-plane shear (B and C) and bending deformation (on common borders of A and C, B and C) dominate the deformation of the fabric.

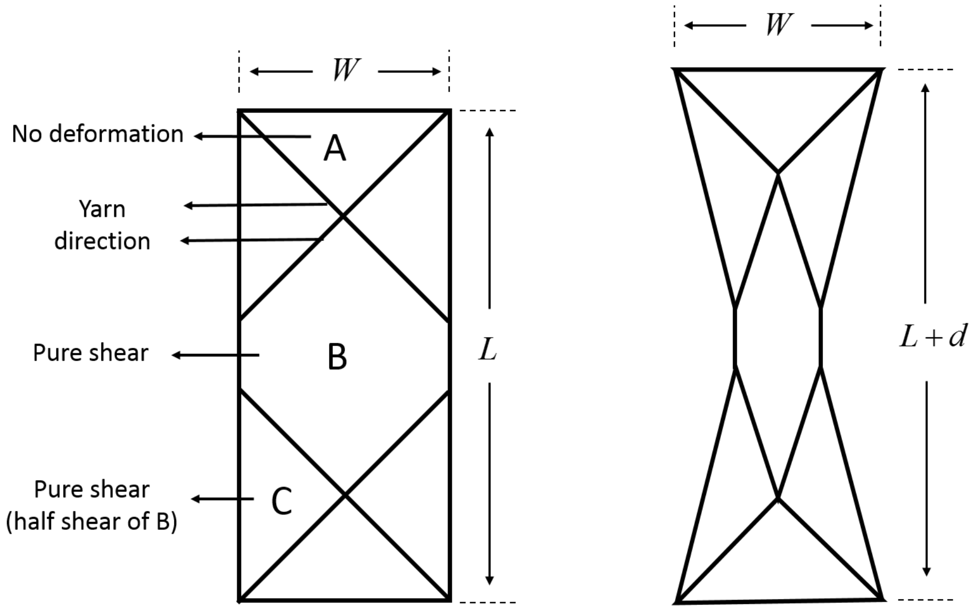

(a) The sample before extension **(b)** The sample after extension

FIGURE 1.14 – Diagram of bias extension experiment for fabric

The shear angle (FIG. 1.14a) of zone B, with respect to stretching displacement d, can be expressed as :

$$\gamma(d) = \frac{\pi}{2} - 2cos^{-1}\left(\frac{L+d}{\sqrt{2}L}\right) \tag{1.6}$$

The power from the tensile force F is assumed to be dissipated completely into the

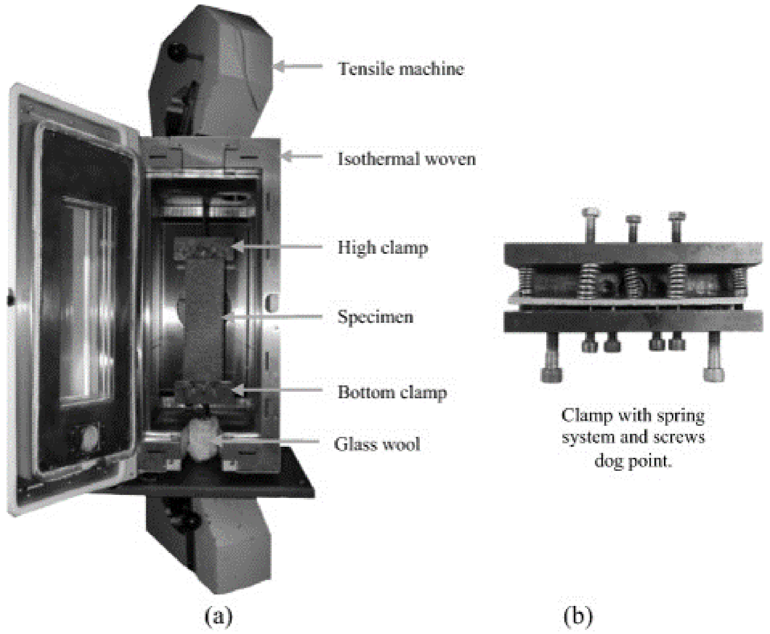

FIGURE 1.15 – Bias extension test set-up for different temperature [GUZ 15]

pure shear energy in zones B and C :

$$F\cdot\dot{d} = C_s^{\gamma}\cdot S^{\gamma}\cdot\dot{\gamma} + C_s^{\frac{\gamma}{2}}\cdot S^{\frac{\gamma}{2}}\cdot\frac{\dot{\gamma}}{2} \tag{1.7}$$

where S^{γ} and $S^{\frac{\gamma}{2}}$, C_s^{γ} and $C_s^{\frac{\gamma}{2}}$ are the areas and normalized torques of zone B and zones C, respectively. Substitute EQ. (1.6) into EQ. (1.7), we obtain :

$$C_s^{\gamma} = \frac{1}{2L-3W}\left(\left(\frac{L}{W}-1\right)\cdot F\cdot\left(cos\frac{\gamma}{2}-sin\frac{\gamma}{2}\right)-W\cdot C_s^{\frac{\gamma}{2}}\right) \tag{1.8}$$

Some more complex setups are developed based on FIG. 1.14. For example, FIG. 1.15 shows a setup by Wang [WAN 12] and Guzman [GUZ 15]. The bias extension can be done in different temperatures, which is interesting when the specimen is thermoplastics.

For the tapas fabric in this study, the bias extension experiment is carried out at room temperature, on Zwick Meca 10kN, LaMCoS, INSA de Lyon. FIG. 1.15 provides the setup for the experiment. Loading velocity of the experiment is as slow as 2 mm/min to avoid the dynamic influence. It is noted that the tapas fabric is not a balanced fabric and the mechanical properties are different in the two orthogonal directions. As a result the out of plan distortion develops during the test and the out-of-plane phenomenon of the fabric and the sliding of the yarn are obviously observed at the final stage of the experiment (FIG. 1.16). This phenomenon concerning the deformation of unbalanced fabric has been studied by Barbagallo [BAR 16] *et al.*, in which the influence of the strong unbalance in the bending stiffness is specially highlighted. They use a second-gradient term to consider the differential bending rigidity values of the two families of yarns.

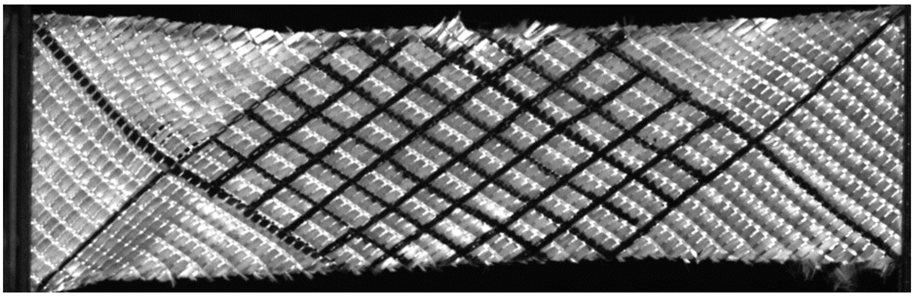

(a) The tapas sample in the beginning stage of bias extension experiment : all in a 2D plane

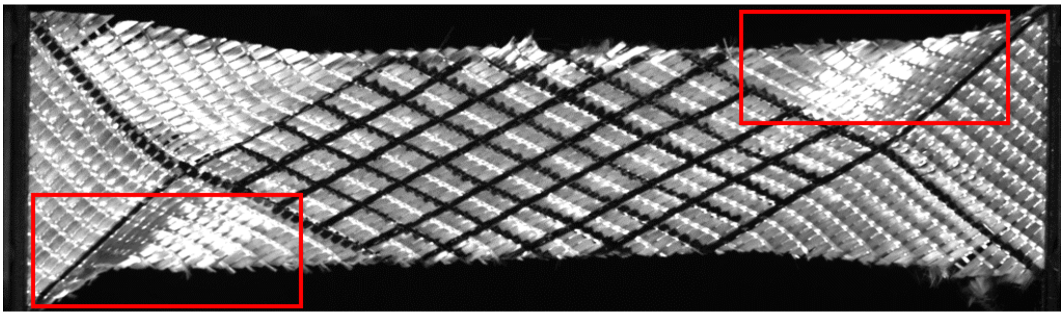

(b) The tapas sample in the final stage of bias extension experiment : out-of-plane deformations arise

FIGURE 1.16 – The tapas fabric during the bias extension experiment

1.3.2.1 Conclusion of in-plane shear

So in conclusion, when the in-plane shear test is required for the unbalanced composite such as tapas fabric, the two kinds of tests have their own merits and demerits respectively. For the picture frame experiment, the out-of-plane phenomenon is constrained, but the tension of the yarn and fabric would lead to a too large measurement. And for the bias extension test, the range of measurement is limited since distortion and sliding appear when the shear angle is large. The results of these two tests on tapas fabric are shown in FIG. 1.17. The latter one gives smaller stiffness since it avoids tension of yarn/fabric. As can be seen, the shear curve of woven composite includes three shear phases : at the very beginning of the in-plane shear deformation, the resistance comes from the contact friction thus is quite small. The yarns only have rotation deformation and the space between them tend to be closed. Then the second phase starts when the side contacts of yarns become obvious and the shear stiffness increases. When the space between yarns almost disappears and the shear locking arises, the lateral compaction becomes the main source of shear stiffness.

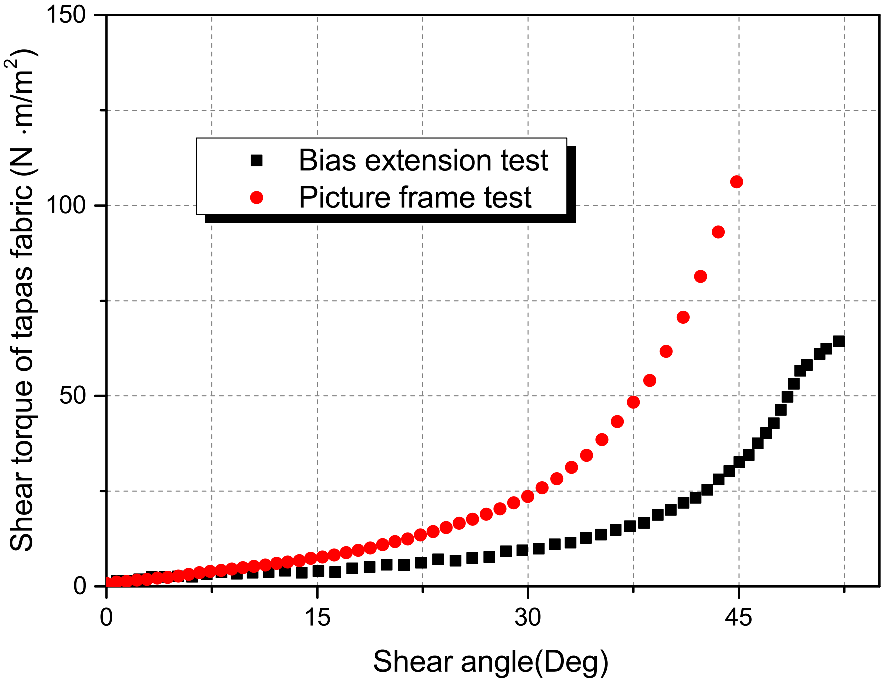

FIGURE 1.17 – Shear stiffness measurements of the tapas fabric, from bias extension test and picture frame test

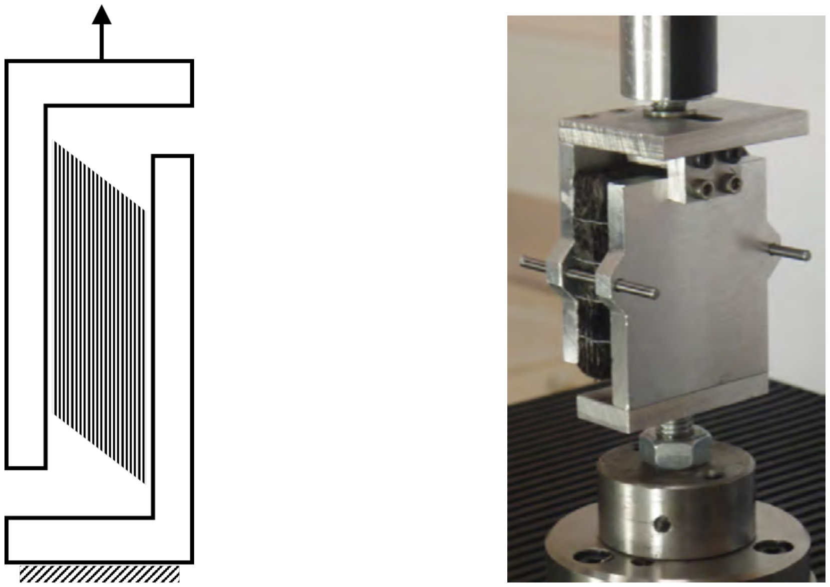

FIGURE 1.18 – Experiment setup for the transverse shear experiment [CHA 12]

1.3.3 Transverse shear

Transverse shear stiffness is important for the macroscopic simulation of the composite fabric. Different with the in-plane shear, transverse shear reflects the shear in the transverse section of the fabric. It has been studied by many researchers [CHA 12, HAA 14]. FIG. 1.18 is a kind of experiment setup used in the work of A. Charmetant to measure the transverse shear stiffness [CHA 12]. The transverse shear stiffness of the fabric in warp and weft directions are measured. As can be seen, the sample of the fabric stack is fixed on the parallel planes, and pure transverse strains are imposed to the specimen. He found that the transverse behavior of the fabric stack can be split into two phases : a first one during which the stiffness initially strong decreases significantly and a second one during which the stiffness is quite constant [CHA 12].

1.3.4 Bending

(a) Simulation without bending stiffness **(b)** Bending stiffness is considered in the simulation

FIGURE 1.19 – The influence of bending stiffness on draping simulation [LIA 16]

The bending stiffness of the fabric or the yarn is small but complex. When a yarn is bent, there could be relative sliding between fibers, as a result, the bending stiffness value is not directly related to the in-plane mudulus as the classical continuum materials [LIA 16]. Bending stiffness of textile fabric has been proved non-ignorable by many researchers [LIA 14, BOI 11]. The importance of bending stiffness can be well explained by FIG. 1.19, which shows two simulations for the draping of a woven fabric on a cylinder. In the first figure only the tensile and in-plane shear rigidities are considered while in the second one the bending stiffness is also taken into account. Obvious differences can be found between them. It is obvious that bending stiffness has influence on the shape and number of wrinkles. Bending of reinforcement is an out of plane behavior and depends on the geometrical configuration of the yarns and their mechanical properties as well as the contact properties of adjacent yarns [BIL 09].

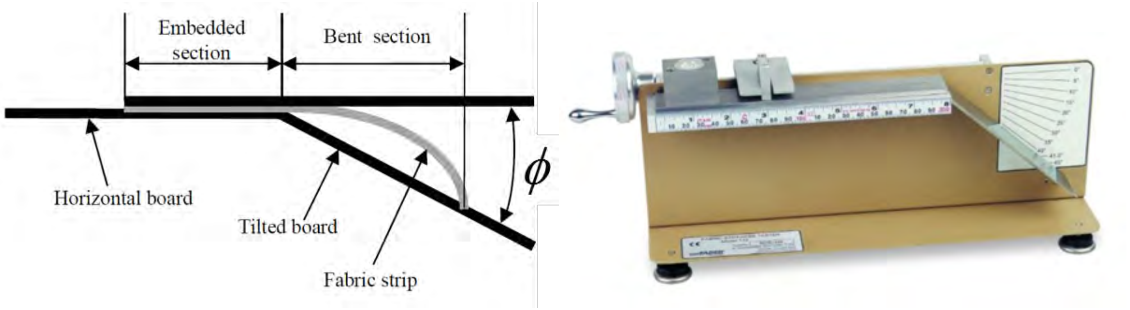

FIGURE 1.20 – The standard cantilever bending experiment [LIA 16]

The bending stiffness of a fabric is normally expressed by curvature-bending moment curve. There are different experiments for the bending performance of composite fabric. The first one is the standard cantilever test (FIG. 1.20). It has been found that the angle of the tilted board should be between $40^o \sim 50^o$ to make sure the measured bending stiffness is stable [ABB 51]. The strip of fabric is set on the horizontal board and moved slowly toward the tilted board, until the end of the fabric strip touches the titled board. The bending stiffness can be calculated according to the following equation :

$$B = \frac{l^3}{8} \frac{cos\,(\phi/2)}{tan\,(\phi)} \cdot w \tag{1.9}$$

where B is the bending stiffness of the fabric along the corresponding orientation ; w is the weight per unit area and l is the length of the bending part of the strip. So in this test only one parameter (the stiffness B) is to be decided, and the nonlinear information of the fabric bending is ignored.

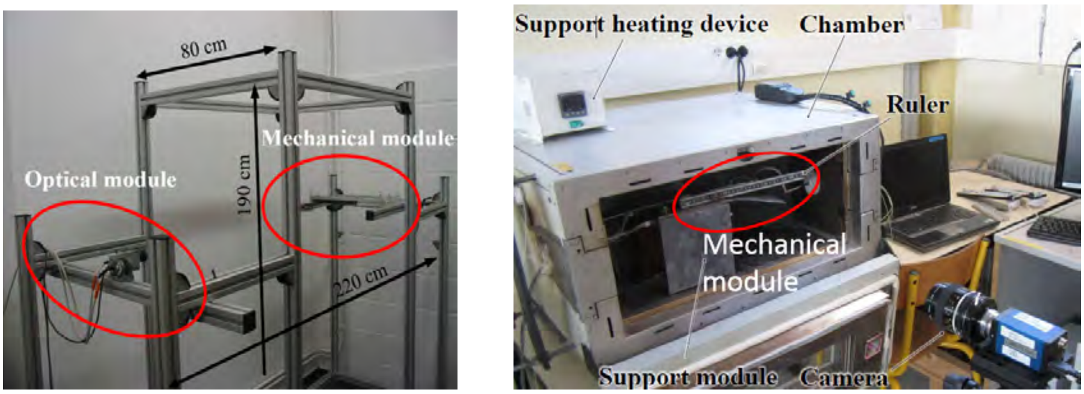

(a) Bending test device developed by Debilbo [BIL 09]

(b) Bending test device that could work at different tempratures [LIA 16]

FIGURE 1.21 – Two experimental setups for the bending test of fabric

DeBilbao [BIL 09] improved the cantilever experiment with an optical method (non-contact measurement). The experiment devices are shown in FIG. 1.21a : the mechanical part clamps the specimen of fabric and the optical module could take photos with high resolution. The specimen is cut from the fabric along the concerned direction (the warp or weft direction). One end is fixed horizontally while the rest of the part bends under gravity. Sometimes a lumped mass can be added at the free end to realize a larger bending. Since this device works at room temperature, Biao Liang [LIA 16] developed another setup (FIG. 1.21b) to enlarge its application to different temperatures. The information about the curvature and bending moment can be analyzed from the profile shape of the bending strip. This optical cantilever test works for a large range of fabric, despite of the thickness and number of layers of the fabric, and thus is recommended.

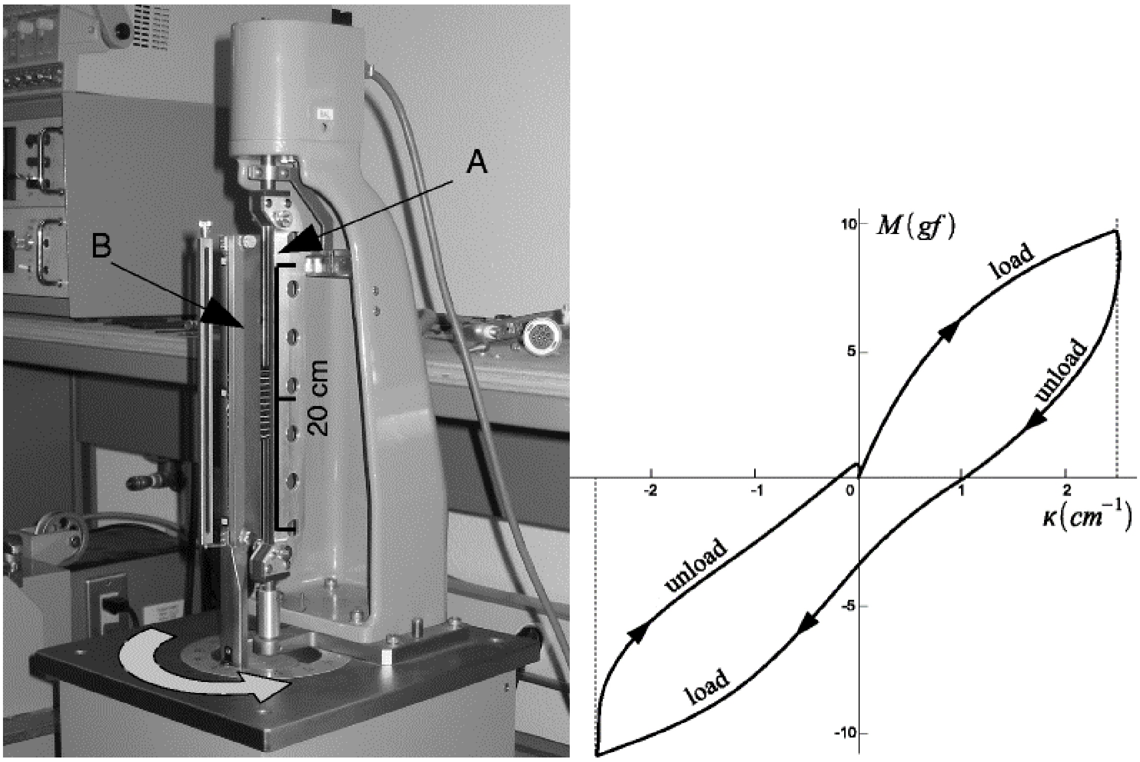

(a) The KES-FB2 bending equipment **(b)** An example of bending result on fabric

FIGURE 1.22 – The bending test designed by Kawabata [BIL 09]

The third experiment is designed by Kawabata [KAW 08] and is capable of record the moment versus the curvature during a bending cycle, this method works well on clothing textiles instead of thicker and stiffer composite reinforcement. The equipment is shown in FIG. 1.22. The fabric sample is fixed by two clamps, and one of them is movable. FIG. 1.22b is an example of the bending result from this method. As can be seen the nonlinear part of the bend phenomenon is taken into account, which is an advantage over the standard cantilever test.

For the tapas fabric in this study, the bending test has been carried out by STEER at

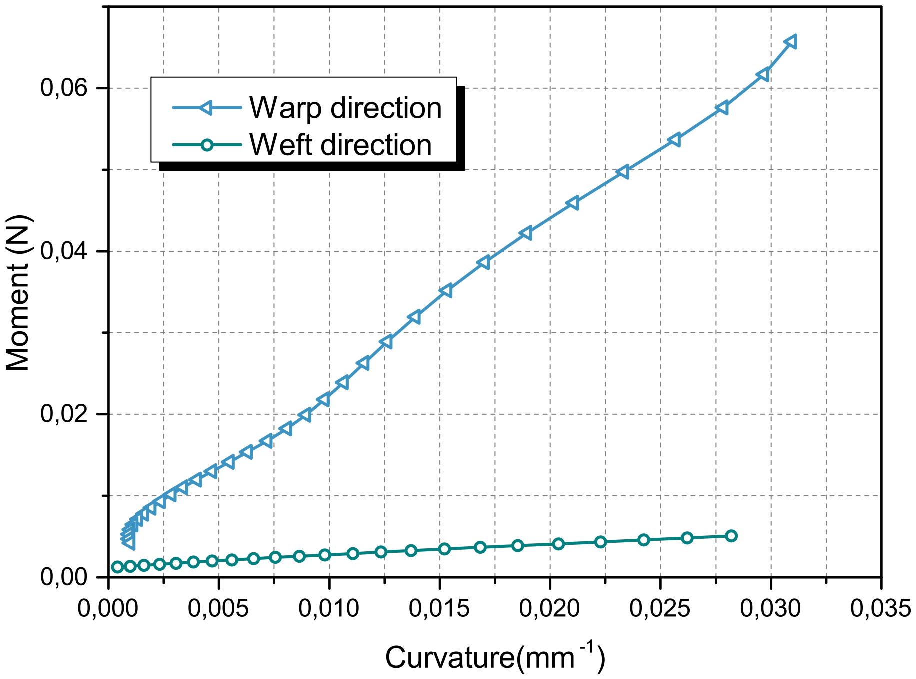

FIGURE 1.23 – The bending stiffness curves of tapas fabric in warp and weft directions

LaMCoS, INSA de Lyon, based on the cantilever bending experiment. The sample is the single layer tapas fabric, and the experiments are done in the room temperature. FIG. 1.23 shows the bending stiffness of the tapas fabric in its warp and weft directions. It is noted that the unit for y-axis is *N*, so the quantity expressed in y-axis is in fact the bending moment per unit width of the fabric strip. It can be found that the bending stiffness of the tapas fabric in the warp direction is much larger than that of weft direction, which implies that the tapas fabric is a high-unbalanced fabric. The largest bending moment is found at the fixed end of the fabric strip, while the smallest one is at the free end of the bending strip. Moreover, the fact that the curve is quite linear implies the assumption of a constant bending stiffness.

1.3.5 Biaxial extension

Biaxial behavior means the interaction of mechanical behavior along different yarn directions. For example, the biaxial tensile test on a fabric shows a progressive nonlinear hardening which arises from the undulated nature of the yarns in the fabric, and this nonlinearity performance changes with the tension states along another yarn direction [KAW 73, CHE 93, HIN 96, BUE 01, WIL 08]. This is definitely a kind of biaxial behavior. To better understand this fabric-specific behavior, an amount of researches have been undertaken. FIG. 1.24 shows two different biaxial loading on a plain woven fabric. It has been proved that the loading in y direction influences the undulation of not only the yarns in y direction, but also those in x direction.

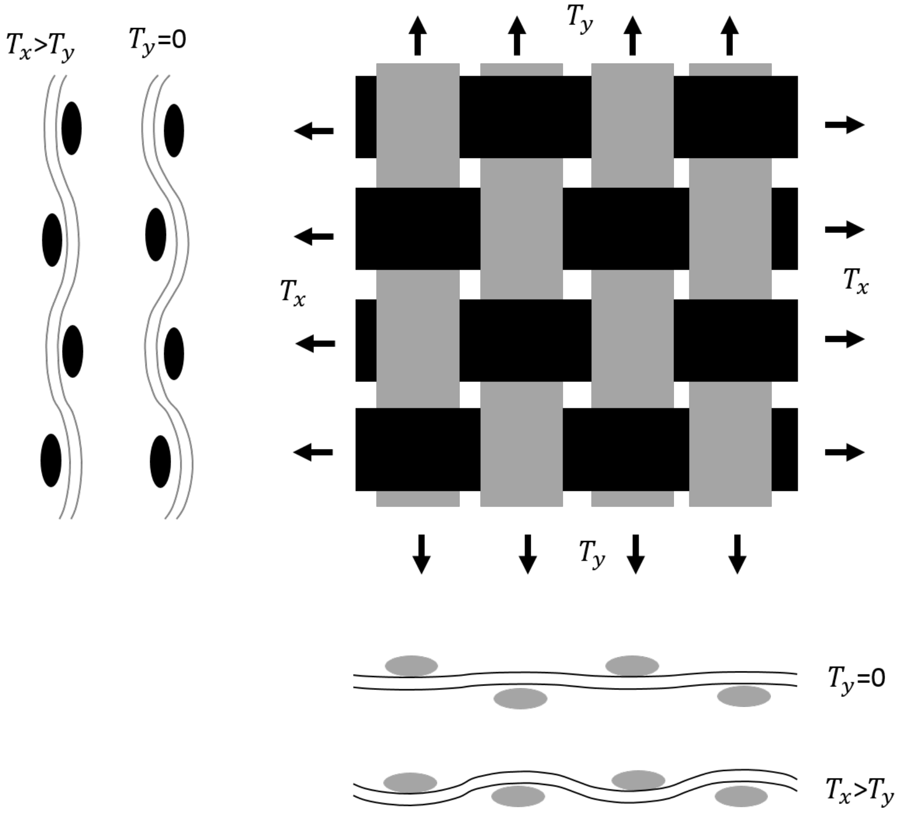

FIGURE 1.24 – The illustration for the test of biaxial tension

The biaxial tension test of tapas fabric is realized on Zwick Meca Bi-axes of LaMCoS, INSA de Lyon (FIG. 1.25a). This machine is designed for the biaxial tension test, and has four fixtures and force/displacement sensors distributed in two orthogonal directions. All of them can move independent of each other with different velocity. The fixture No.1 and No.3 are distributed in one line, and orthogonal to them are fixture No.2 and No.4. The velocity of the fixture should be slow enough to make sure the experiment is a quasi static one. The tapas fabric sample used in the experiment is shown in FIG. 1.25b.

The experiment results are shown in FIG. 1.26a (tensile stiffness of tapas fabric in the warp direction) and FIG. 1.26b (tensile stiffness of tapas fabric in the weft direction). The parameter k has the following expression :

$$k = \frac{\varepsilon_x}{\varepsilon_y} \tag{1.10}$$

where ε_x and ε_y are strains in orthogonal directions. It seems that a large k will significantly reduce the non-linearity of the tensile performance. The biaxial phenomenon, in

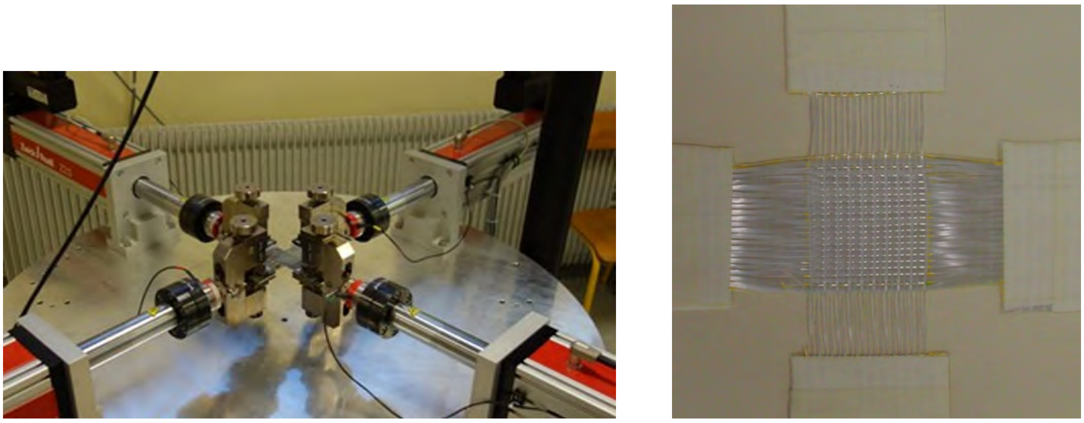

(a) Zwick Meca Bi-axes of LaMCoS,INSA de Lyon **(b)** The sample of tapas fabric for the biaxial tension test

FIGURE 1.25 – The biaxial tension test for tapas fabric

essence, reflects the coupling of the tensile deformation and transverse compaction deformation. Considering this point, this experiment will be used to measure the parameter in the F.E. model in section 3.2.

1.3.6 Transverse compaction

The study on the transverse compaction of composite reinforcements should be highlighted, because it is one of the most important deformations arising in textile reinforcements during composites manufacture. Especially for the LCM process, the transverse is the dominant deformation : it increases the volume fraction of the dry fabric to the required value, which has an important influence on the flow of resin, moreover, if one wants to know the requirements of the mould (the values of the forces required to close and maintain closure of the mould during the LMC), the knowledge of fabric transverse compression properties is necessary [BIC 03, KEL 11]. Transverse compaction is also important for the consolidation of prepregs : although the change of volume fraction of the prepreg during the compression is not as significant as in LCM, the transverse compaction helps to drive out voids [KEL 11]. So transverse compression response of composites should be well studied by experiment.

For the tapas fabric in this study, different kinds of compaction tests have been carried out and some interesting results are obtained. These experiments include the compaction on single layer fabric (with different shear angles), or multilayer fabric samples (with different layouts and shear angles). The machine used to compact the fabric samples is Zwick Meca 10kN at LaMCoS, INSA de Lyon. The compaction setup is shown in FIG. 1.27. The reinforcement is positioned on the bottom plate which is a 100-mm diameter steel plate, and the size of the sample is larger than the compaction plates. Since the thicknesses of the tapas samples can be as small as several millimeters (*e.g.*, the single layer of tapas fabric is around 0.72 mm), the bottom plate is versatile (FIG. 1.27b) to make sure the

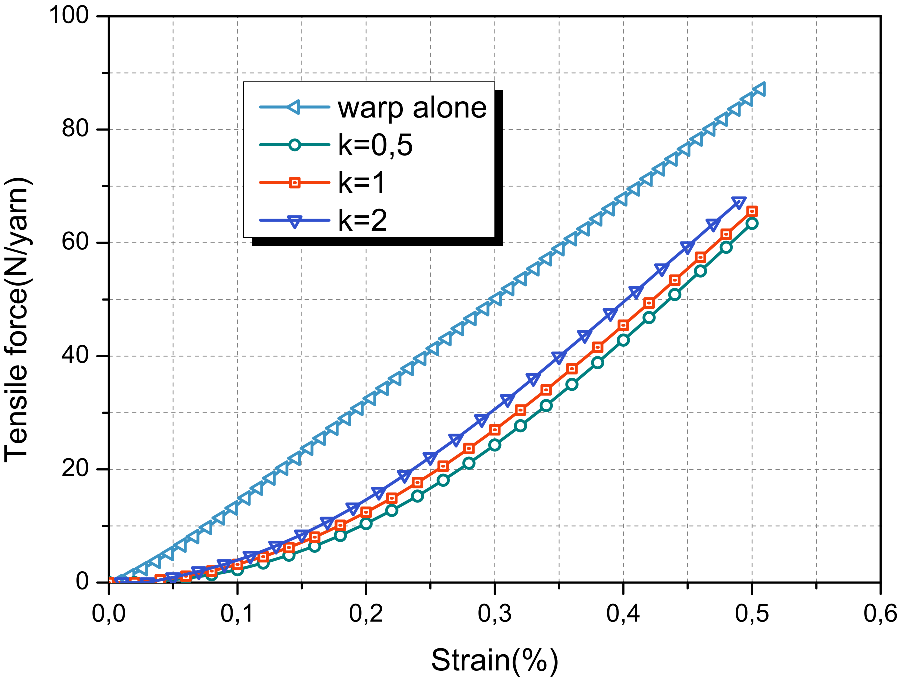

(a) Biaial tension tests on warp direction of tapas fabric

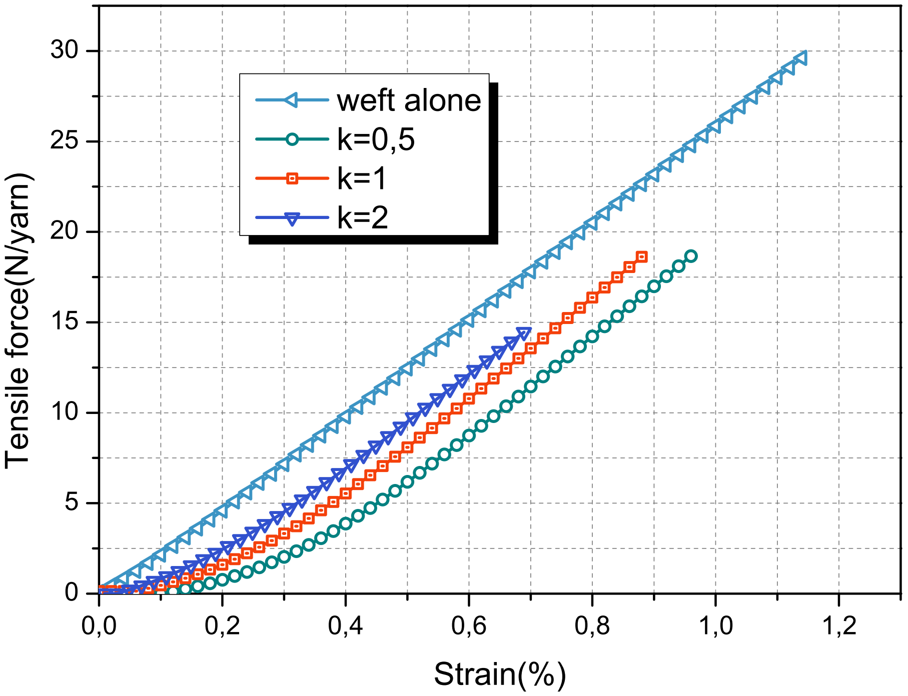

(b) Biaial tension tests on weft direction of tapas fabric

FIGURE 1.26 – Biaxial tension tests on tapas fabric

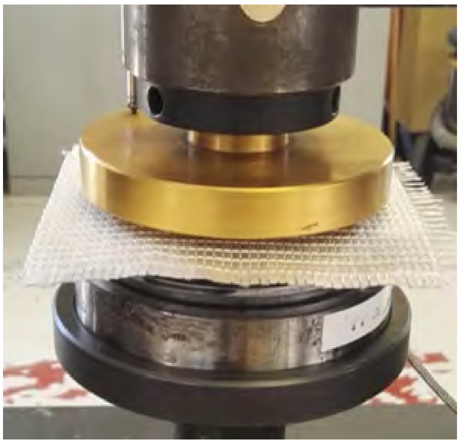

(a) Setup with versatile base

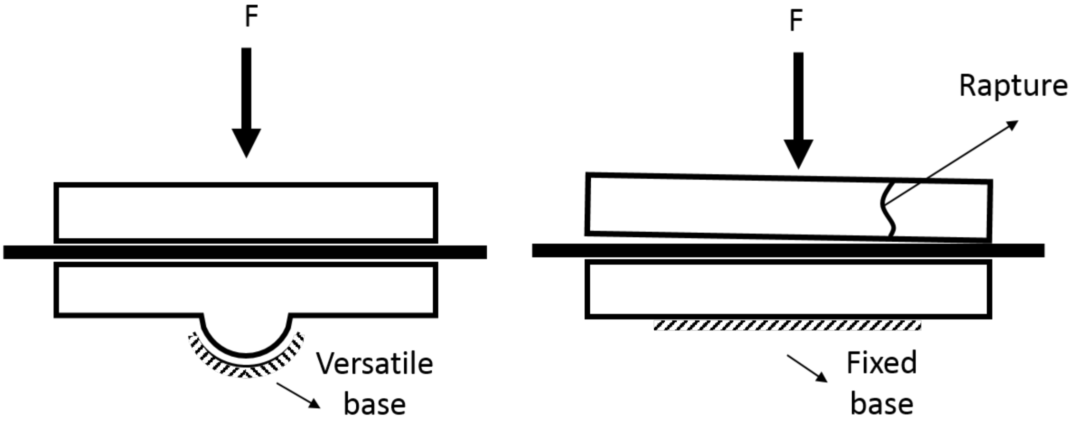

(b) Setup with versatile base **(c)** Fixed compaction base

FIGURE 1.27 – The setup of compaction test

compaction force is perpendicular to the fabric surface precisely. This is important for the sake of a uniform pressure distribution [WAL 12], as well as protecting the devices. A displacement sensor is used to measure the distance between the bottom and top plates. The compaction velocity is 2 mm/min to make sure the experiment is a quasi static one. The tests on different kinds of samples have been repeated several times.

Compaction on single layer fabric

FIG. 1.28 shows the stiffness curve of the single layer tapas fabric, in which vf is the volume fraction of the fabric :

$$vf = \frac{m_s \cdot n}{\rho \cdot \delta} \tag{1.11}$$

where m_s is the areal mass of a single fabric ; n is the number of fabric layers ; ρ is the material density (the density of the fiber) ; δ is the distance between compaction plates.

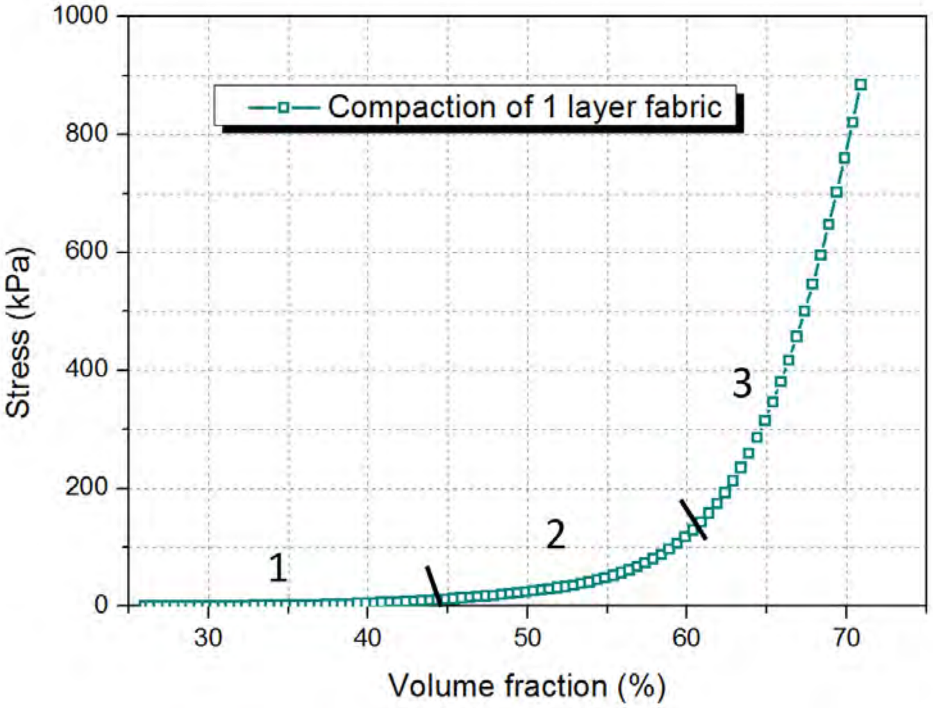

FIGURE 1.28 – The compaction stiffness of the single layer tapas fabric

The three parts of the compaction stiffness curve in FIG. 1.28 are explained as follows : at the beginning stage of the transverse compaction, the thickness of the sample is not uniform over the total area (this is caused by its woven nature), and the compaction exist locally at thick places. During the second stage, the fabric is compacted to a uniform thickness and the yarns/fibers in the fabric experience rearrangements to adapt to the reduction of space, and the stress rises up slowly. Finally, there is not enough space for the rearrangements and the stress increases sharply to reach a value as high as 1200 KPa.

Compaction on fabric stacks

In the industry field, the fabrics are often stacked up to manufacture products with a thickness larger than the ply. The compaction could change the internal structure of the fabric stacks, which will influence the phase of resin injection in LCM. So it is meaningful to study the compaction performance of fabric stacks.

When the compaction experiments are carried out on fabric stacks, the yarns in one fabric goes into the void of the adjacent fabrics. This is called nesting and it could reduce the compaction stiffness. The nesting phenomenon of composite fabric has been studied by many researchers [LUO 99, LOM 03, NGU 13]. *E.g.*, Nguyen [NGU 13] found that for twill 2×2 fabric, the compaction stiffness of the fabric stack is alway smaller than the single layer sample, and for the stacks, the largest stiffness could be found in the layout of $0^o/45^o/0^o$ since the nesting in this case is the smallest (FIG. 1.29a).

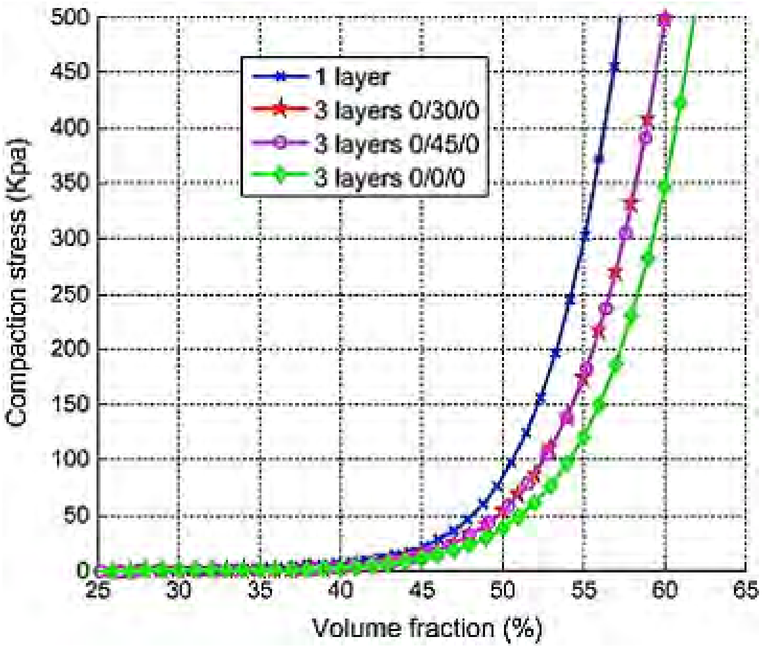

(a) Transverse compation experiments on a twill fabric 2/2 by Nguyen [NGU 13]

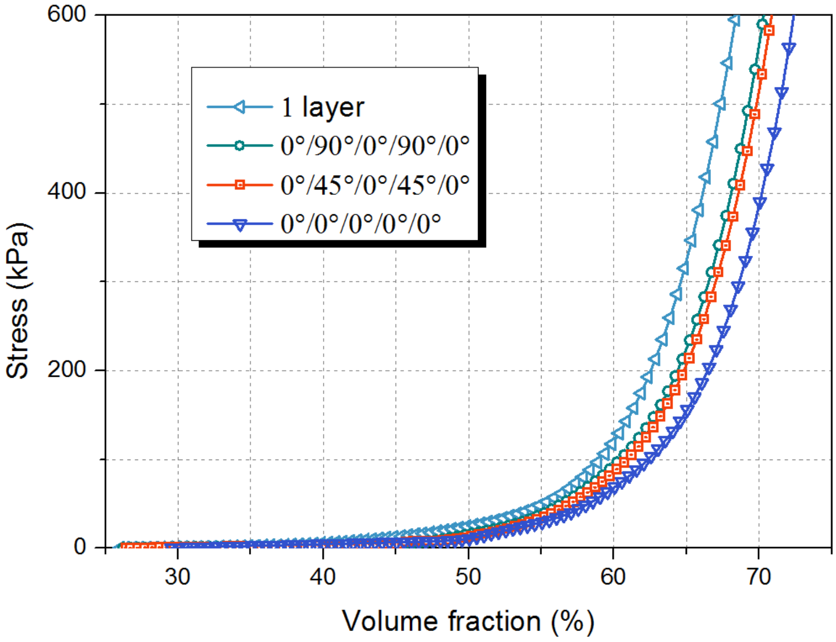

(b) Transverse compation experiments on the tapas fabric

FIGURE 1.29 – Compaction on fabric stacks

The similar conclusion could be found on tapas fabric. Since the warp yarn in the tapas fabric is much larger than the weft yarn or the binder yarn (FIG. 1.6), it takes up most of the surface area of the fabric. As a result, transverse compaction stiffness of tapas fabric is led by the warp yarn. Noting that the nesting phenomenon of the warp yarns would reach the minimum in the case of $0^o/90^o/0^o/90^o/0^o$, this kind of stack layout has the largest transverse compaction stiffness (FIG. 1.29b).

The effect of in-plane shear on its compaction

In-plane shear is an important deformation during the forming process of composite. Experiments on tapas fabric show that in-plane shear can modify the compaction stiffness [NGU 13]. This is mainly because when the shear happens, the void between yarns and the fibers become smaller and almost disappear when the locking angle is reached. So there will be less space for the yarn and fiber to rearrange themselves when the compaction happens.

For the tapas fabric, FIG. 1.30a exhibits three compaction curves corresponding to different in-plane shear states. As can be seen, when the tapas fabric has a shear deformation in its 2D plane, the compaction stiffness increases largely. Besides the single fabric layer, the influence of in-plane shear to the compaction stiffness of the fabric stacks is also studied. FIG. 1.29a provides the compaction results on tapas fabric stacks with different in-plane shear angles. It seems that the shear deformation has a large influence on the compaction stiffness of fabric stacks. There are three groups of stacks in this experiment : in-plane shear of 13^o, in-plane shear of 20^o, in-plane shear of 28^o. And each group has two kinds of layouts : $0^o/90^o$ and $/0^o/0^o/0^o$. So there are totally 6 stiffness curves in the comparison. It seems that the in-plane shear angle is the foremost factor that affects the compaction stiffness, and the secondary factor is the layout angles (with the same in-plane shear deformation, the stacks with a layout of $0^o/90^o$ performs stiffer than the one of $0^o/0^o$).

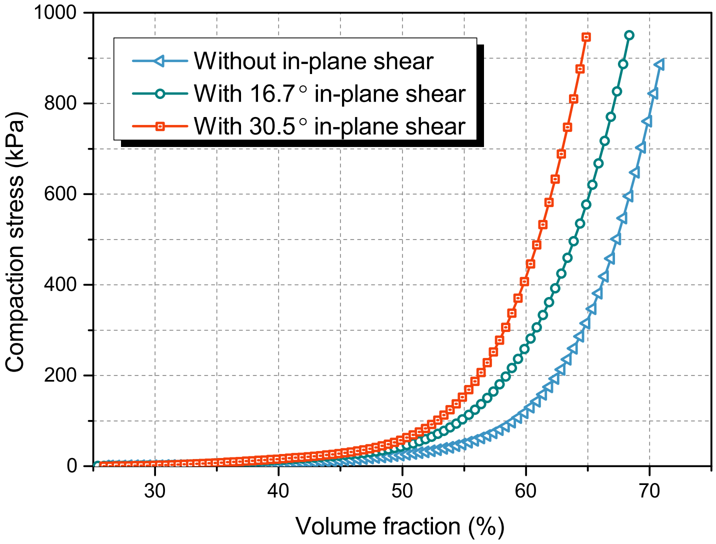

(a) The compaction stiffness of single layer tapas fabric with in-plane shear deformation

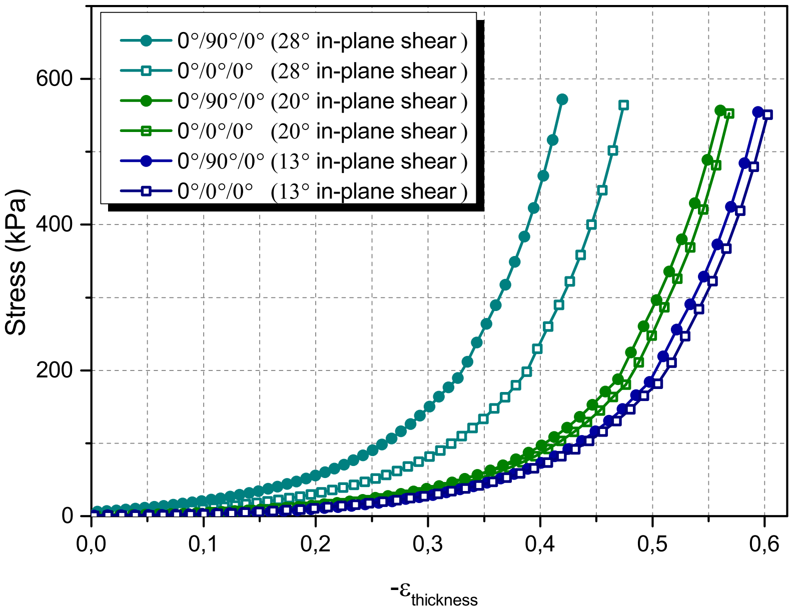

(a) The compaction stiffness of tapas fabric stacks with different in-plane shear angles and layer-outs

FIGURE 1.29 – The influence of in-plane shear to the compaction stiffness of fabric/fabric stack

1.4 Numerical approaches for analyses of reinforcement deformation

The optimal research of reinforcement preforming could be costly and sometimes time consuming, and the reasons stem from not only the material consumption, but also the experiment equipment. This motivate the academic work on some numerical studies. For composite material, the numerical methodologies are usually grouped into two categories : the kinematic methods that are also called fishnet algorithms are favored for their high efficiency, since they are capable of provide the draping appearance (this is sufficient in some industrial occasions) in a short computer time ; the second one is based on the development of finite element technology, which can take into account more details and get more precise results. Composite researches have benefited a lot from all these tools, for instance, different simulations could provide right conditions that enable a forming process, or give information that cannot be observed in the real forming experiments (such as the failure and twist of yarns or fibers). Moreover, the simulation results can be used to predict the permeability of the preforms [BIC 97, LOI 08].

1.4.1 Kinematic approach

Kinematic approach is an early method to anticipate the shape of draped fabric. Mack and Taylor [MAC 56] firstly proposed this algorithm in which they assumed that the yarns are pinned at the cross points and are inextensible and incompressible (thus can only rotate around the hinge points). After their work, a great deal of sequential studies were carried out. *E.g.*, different boundary conditions are considered to get more complex draping shapes [Van 91, YAN 14] ; New algorithms are found to improve the computational efficient [AON 94, EBE 97, IVA 01, IVA 02]. The very basic thinking of kinematic approach is easy to be understand. The textile fabric is considered as a fishnet (for this reason, kinematic approach is also called Fishnet Algorithm). To locate the cross points on the dome structure (FIG. 1.30), the calculation always starts from a point and spreads progressively to the neighbor nodes. The mapping methodology to determine the coordinates of the current node is the focus of kinematic approach technology. An example in FIG. 1.30 shows how to locate the unknown point C from the known points A and B. According to the basic assumptions, the location of C fulfills the following equations :

$$\widehat{AC} = \widehat{OB} \tag{1.12}$$

$$\widehat{BC} = \widehat{OA} \tag{1.13}$$

$$C \in S_{mold} \tag{1.14}$$

where $\widehat{MN}$ means the surface distance of M and N ; S_{mold} is the surface of the mold. Kinematic approach is fast and stable, thus is widely accepted in industry. Nevertheless the drawbacks are also very obvious, since it ignores the specific mechanical properties of the reinforcement thus can only give a rough description of the forming process. Moreover, its application is limited to 2D fabric since the kinematic approach technology on 3D fabric is still immature and expensive.

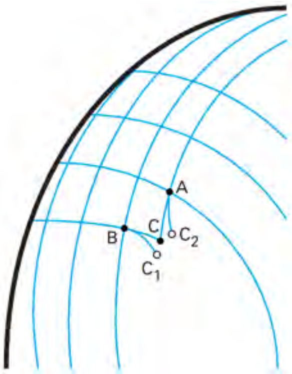

FIGURE 1.30 – An example for fishnet algerithm

1.4.2 Finite element approaches

Finite element (F.E.) technology has been used to study the reinforcement deformation for decades. It has many advantages over kinematic algorithm : firstly, it is capable of considering detailed mechanical properties which means the results are more reliable ; secondly, F.E. method has wider application since it is adapted to quite complex deformations ; most importantly, F.E. methods could provide results at different scales (FIG. 1.31) to fulfill different research requirements, *e.g.*, micro scale simulations are used to find out fiber-level phenomena [VAN 96, IVA 01, BAH 04, DUR 05, LAD 06, MIA 08, DUR 10, LAT 11, DUR 12, MAR 12, El 14, SAI 16] while results of mesoscale [MIE 04, BOI 05a, PIC 06, LOM 07, BAD 07, BAD 08c, BAD 08b, BAD 09, TAB 14] take into account the interactions between elementary tows, if the phenomenon in the fabric level is interested, macroscale studies [BOI 05a, GOW 97, HAM 08, HAM 09, PEN 02, PEN 04, WAN 97, XUE 03, YU 02] can be carried out based on different homogenized approaches.

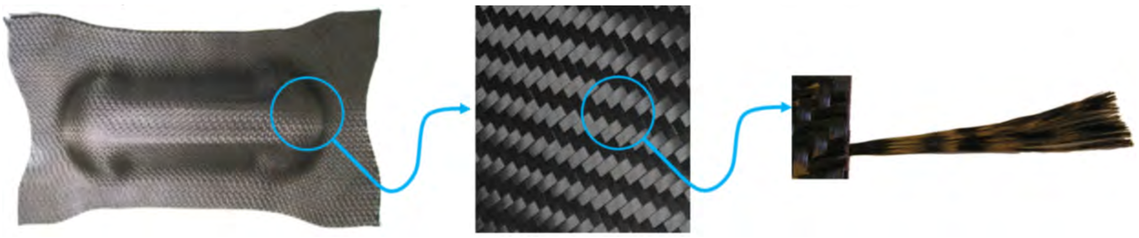

FIGURE 1.31 – Analysis of composite at differente scale [NAO 15b]

Macroscopic F.E. modeling

The macroscale is the scale of fabric product (FIG. 1.32). The reinforcement is considered as continuous structure with specific properties, which is quite dependent of the performance of yarns at mesoscale and fibers at microscale (*e.g.*, the fabric usually has small deformation in warp/weft directions but large angular variation between warp and weft yarns). Some macroscale F.E. models have been developed over the last few decades based on different homogenization processes, and most of them are realized in membrane or shell elements. For instance, Yu *et al.* used a non-orthogonal model based on force analysis along yarn directions [YU 02]. Boisse.P *et al.* [ALL 11] proposed a triangular shell element for the simulating of textile composite forming ; Cao J *et al.* developed two continuous models based on transformation approach [PEN 02] and energy approach [XUE 03], respectively.

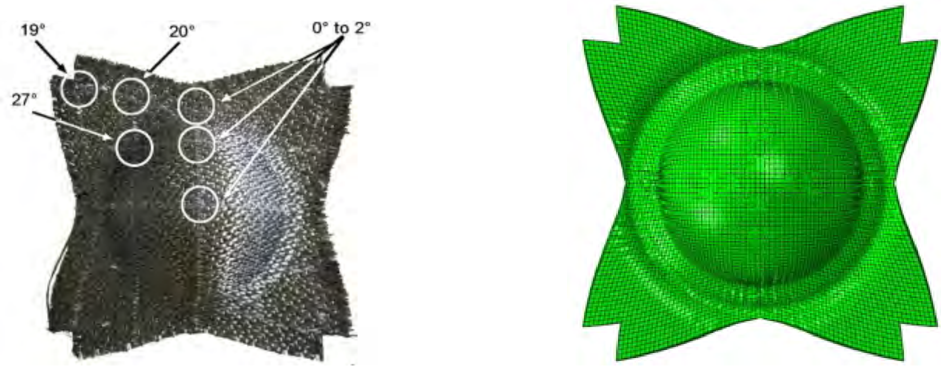

(a) Stamping of 3D fabric **(b)** Stamping simulaion of 3D fabric [CHA 12]

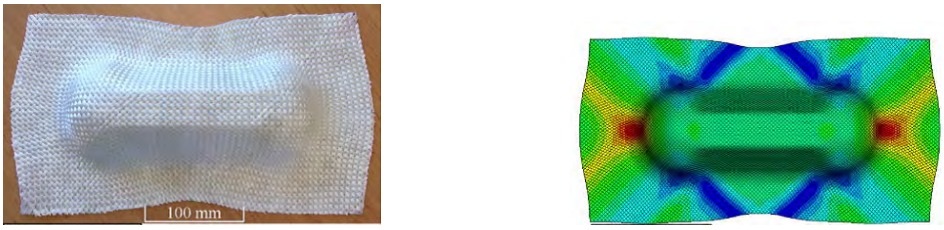

(c) Stamping of 2D fabric **(d)** Stamping simulation of 3D fabric [KHA 10]

FIGURE 1.32 – Macroscopic study of composite stamping

Mesoscopic F.E. modeling

Mesoscale concerns the yarn-level phenomenon, and the yarn is modeled as 3D continuum with specific properties. Some necessary work to build up mesoscopic model have been figured out by E. Vidal-Salle *et al.* [VID 11]. The first step is geometrical modeling which means to find a Representative Unit Cell (RUC). The selection of an RUC is a multi-choice problem (FIG. 1.33a), and a good choice may reduce the complexity to define boundary conditions and improve the computational efficiency. For the three RUCs in FIG. 1.33, RUC2 and RUC3 are smaller than RUC1, which leads to shorter computation time. Furthermore, comparing RUC2 and RUC3, the former one is preferable when it comes to the definition of periodicity boundary conditions. The reason is that RUC2 is embraced by material boundary (FIG. 1.33b), while in RUC3, the boundary consists of material and geometrical ones. More detailed explanation can be found in Badel's work [BAD 07]. The 3D geometry of the selected RUC can be built up by different technologies. There are various of accesses for this purpose : the first choice can be some geometry modelers such as TexGen [LON 11] and WiseTex [LOM 11], which are developed to generate textile structures conveniently. They give a reasonable description of the internal geometry of textile fabric and both of them are accessible on the internet ; A more precise way is based on the *x*-ray computed tomography technology [NAO 14], which is non-destructive and can reconstruct the internal geometry of textile reinforcement in 3D. The fabric is scanned by *x*-ray devices, and image processing algorithms are used to gain the 3D structure from tomography data ; The third choice may be a sweeping modeling methodology [HIV 08], in which the yarn section or sections are swept along the yarn trajectory to generate the yarn geometry.

The second step to build up a mesoscale model concerns the constitutive relation. Two examples that have been extensively used on mesoscopic simulations are hypo elasticity and hyper elasticity. They relate stress and strain and allow taking into account material non-linearity. The related parameters can be measured from tension test, shear test, compaction test,*etc.* A mesoscopic simulation result is shown in FIG. 1.34, in which the outlines of yarns are clear to be observed. The simulation is verified by a tomography test (FIG. 1.34a).

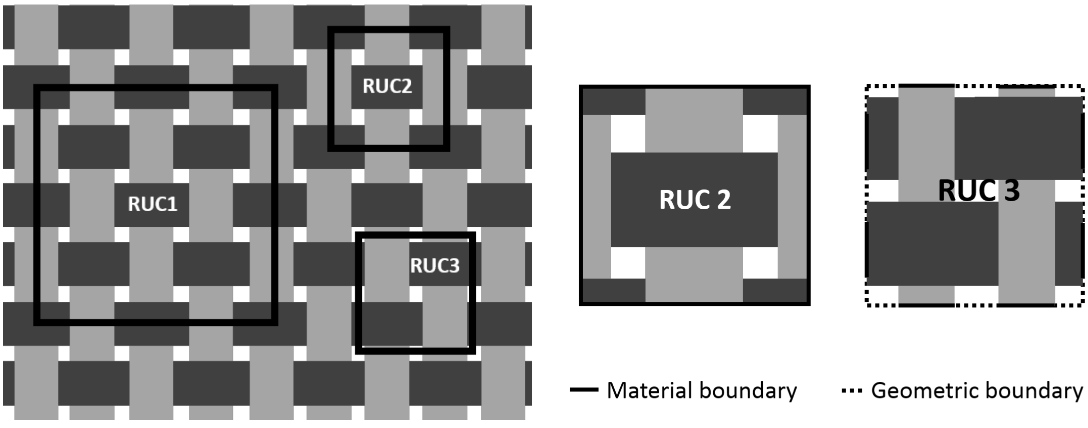

(a) Three RUCs for plain fabric **(b)** Two boundary types for RUC

FIGURE 1.33 – The selection of RUC for the plain fabric

Microscopic F.E. modeling

The microscale concerns the fiber-level phenomena such as fiber twist, transverse property of the fibers, as well as the stochastic nature of fiber strength. The most obvious

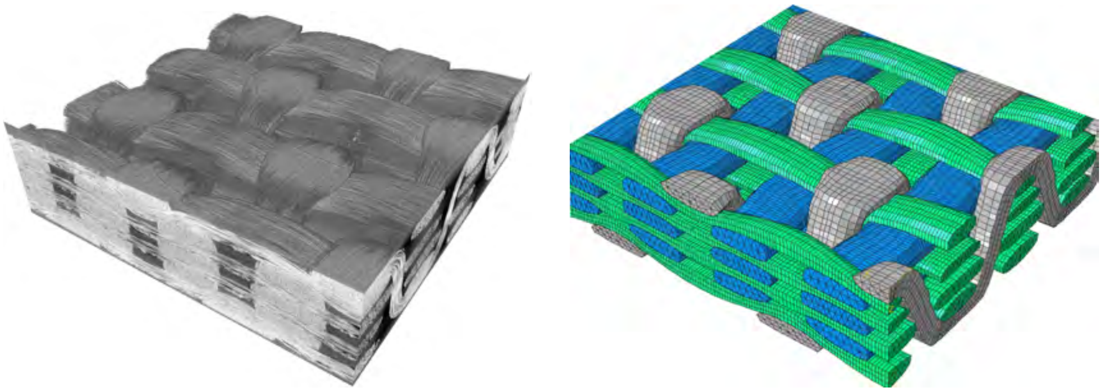

(a) Tomography of compacted fabric **(b)** Mesoscopic simulaiton of compaction

FIGURE 1.34 – Mesoscopic simulation of composite [NAO 15a]

advantage of microscale simulation over macroscale and mesoscale ones is that it only requires the characteristics of the fibers, instead of assuming some deformation modes to describe the behavior of fabric (as is done in mesoscale/macroscale models). It is found that the key issue is how to taking into account the contact-friction between fibers. To solve this mechanical problem involving a large number of contacts, some researchers found efficient approaches based on F.E. technology.

Durville [DUR 05, DUR 10] developed an efficient microscopic approach in which each fiber is described in contact with its neighbors. This approach is based on implicit F.E. code that was specially developed for the study of mechanical behavior of entangled materials. He computed the initial configuration of the fibrous structure with a special process which gradually moves fibers until satisfying the chosen weaving pattern. The trajectories of all the fibers can be found by solving a global equilibrium that offers an accurate geometrical information of the arrangement of fibers and tows in the fabric. The process is illustrated in FIG. 1.35a and FIG. 1.35b. Once the initial geometry has been obtained, different loading cases can be applied to the geometrical model to identify the mechanical properties. FIG. 1.35c and FIG. 1.35d provide two example of the loaded model. The advantage of this model is that it requires few parameters (mechanical properties of fibers and geometrical description of the weaving pattern) [DUR 10, DUR 11], but can be very helpful to provide information to mesoscale or macroscale study, *e.g.*, providing the initial configuration of fabric, and so on.

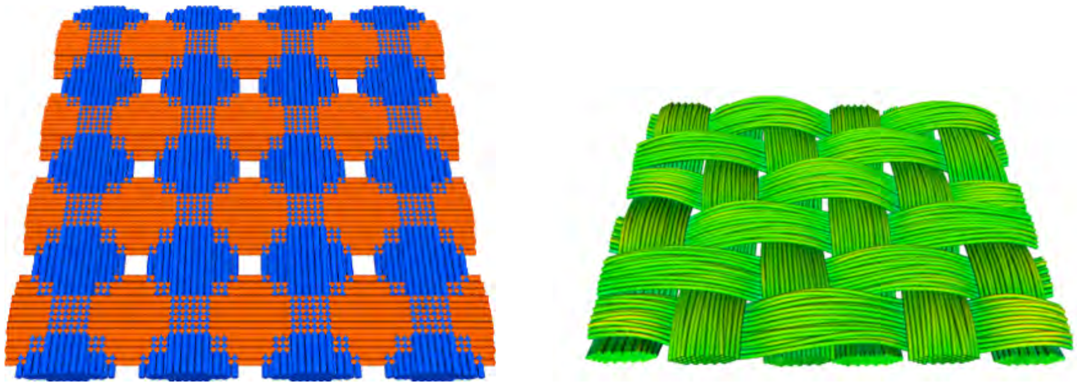

(a) Initial state **(b)** Micro model

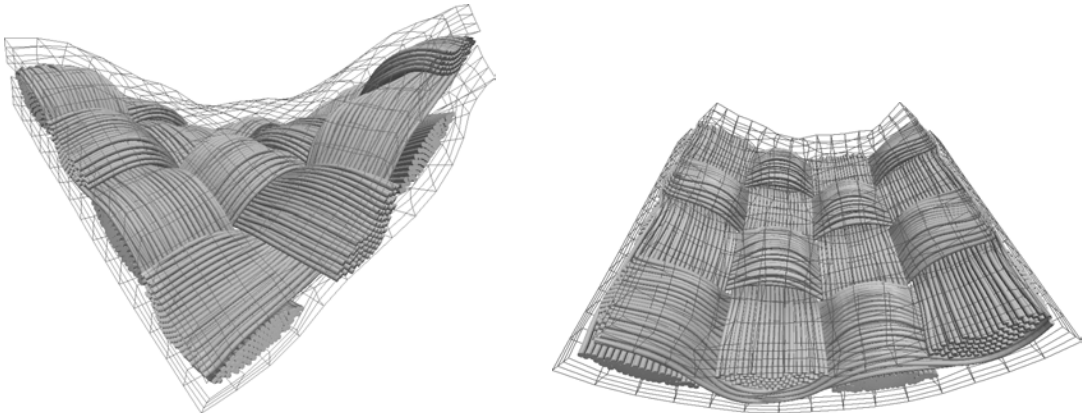

(c) Globle twist simulaion **(d)** Globle bending simulaion

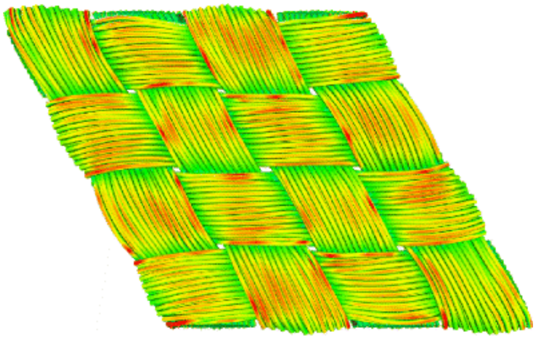

(a) Globle shear simulaion

FIGURE 1.34 – Microscale model for textile reinforcement [DUR 10, DUR 11]

Chapitre 2

Tomography technology for textile reinforcement

Nowadays tomography technology has become an effective tool to study the composite materials. It plays quite an important role in this study thus deserves special presentation. Section 2.1 introduces the physical principles of tomography technology, and several common operators used to process tomography data. The rest of this chapters introduces several important applications of tomography on tapas fabric in this study : section 2.2 shows how to build up the geometric model of mesoscopic scale for tapas fabric ; section 2.3 introduces how tomography is used to observe the nesting phenomenon in fabric stacks, the transverse expansion of the yarn, etc.

Contents

2.1 Introduction of tomography

Tomography is a non-invasive technology that allows the reconstruction of the inner structure of an object, thus has found wide application in medical and the industrial field, *e.g.*, nondestructive testing and reverse engineering. The physical excitation to realize tomography can be ultrasonic, magnetic field, x-ray, γ-ray and electric field [BAR 00], among which the x-ray is the most used in the field of industrial non-destructive testing (NDT). This section presents x-ray tomography [STO 99, BAR 00, DES 05, STO 08, HSI 09, HER 09, MAI 14]. The physical principle and usual setups will be presented firstly. Then several mathematical morphology technologies will be discussed, since they are normally used to pre-process the raw data of tomography.

2.1.1 Physical principle

An illustration that explains the principle of x-ray tomography is shown in FIG. 2.1. A complete system consists of three essential parts [BAR 00, MAI 14] : the x-ray source, the rotation stage and the x-ray detector. The line scanner in FIG. 2.1a was usually used in the early time, its scanner process can be time consuming since the detector is a mono one ; Cone scanner has a plate detector and the x-ray source could give off ray sets at the same time, thus obviously improves the efficiency of tomography test. All the tests in this study are done in the device in FIG. 2.1b.

A simple diagram is exhibited in FIG. 2.3 to explain how tomography works. The intensity of the x-ray is reduced because the beam is passing through the matter, and the photons are absorbed. The attenuation could be detected by the ray sensor. A distribution map of attenuation coefficient μ is obtained according to Beer-Lambert law :

$$\frac{N}{N_0} = e^{-\int_{path}\mu(x,y_1)dx} \tag{2.1}$$

where N_0 is the number of photons emitted by ray source ; N is the photons detected by ray detector and it depend on the thickness only if the material is homogeneous. Rotating the object to obtain a full set of radiographs corresponding to a 360^o rotation. From this data set, EQ. (2.1) can be written for each pixel of each radiography, which gives a linear function of the local attenuation coefficient in each voxel :

$$ln\left(\frac{N_0}{N_{ij}}\right) = -\sum_k \mu_{ik} \tag{2.2}$$

where N_{ij} is the number of transmitted photons recorded by the detector j in radiograph i, and μ_{ik} is the total value of local attenuation coefficient of each voxel k summed along the beam which reaches the detector point j [BOI 11]. EQ. (2.2) provides an equation set to get the attenuation coefficients for all material points of scanned object.

The most important parameter for a tomography test is the resolution. A compromise between the resolution and size of the sample should be made before the experiment is carried out. Specific to textile reinforcement, a resolution value of $10 \sim 20\ \mu m$ is sufficient

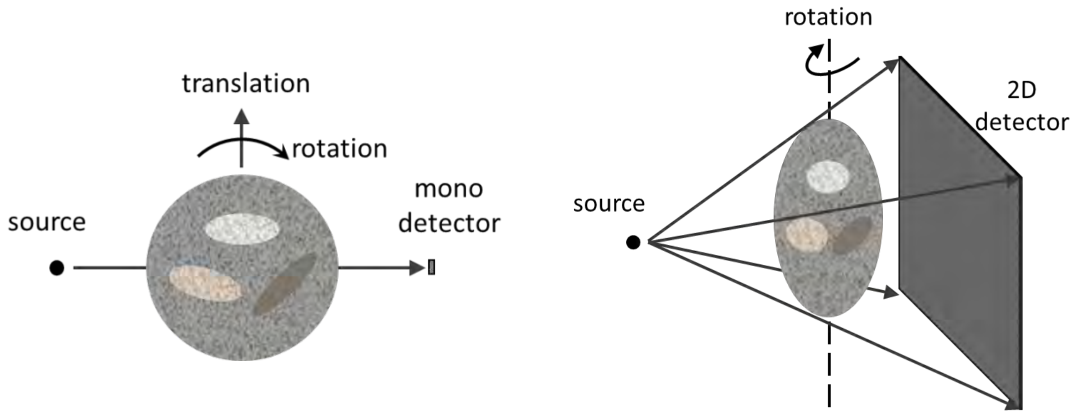

(a) Line beam scanner **(b)** Cone beam scanner

FIGURE 2.1 – Different kinds of $x - ray$ principles

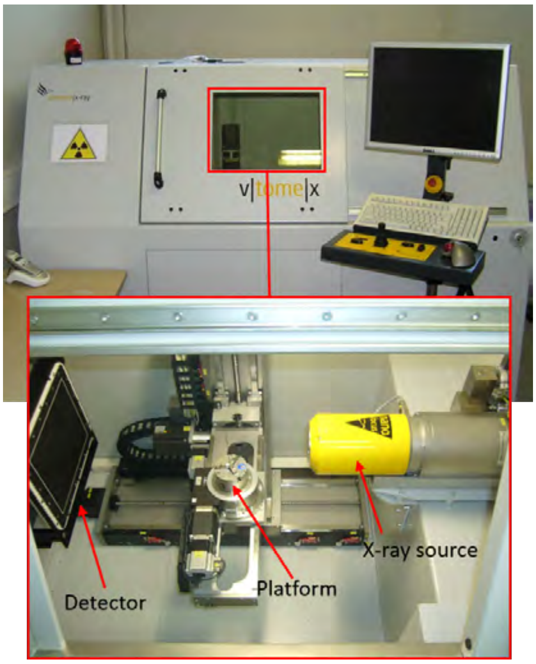

FIGURE 2.2 – Devices (LAB MATEIS,INSA de Lyon) used in this thesis

to obtain yarn level views, as is shown in FIG. 2.4a, the outlines of the yarns are quite clear. Smaller resolutions around 5 $\sim$10 μm are also frequently used for the purpose of the microscopic observation of composite fabric. Generally, when the resolution is below 4 microns, fibers can be distinguished individually.

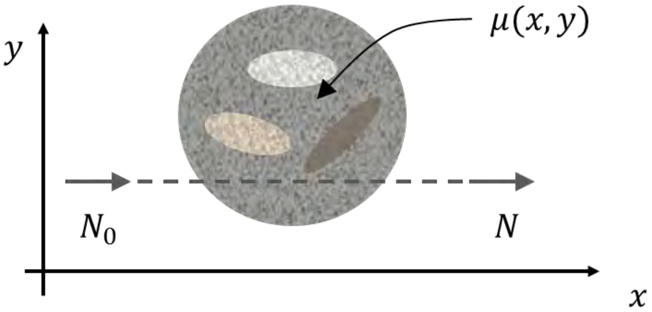

FIGURE 2.3 – Diagram to explain the physical principle of tomography

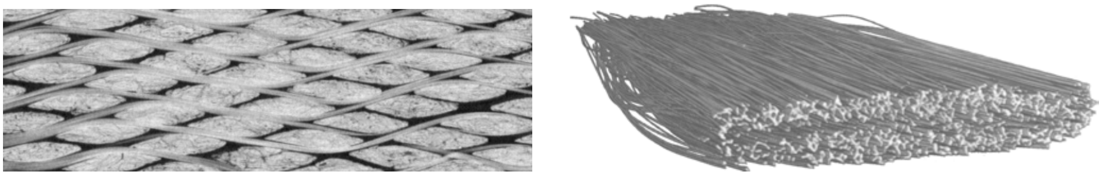

(a) Mesoscale tomography **(b)** Microscale tomography

FIGURE 2.4 – Two tomographies of composite materials with different resolutions

2.1.2 Mathematical morphology

To extract useful information from the raw data of tomography, various image processes could be used. They are introduced as follows :

Binarization. Binarization operator is the base of other image processing operators. It creates binary images from grayscale or color ones. The intension is to delete multifarious details in the image while keeping the most important information. After binarization, the tomography data is compressed in size and becomes easier to be further processed. In a binary image, each pixel has a value of 0 or 255, corresponding to black and white, respectively.

Dilation. Dilation is one of the most basic operations in mathematical morphology. The objective is to repair the small spurious gaps and holes of the structure in the image according to various dilation algorithms. As can be seen in FIG. 2.5b. This operation can gradually enlarge the boundaries of the regions of white pixels, so the area of the foreground pixels grows in size.

Erosion. Erosion is an opposite operation of dilation. Its effect is eroding away the small boundaries of white pixel regions as well as eliminate the small clumps of undesirable pixels such as salt-and-pepper noise (FIG. 2.5c). Thus the white areas becomes smaller after erosion.

Opening. Opening is the combination of dilation and erosion. In fact different open operators could have a flexible number of dilation and erosion operators in different orders, according to different algorithms. However on the whole, the erosion prevails.

(a) An image before/after binarization

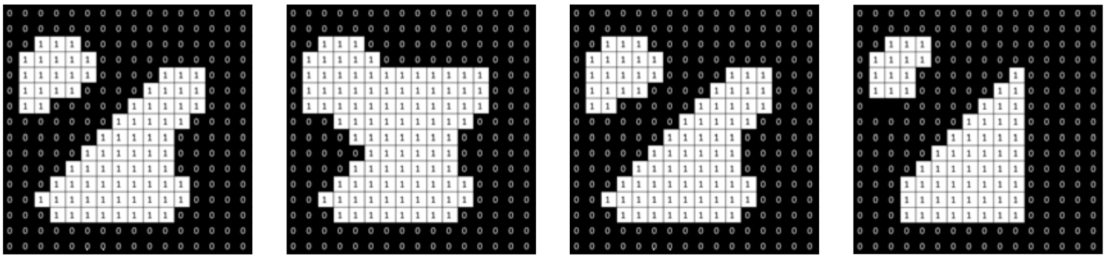

(b) A binary image before/after dilation **(c)** A binary image before/after erosion

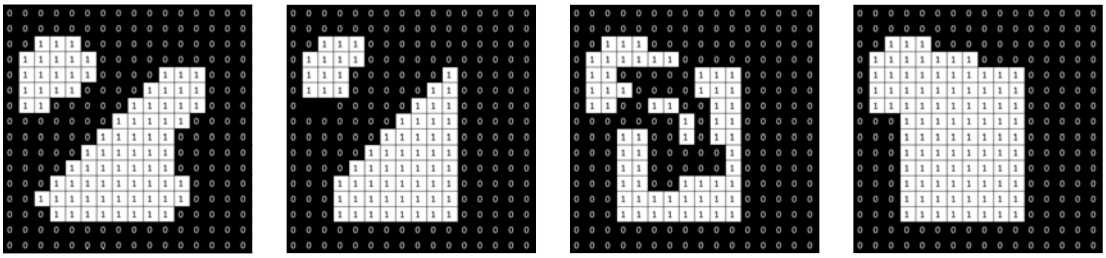

(d) A binary image before/after opening **(e)** A binary image before/after closing

FIGURE 2.5 – The common mathematical morphologies

So the effect of opening operator is somewhat like erosion but is less destructive. An example is shown in FIG. 2.5c.

Closing. Closing also comes from the alternative usage of dilation and erosion operators, however dilation operator prevails. So closing is like the dilation but is less destructive (FIG. 2.5e).

2.2 Geometrical modeling with tomography data

The geometrical model in this thesis is built up using the tomography data, which is one of the most attractive applications of tomography experiment on composites. To built up the geometrical reprentative unit cell (RUC) for tapas fabric in FIG. 2.6, the computed tomography process [YOU 05, NAO 14, NAO 15a, NAO 15b] could be a choice since to a large extent, it is capable of preserving the details of the real configuration. Nevertheless it will be shown in 2.2.1that this methodology has limitation on RUC modeling : firsly, a RUC should be a reasonable balance between *precise* and *representative*, and too many details such as irregular convex hull reduces the representativeness of the geometrical mode ; what's more, it is expected to obtain the whole fabric by the repetition of RUC, and this puts forward special geometrical requirements on the boudaries of the RUC, but the

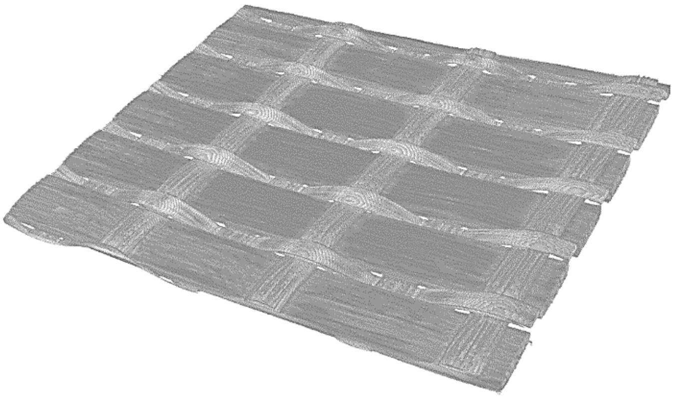

FIGURE 2.6 – The tomogrpahy result of tapas fabric

model from computed modeling technology cannot fulfill these requirements and should be modified. For these two reasons sweeping modeling technology [HIV 05, WEN 13, WEN 14, WEN 15] is chosen as a supplementation to improve the geometrical model. These two methodologies will be presented bellow and both of them are based on the tomography data in FIG. 2.6.

2.2.1 Computed tomography modeling

Computed tomography modeling is usually applied on the modeling of metal material. *E.g.*, Youssef [YOU 05] defined three essential processes to get a meshed model for cellular materials : the first step is the binarization and enhancement of grey radiographs ; followed by the definition of the solid boundary, in which a closed surface domain that bounds the solid volume is obtained ; the last step is meshing the solid structure with advancing front method. The last two steps can be replaced by transforming the voxels into hexahedron elements directly, this is known as voxel-element technique and do not require any additional expenses for mesh generation. The shortcoming is that when the voxel is small comparing with the whole structure, the massive mesh will slow down the simulation. The modeling methodology will come across a problem when it comes to composites. An additional step is required to separate a warp yarn and a weft yarn at their crossing area. Naouar [NAO 14, NAO 15a, NAO 15b] solves this problem by means of a segmentation process. Segmentation refers to partitioning a radiograph into different sets of pixels. The segmentation is realized on account of an important value that is called structure tensor [JEU 08, REZ 12] :

$$A = \begin{bmatrix} \langle f_x, f_x \rangle_w & \langle f_x, f_y \rangle_w \\ \langle f_x, f_y \rangle_w & \langle f_y, f_y \rangle_w \end{bmatrix} \tag{2.3}$$

where f_x and f_y are the partial spatial derivatives of brightness distribution $f(x,y)$ in the image, and $\langle m,n \rangle_w$ is the short form of $\iint w \cdot m \cdot n dxdy$. The local orientation can be extracted from structure tensor through the following expression :

$$\theta = \frac{1}{2} arctan \left(2 \frac{\langle f_x, f_y \rangle_w}{\langle f_y, f_y \rangle_w - \langle f_x, f_x \rangle_w} \right) \tag{2.4}$$

where θ is the local orientation of the pixel in the image. The pixel points in a image can be divided into different groups according to their local orientation magnitude. After segmentation, some traditional image operators (as has been presented in 2.1.2) are applied to smooth the tomography data, followed by skeletonization, which gives the information of neutral axis of each yarn [CAL 68, BOR 99]. At last, the polygonal surface is generated and the advancing front mesh generation method [FRE 98] is chosen to get the meshed F.E. structure. Computed tomography methodology is an automatic technology that can reduce the man-made interference to a large extent. It reflects the realistic structure of the scanned material. Naouar [NAO 14, NAO 15a, NAO 15b] has proved the efficiency of this modeling tool. In spite of this, when the expected model is a RUC one that is small and representative, two problems arise.

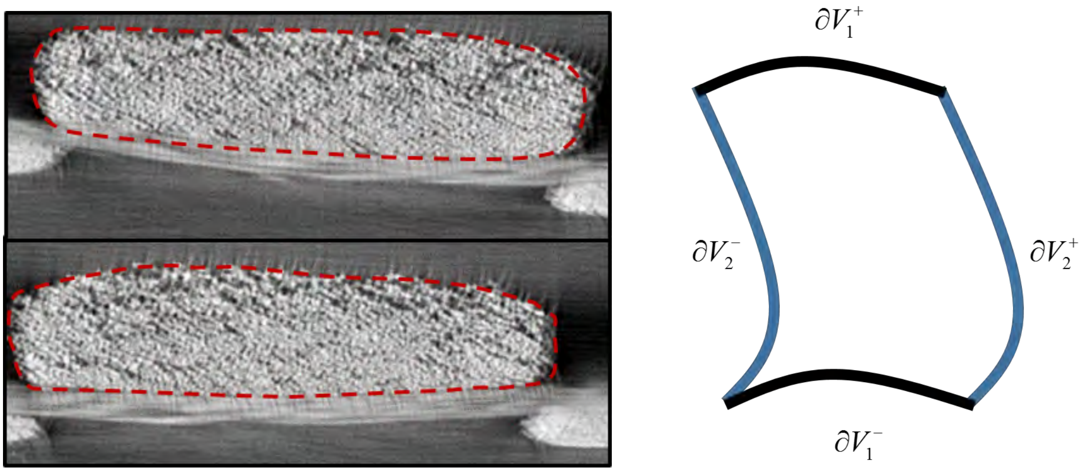

(a) Irregular convex hull on the cross section

(b) The corresponding boudaries should have same outlines

FIGURE 2.7 – Two problems when modeling the RUC with computed tomography methedology

Firstly, model of computed tomography preserves too much details (such as irregular convex hull of warp yarn in FIG. 2.7a) and makes the RUC model too individual to be representative.

Secondly, it is expected to construct a periodic structure by the repetition of RUC, which means the corresponding boundaries should have the same outlines. *E.g.*, in FIG. 2.7b, ∂V_α^- and ∂V_α^+ should have the same shape. This point cannot be guaranteed in the computed tomography methodology.

2.2.2 Sweeping modeling methodology

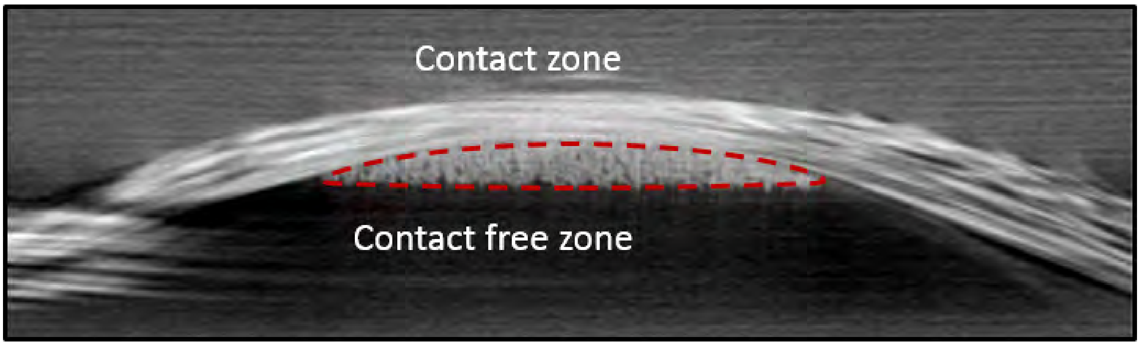

(a) Section of yarn

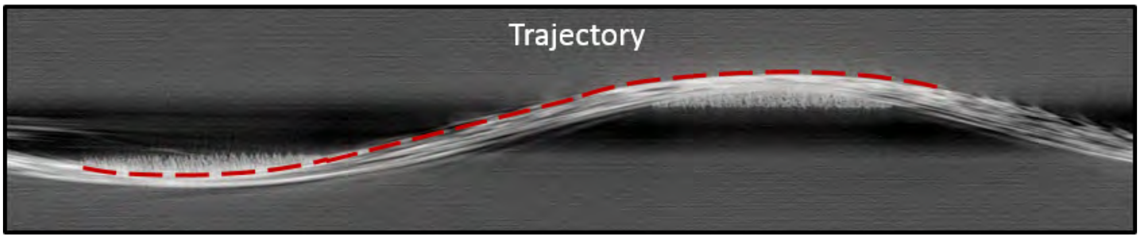

(b) Trajectory of yarn

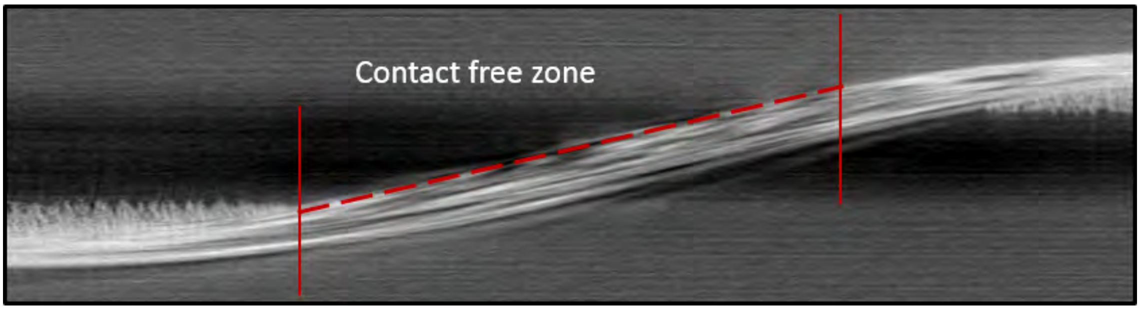

(c) Constact part on the trajectory

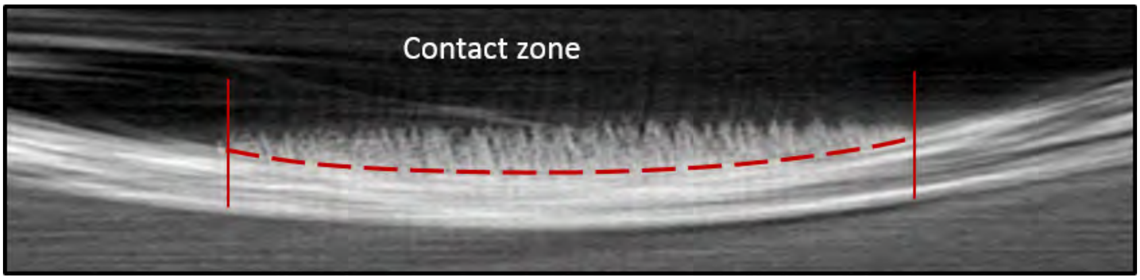

(d) Contact free part on the trajectory

FIGURE 2.8 – Different zones to be considered in a geometrical medeling process

Sweeping modeling proposes to obtain the geometrical model by sweeping section along a trajectory. There are different ways to measure the geometry of the yarn, *e.g.*, direct measurement with ruler or optical measurement based on high quality photos. They are sample but have no access to the sections/trajectories inside the fabric. Now in this study we can use tomography technology to measure all the needed parameters precisely.

The early models assumed that the yarn has a constant section along the trajectory, which makes the modeling process fast and easy. As to the trajectories of different yarns, they are considered to be sinusoids, splines, polynominals, *etc.* [LOM 11]. An obvious drawback of this kind of treatment is that the contact zone is not well considered and designed. Hivet *et al.* [HIV 05] improved the sweeping methodology. Firstly he found that the section of a yarn is affected by the contact condition (FIG. 2.8a), so it should adapt different sweeping sections according to the contact circumstance along the sweep path ; secondly, as to the sweep path, which is the mean line of the yarn (FIG. 2.8b), is studied separately : the contact part on the trajectory has the same conic surface as the contact curve of the cross section (FIG. 2.8c) ; and the contact free part is assumed to be straight (FIG. 2.8d) because the bending stiffness of the yarn is small. The model created by this technology has been proved close to the real structure. So it is used in this study to obtain the geometrical model, along with the computed tomography technology.

2.2.3 Geometrical modeling of tapas fabric

As is discussed, in this study, a combination process of these two methodologies are carried out to build up the geometrical model for tapas fabric. Firsly, the 3D geometrical model created by computed tomography method. An example of warp yarn is shown in FIG. 2.9b, and it is very close to the tomography radiography in FIG. 2.9a, which has some irregular convex hull. Then a cross section based on the parameterization theory of Hivet [HIV 05] is used in CAD software to modify the warp model, after which the irregular edge becomes regular (FIG. 2.9c). Moreover, it is noted that the RUC should fulfill the geometrical periodicity, as is exhibited in FIG. 2.9, there are totally 8 groups of symmetry boundaries. This requirement for the geometrical symmetry should be fulfilled when the model from computed tomography is modified by CAD software. The final geometry of the RUC for tapas fabric is exhibited in FIG. 2.9. As can be seen, the type of element is C3D6. For two reasons, the size of elements in binder yarns and weft yarns are smaller that those in warp yarns : firstly, the size of binder and weft yarns are small, so they need fine mesh to reflect their geometrical shapes ; secondly, the deformation of binder yarn is relatively complex, which calls for the fine mesh.

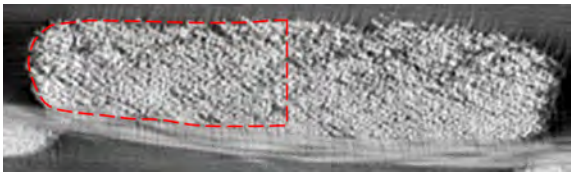

(a) The sectional shape of warp yarn in the tomography image

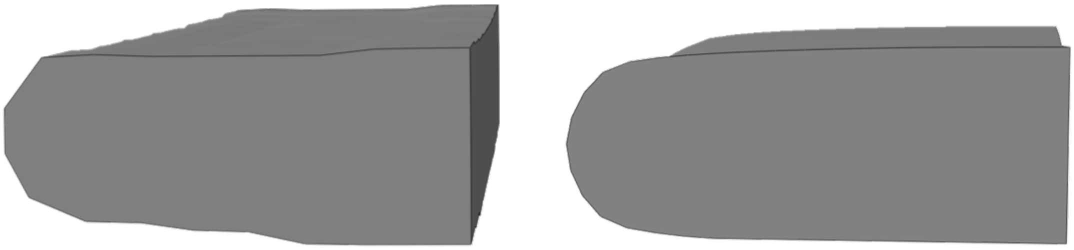

(b) The warp yarn model from computed tomography

(c) The warp yarn model from computed tomography is improved by average section shape

FIGURE 2.9 – The geometrical model of warp yarn generated from computed tomography modeling method is improved by sweeping modeling methodology

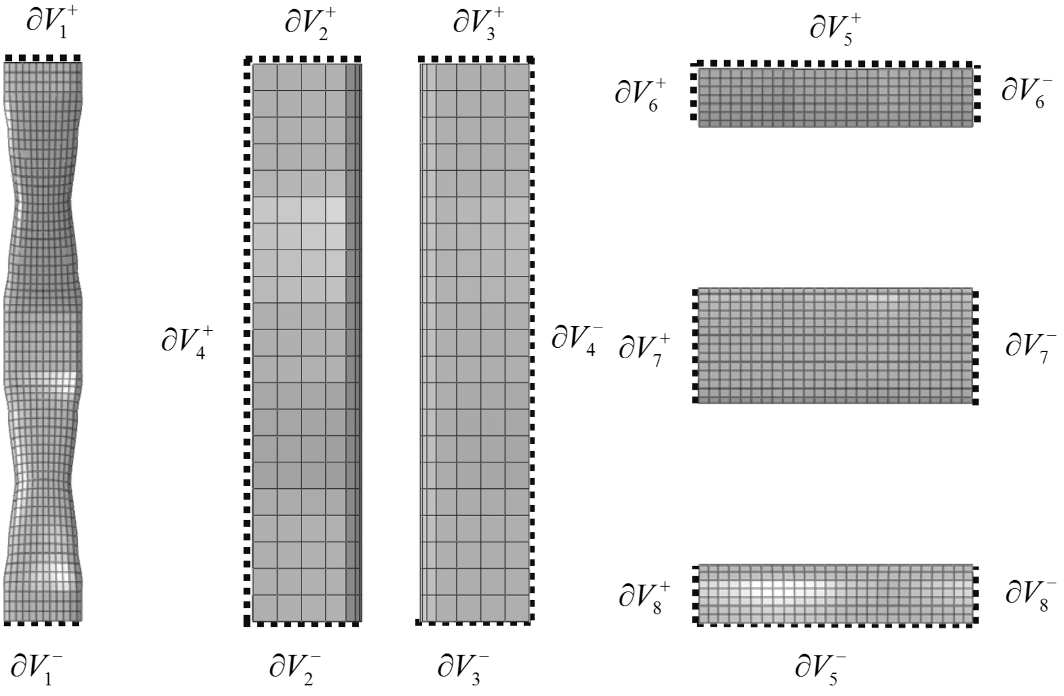

(a) Binder yarn

(b) Warp yarns

(c) Weft yarns

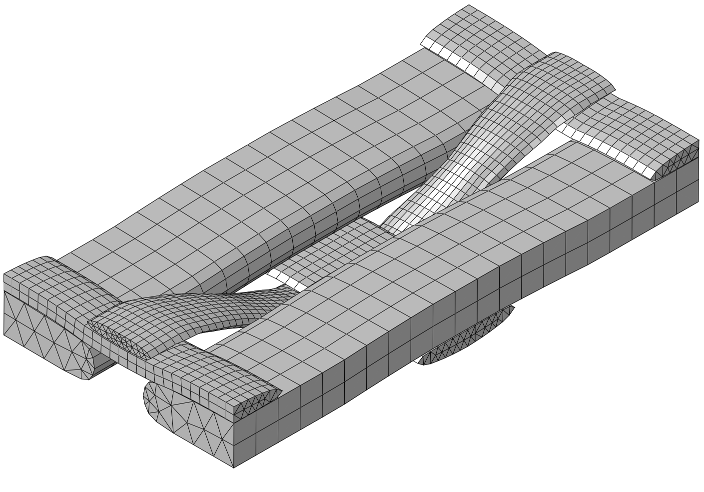

(**a**) The RUC model for tapas fabric

FIGURE 2.9 – The RUC for tapas fabric and its periodicity boundaries

2.3 Other applications of tomography technology

Besides the geometrical modeling, tomography experiments also finds its applications in other aspects. When it is applied to observe the loaded fabric, *x*-ray scanning gives details circumstance of the deformed yarns and fibers, thus can provide support to constitutive studies. This section provides several examples such as observing the compaction and shear of the fabric as well as the transverse expansion of the yarn.

2.3.1 Observation of the nesting phenomenon

Nesting is a typical internal phenomenon that cannot be observed directly. It has been mentioned in section 1.3 when the compaction deformaiton of the composite reinforcement is discussed. The compaction experiment tests on tapas fabric have shown that nesting between layers of fabric will obviously affects the compaction stiffness. *E.g.*, for tapas fabric, the layout of $0^o/0^o/0^o/0^o/0^o$ has a smaller stiffness curve than the one of $0^o/90^o/0^o/90^o/0^o$. This is different with the satin or other balanced fabric (*e.g.*, for satin the circumstance of $0^o/45^o/0^o/45^o/0^o$ has the smallest nesting and the largest compaction stiffness [NGU 13]). The *x*-ray tomography tests are carried out here to get the internal access to the nesting phenomenon.

The fabric is the compacted tapas reinforcement, and the device is from LAB MATEIS, INSA de Lyon. Different with the tomography operation on unloaded fabric, the compacted fabric should be fixed by devices in order to keep a constant deformation state when scanning is ongoing. The devices should be well designed in order to adapt to the limited space in the tomography machine (FIG. 2.10). The fabric is compressed by two plexiglas plates which are fixed by screws instead of normal clips, for the sake of a

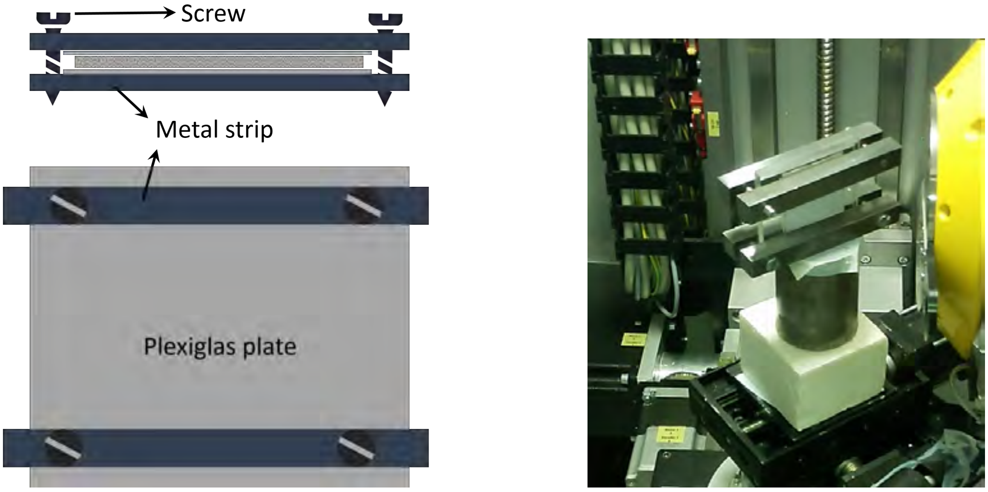

FIGURE 2.10 – The experimental setup for the tomography of compacted tapas stacks

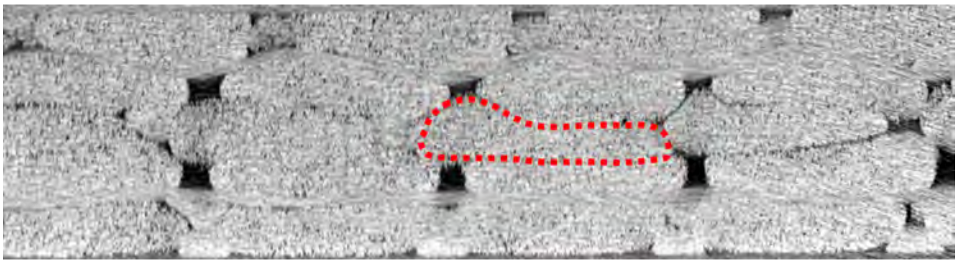

(a) $0^o/0^o/0^o/0^o/0^o$

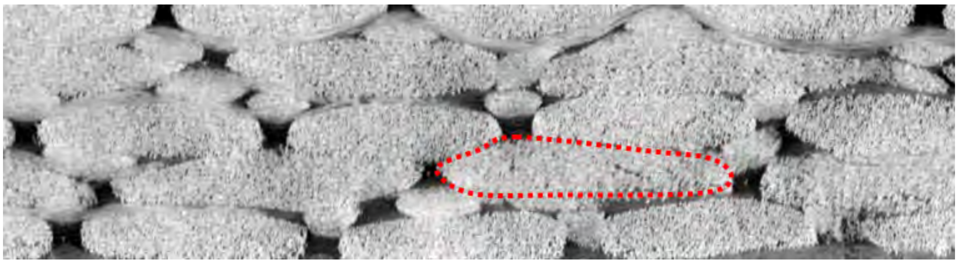

(b) $0^o/45^o/0^o/45^o/0^o$

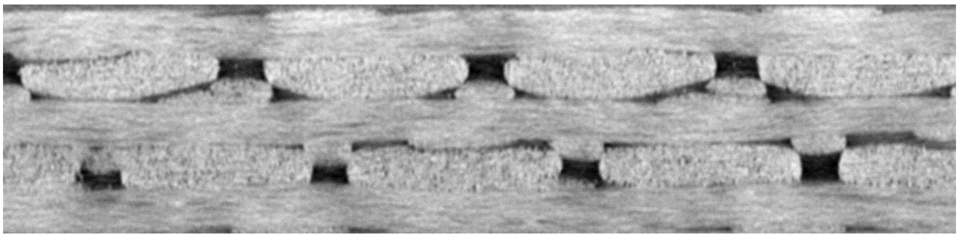

(c) $0^o/90^o/0^o/90^o/0^o$

FIGURE 2.11 – Tomography comparison of the nesting on different layouts of fabric

large compression force. The center part of the device is made of plastic which has small influence for the propagation of x-ray.

As can be seen in FIG. 2.11, the nesting in the layout of $0^o/0^o/0^o/0^o/0^o$ is very clearly observed. The fabrics fill the void of the adjacent fabrics. For the layout of $0^o/45^o/0^o/45^o/0^o$, since the yarns' orientations do not coincide with the orientation of the void in the adjacent fabric, the nesting level is reduced. When the fabric layout becomes $0^o/90^o/0^o/90^o/0^o$, as can be seen, the nesting almost disappears. This explains why the layout of $0^o/90^o/0^o/90^o/0^o$ has the largest compaction stiffness in FIG. 1.29b in section 1.3. This phenomenon will be further studied in chapter 4 by F.E. simulations.

2.3.2 Observation of shear deformation

Shear is a normal but important deformation mode for fabric. As is discussed, it affects the drapability of the fabric, as well as the generation/development of wrinkles. Direct observation could provide some useful data such as shear angles but has no access to the internal structure. So to understand the yarn and fiber level activities during the shear deformation, a NDT technology such as x-ray scanning method can be helpful. The part introduces two kinds of observations of the sheared fabric, from mesoscale and microscale respectively. The mesoscale one is on the tapas fabric and the microsopic one is from the work of Badel [BAD 08a].

Mesoscale tomography observation of sheared tapas fabric

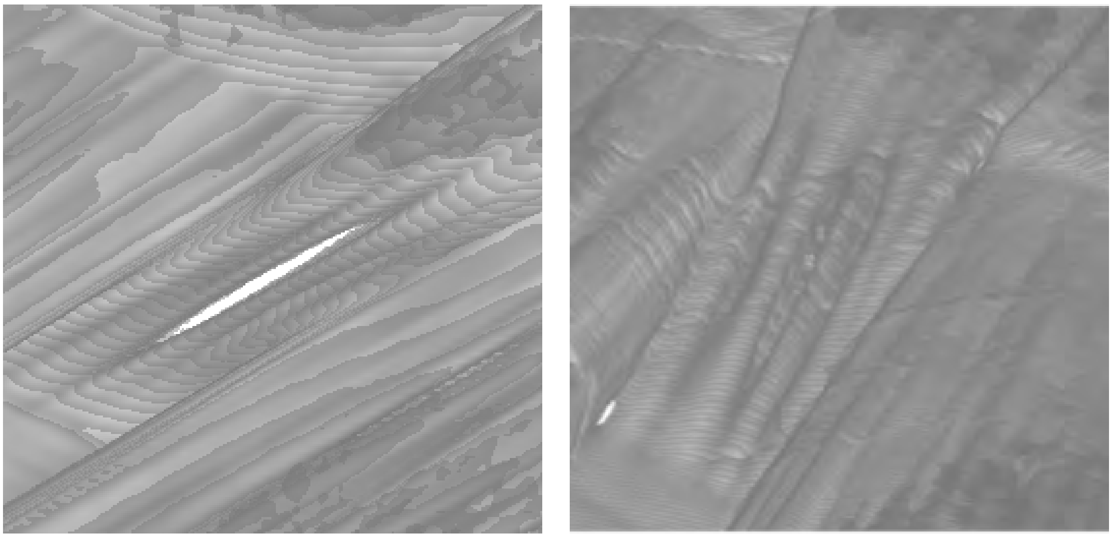

(a) Gap inside the yarn from the tapas fabric with in-plane shear **(b)** Wrinkles on the surface of the yarn from the tapas fabric with in-plane shear

FIGURE 2.12 – Mesoscale observation of tapas fabric with an in-plane shear angle of 30.9^o)

The sample of tapas fabric with a in-plane shear angle of 30.9^o is scanned in the tomography experiment. The resolution is 10 μm and the result is shown in FIG. 2.12. The performance of the yarns in a sheared fabric seems quite complex : the yarns seem to be twisted and compressed, and some wrinkles or gaps appear on the yarn surfaces or inside the yarns. These local deformations should be well considered in the simulation.

Microscale tomography observation of sheared tapas fabric

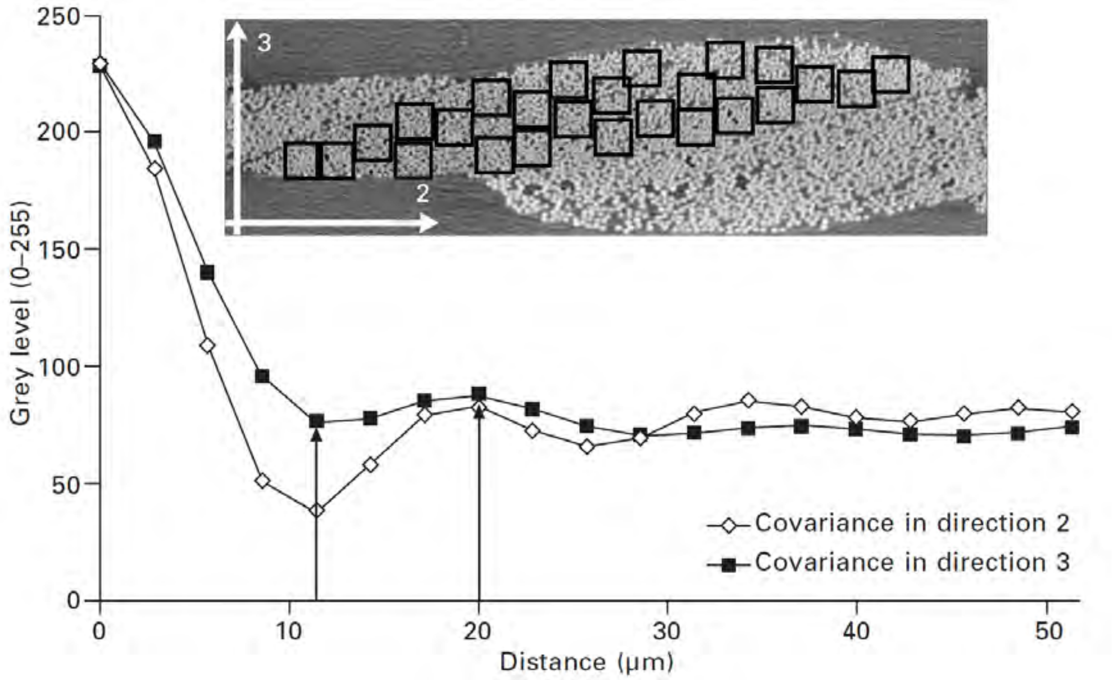

FIGURE 2.13 – Covariance analysis on the sheared glass plain weave [BAD 08a]

The microscopic tomography study could be also meaningful, since the understanding of the fiber level phenomenon is always helpful to establish a reasonable constitutive relationship. *E.g.*, Badel [BAD 07] observed the cross section in a sheared fabric (FIG. 2.13). The tomography radiography provides clear information about the location and distribution of fibers. It seems that the fibers distribute homogeneously in the sheared cross section, that is to say the cross section has a kind of isotropic performance during deformation. To verify this assumption, covariogram [BAD 08a, BAD 11] is carried out to provide information about the spatial distribution of fibers : firstly the image is converted into binary form ; then Fourier transform is carried out on the binarization image and the square of the Fourier results are computed ; finally, inverse Fourier transform from which histograms are plotted along two orthogonal directions. More details about this process can be found in [DOU 03]. Obviously the two covariograms look similar which validate the assumption of isotropic section. This conclusion will be used in chapter 3, when discussing the mesoscopic constitutive relationship.

2.3.3 Observation of the transverse expansion of yarn

Tomography is also used to observe the transverse expansion of yarn in this study. When a yarn is compressed along its longitudinal direction, it will have transverse expansion deformation. Although it has influence on the permeability of the deformed fabric, to the best of the author's knowledge, there are not much literature on it. This phenomenon will be well discussed in section 3.4, based on tomography technology. Two kinds of resolutions will be used : the resolution of 10 μm gives a mesoscopic conception of this phenomenon (FIG. 3.26b), while a smaller resolution of about 5 μm provides a quite clear view of the fibers (FIG. 3.25) in the yarn. As will been shown in chapter 3, both of these two observations are helpful to understand the transverse expansion phenomenon.

2.3.4 Calculation of the porosity

The forth example of the application of tomography is the calculation of composite porosity. The porosity of composite material is an important topic for the composite and has been studied by many researchers [DAN 92, BIR 04, LIN 08, KAS 10, TOS 13, CIN 13]. One reason is that the porosity level affects the mechanical properties such as shear strength. It has been found that the interlaminar shear strength decreases by 7 % per 1 % porosity [BIR 04]. For those composite used in the aircraft and cars, the porosity level is usually between 2.5 % and 5 %. In the early time, acid digestion and materialography are used to measure the porosity value, nonetheless their nature of destructive influence the precision. For this reason, KASTNER *et al* [KAS 10] managed to improve the detection precision and he found that x-ray tomography is a powerful non-destructive tool for measuring the volumetric porosity of composite reinforcement. An obvious periodicity can be found from this image, which also gives useful guidance to find the good representative unit cell. The average porosity value calculated based on this figure is about 3.2%.

2.3.5 Validation of simulation results

Last but not the least, tomography technology is applied widely to verifying the simulation result. No doubt that the traditional mechanical experiments such as compaction test plays the most important roles when verifying the simulation results. In spite of this, they cannot provide any information to verify the shape of deformed model, *e.g.*, the change of yarn cross-sections, the fiber level phenomenon such as fiber twist. So tomography is a complement to check or confirm the simulation. This geometrical tool has been used in many researches. In chapter 3 and chapter 4, all the simulations will be checked by tomography.

Chapitre 3

Mesoscopic mechanical model for textile reinforcement

There have been some publications and thesises about the hypoelastic mesoscale model for fibrous structures [HAG 04, BOI 05b, BAD 07, BAD 08b, BAD 09, NGU 12, NGU 13]. This previously proposed mesoscopic model will be introduced and improved in this chapter. Section 3.1 presents a special hypoelastic law that is adapted to the fibrous structure. Section 3.2 reviews the mesosopic model proposed in the previous works which includes four deformation modes (elongation, longitudinal shear, transverse compaction and transverse shear). In section 3.3 and section 3.4, two kinds of new deformation modes are developed separately : Longitudinal Compression (LC) mode is used to reflects yarn's small longitudinal compression stiffness, while Transverse Expansion (TE) mode aims to reflect the transverse expansion when the yarn is compressed longitudinally (so more precisely, it should be called the mode of Transverse Expansion arising from Longitudinal Compression). They are supplemented into the model proposed in the previous works, and the simulation results are apparently improved.

Contents

3.1 Hypo-elasticity law for fibrous material

This section introduces the stress updating framework used in the mesoscopic model proposed in the previous works for the composite. It is an specific hypoelastic law that is adapted to the fibrous nature of textile structures [BOI 05b, BAD 07].

3.1.1 Continuum mechanics

The use of the behavior law in large deformation problems need a description of movements that goes beyond the hypothesis of small perturbations. Before introducing the constitutive relationship for yarn material, several basic concepts about nonlinear continuum mechanics will be recalled.

Deformation gradient

In any deformation, the material particle initially located at the position $\underline{X}$ in space will move to its new position $\underline{x}$. Considering that the material cannot appear or disappear, the correspondence between $\underline{X}$ and $\underline{x}$ is one-to-one, we can always write the history of the location of a particle as :

$$\underline{x} = \underline{x}(\underline{X}, t) \tag{3.1}$$

Now consider two adjacent particles in the initial configuration, located at $\underline{X}$ and $\underline{X} + d\underline{X}$, in the current configuration we have :

$$\underline{x} = \frac{\partial \underline{x}}{\partial \underline{X}} \cdot d\underline{X} = \underline{\underline{F}} \cdot \underline{dX} \tag{3.2}$$

The partial derivative matrix in equation (3.2) is called the deformation gradient matrix, which is a powerful tool for nonlinear deformation study. All the deformation information of the continuum is included in $\underline{\underline{F}}$, *e.g.*, the change of the volume element or surface element can be expressed as :

$$dv = J \cdot dV \tag{3.3}$$

$$\underline{n_s} \cdot ds = J \underline{\underline{F}}^{-T} \cdot \underline{N_S} dS \tag{3.4}$$

where dV and dS are the volume and area elements in the initial configuration, and they become dv and ds in the current configuration ; $\underline{N_S}$ and $\underline{n_s}$ are the direction vectors of dS and ds ; the well-known Jacobian J is the determinant of $\underline{\underline{F}}$.

As the material behavior depends on the straining of the materiel instead of the rigid motion, the rigid motion should be distinguished by means of polar decomposition theorem :

$$\underline{\underline{F}} = \underline{\underline{R}} \cdot \underline{\underline{U}} = \underline{\underline{V}} \cdot \underline{\underline{R}} \tag{3.5}$$

where $\underline{\underline{R}}$ is an orthogonal tensor ($\underline{\underline{R}}^T = \underline{\underline{R}}^{-1}$) ; $\underline{\underline{U}}$ and $\underline{\underline{V}}$ are positive and symmetric.

Here it is worth mentioning the limitation of $\underline{\underline{R}}$: it is just an average rotation expression for the whole structure. To be exact, it is precise only for the principle directions :

$$\underline{n}_i = \underline{\underline{R}} \cdot \underline{N}_i \tag{3.6}$$

where $\underline{N}_i$ and $\underline{n}_i$ are relevant to the eigenvalue problem of $\underline{\underline{F}}$. As for the rotations of other directions, $\underline{\underline{R}}$ is an approximate expression. For materials such as concrete, metal and rubber, this limitation of $\underline{\underline{R}}$ is negligible.

However the property of composite reinforcement badly depends on the yarn's orientation, which means the orientation of the yarn should be strictly followed. So $\underline{\underline{R}}$ is not a appropriate choice on this occasion. Hagege and Badel [HAG 04, BAD 07] settled this problem with a new rotation frame, and more details can be found in section 3.1.3.

Deformation measurement

In the nonlinear continuum mechanics, there are several choices for the strain measurement. All of them can be derived from the stretch tensor $\underline{\underline{U}}$ or $\underline{\underline{V}}$, since they contain the complete deformation. In order to study the stretch deformation and rotation of the nodes in a deformed object, we can choose two elemental vectors in the initial configuration :

$$\begin{aligned} d\underline{u} \cdot d\underline{v} &= du_i dv_i = F_{ij} dU_j F_{ik} dV_k = dU_j F^T_{ji} F_{ik} dV_k \\ &= d\underline{U} \cdot \underline{\underline{F}}^T \cdot \underline{\underline{F}} \cdot d\underline{V} \\ &= d\underline{U} \cdot \underline{\underline{C}} \cdot d\underline{V} \end{aligned} \tag{3.7}$$

where $\underline{\underline{C}}$ is the right Cauchy-Green deformation tensor $\underline{\underline{C}} = \underline{\underline{F}}^T \cdot \underline{\underline{F}} = \underline{\underline{U}}^2$. And the variation of the vector production between the deformed configuration and the initial configuration is :

$$\begin{aligned} d\underline{u} \cdot d\underline{v} - d\underline{U} \cdot d\underline{V} &= d\underline{U} \cdot \underline{\underline{C}} \cdot d\underline{V} - d\underline{U} \cdot d\underline{V} \\ &= d\underline{U} \cdot (\underline{\underline{C}} - \underline{\underline{I}}) \cdot d\underline{V} \\ &= d\underline{U} \cdot 2\underline{\underline{E}} \cdot d\underline{V} \end{aligned} \tag{3.8}$$

where the tensor $\underline{\underline{E}} = 1/2(\underline{\underline{C}} - \underline{\underline{I}})$ is the Green-Lagrange strain tensor : in small deformation, this tensor is the same with the linear deformation tensor $\underline{\underline{\varepsilon}}$. The two tensors mentioned above are defined on the initial configuration, so they are lagrangian quantities. We can also define the same quantities on the deformed configuration :

$$\begin{aligned} \underline{\underline{b}} &= \underline{\underline{F}} \cdot \underline{\underline{F}}^T = \underline{\underline{V}}^2 \\ \underline{\underline{a}} &= \frac{1}{2} \left(\underline{\underline{I}} - \underline{\underline{b}}^{-1} \right) \end{aligned} \tag{3.9}$$

these two quantities are the left Cauchy-Green tensor and Euler-Almansi tensor.

It should be emphasized that Green strain and Almansi strain are two ways of viewing the same deformation process, so they can transform into each other by push-forward or pull-back operations :

$$\underline{\underline{E}} = \underline{\underline{F}}^T \cdot \underline{\underline{a}} \cdot \underline{\underline{F}} \tag{3.10}$$

$$\underline{\underline{a}} = \underline{\underline{F}}^{-T} \cdot \underline{\underline{E}} \cdot \underline{\underline{F}}^{-1} \tag{3.11}$$

In order to define different kinds of deformation laws, it is necessary to define the quantities to describe the deformation velocity. According to EQ. 3.2, we have :

$$d\underline{\dot{x}} = \underline{\underline{\dot{F}}} \cdot d\underline{X} = \underline{\underline{\dot{F}}} \cdot \underline{\underline{F}}^{-1} \cdot d\underline{x} = \underline{\underline{l}} \cdot d\underline{x} \tag{3.12}$$

where $\underline{\underline{l}}$ is the velocity gradient. It can be decomposed into a symmetry part $\underline{\underline{d}}$ (deformation rate)and an anti-symmetric part $\underline{\underline{w}}$ (rotation rate) :

$$\begin{aligned} \underline{\underline{l}} &= \underline{\underline{d}} + \underline{\underline{w}} \\ \underline{\underline{d}} &= \frac{1}{2}(\underline{\underline{F}} + \underline{\underline{F}}^T) \\ \underline{\underline{w}} &= \frac{1}{2}(\underline{\underline{F}} - \underline{\underline{F}}^T) \end{aligned} \tag{3.13}$$

The tensor of deformation rate is a measurement on the deformed configuration. We can also get the corresponding measurement in the initial configuration :

$$\underline{\underline{\dot{E}}} = \frac{1}{2}\underline{\underline{\dot{C}}} = \underline{\underline{F}}^T \cdot \underline{\underline{d}} \cdot \underline{\underline{F}} \tag{3.14}$$

Stress measurement

There are several different stress tensors, and the most fundamental one is Cauchy stress. Considering an infinitesimal area element ds in the deformed body, its normal direction is $\underline{n}_s$ and the force on this small area is $\underline{t}$ (it is also named stress vector). The well-known Cauchy law proves that there always exists a tensor that could map $\underline{n}$ to $\underline{t}$:

$$\underline{t} = \underline{\underline{\sigma}} \cdot \underline{n} \tag{3.15}$$

$\underline{\underline{\sigma}}$ is Cauchy stress, which is also known as true stress. It is work-conjugated with the rate of deformation $\underline{\underline{D}}$:

$$P = \int_V \underline{\underline{\sigma}} : \underline{\underline{D}} dV \tag{3.16}$$

Rewriting the work rate over the initial configuration volume, the Kirchhoff stress $\underline{\underline{\tau}}$ arises :

$$\int_V \underline{\underline{\sigma}} : \underline{\underline{D}} dV = \int_{V^0} J \underline{\underline{\sigma}} : \underline{\underline{D}} dV^0 = \int_{V^0} \underline{\underline{\tau}} : \underline{\underline{D}} dV^0 \tag{3.17}$$

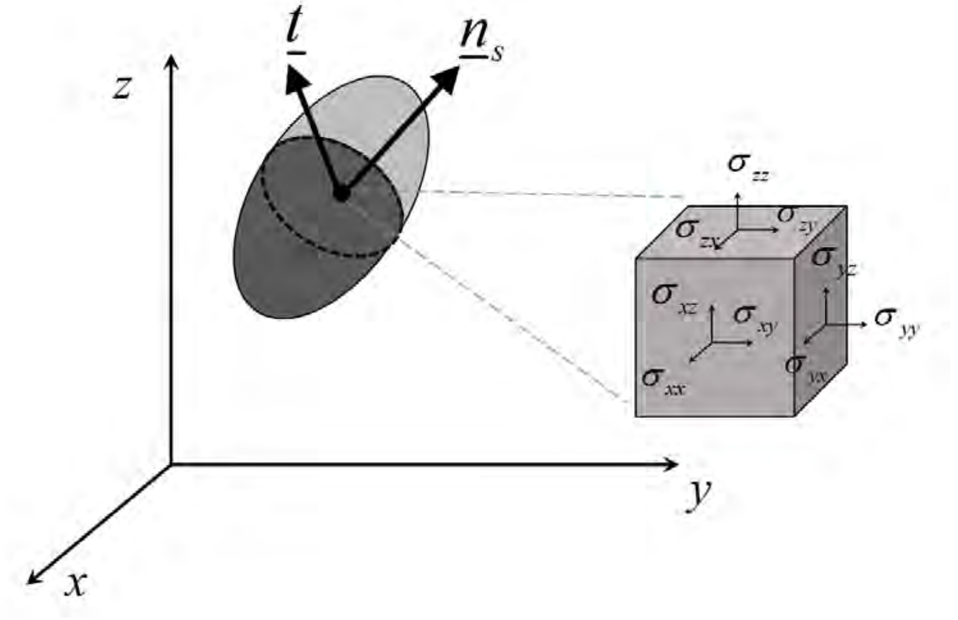

FIGURE 3.1 – Definition of Cauchy stress.

Kirchhoff stress finds its application in the large strain deformation. From EQ. (3.16) we know that $\underline{\underline{\sigma}}$ and $\underline{\underline{D}}$ are work conjugation couples, for the same reason, it is useful to find out the stress tensor conjugated with Green strain rate $\underline{\underline{\dot{\varepsilon}}}^G$:

$$\int_V \underline{\underline{\sigma}} : \underline{\underline{D}} dV = \int_{V^0} \left(J \underline{\underline{F}}^{-1} \cdot \underline{\underline{\sigma}} \cdot \underline{\underline{F}}^{-T} \right) : \underline{\underline{\dot{\varepsilon}}}^G dV^0 = \int_{V^0} \underline{\underline{\tau}} : \underline{\underline{\dot{\varepsilon}}}^G dV^0 \tag{3.18}$$

3.1.2 Definition of hypo-elasticity

The hypo-elastic law relates the rate of stress to the rate of deformation $\underline{\underline{D}}$ linearly :

$$\underline{\underline{\sigma}}^{\nabla} = \underline{\underline{\underline{\underline{C}}}} : \underline{\underline{D}} \tag{3.19}$$

where $\underline{\underline{\underline{\underline{C}}}}$ is a fourth-order tensor of elastic moduli, which may itself depends on the stress. $\underline{\underline{\sigma}}^{\nabla}$ represents any objective time derivative of the Cauchy stress $\underline{\underline{\sigma}}$ to avoid the stress change due to the rigid body rotation in $\underline{\underline{\dot{\sigma}}}$, so $\underline{\underline{\sigma}}^{\nabla}$ can be comprehended as the derivative from an observer who is fixed on the material. If we define $\underline{\underline{Q}}$ as the rotation of the observer, define $\underline{\underline{\Omega}} = \underline{\underline{\dot{Q}}} \cdot \underline{\underline{Q}}^T$ as the rotation rate, and expand $\underline{\underline{\sigma}}$ on the material base $\{\underline{e}_1;\underline{e}_2;\underline{e}_3\}$:

$$\underline{\underline{\sigma}} = \sigma_{ij} \underline{e}_i \otimes \underline{e}_j \tag{3.20}$$

The following derivation shows how the $\underline{\underline{\sigma}}^{\nabla}$ eliminates the effects of rigid rotation from $\dot{\underline{\underline{\sigma}}}$:

$$\begin{aligned}\dot{\underline{\underline{\sigma}}} &= \dot{\sigma}_{ij}\underline{e}_i \otimes \underline{e}_j + \sigma_{ij}\dot{\underline{e}}_i \otimes \underline{e}_j + \sigma_{ij}\underline{e}_i \otimes \dot{\underline{e}}_j \\ &= \dot{\sigma}_{ij}\underline{e}_i \otimes \underline{e}_j + \sigma_{ij}\left(\Omega \cdot \underline{e}_i\right) \otimes \underline{e}_j + \sigma_{ij}\underline{e}_i \otimes \left(\Omega \cdot \underline{e}_j\right) \\ &= \underline{\underline{\sigma}}^{\nabla} + \underline{\underline{\Omega}} \cdot \underline{\underline{\sigma}} - \underline{\underline{\sigma}} \cdot \underline{\underline{\Omega}}\end{aligned} \tag{3.21}$$

So the objective derivative of Cauchy stress is :

$$\underline{\underline{\sigma}}^{\nabla} = \dot{\underline{\underline{\sigma}}} - \underline{\underline{\Omega}} \cdot \underline{\underline{\sigma}} + \underline{\underline{\sigma}} \cdot \underline{\underline{\Omega}} \tag{3.22}$$

EQ. (3.22) gives the definition expression of objective derivative, while in the finite process, it is updated according to this equation :

$$\underline{\underline{\sigma}}^{\nabla} = \underline{\underline{Q}} \cdot \left(\frac{d}{dt}\left(\underline{\underline{Q}}^T \cdot \underline{\underline{\sigma}} \cdot \underline{\underline{Q}}\right)\right) \cdot \underline{\underline{Q}}^T \tag{3.23}$$

It should be highlighted that defining a proper rotation $\underline{\underline{Q}}$ is a challenge. In fact for a given material point, it is impossible to find a $\underline{\underline{Q}}$ to precisely reflect the rigid rotation of all materiel directions. This is because the rotation value varies according to the directions (except the circumstance of pure rigid movement). *E.g.* the discussion in section 3.1 tells us that the rotation $\underline{\underline{R}}$ from polar decomposition is only precise for the principle directions, while for the other directions it is just a kind of rough expression. If $\underline{\underline{R}}$ is chosen to identify $\underline{\underline{\sigma}}^{\nabla}$, we get Green-Naghdi objective derivative (see table 3.1). Table 3.1 also shows some other expression of objective derivative for both Cauchy stress and Kirchhhof stress as well as the corresponding rate law.

	Rate law	Stress rate
Jaumann rate of Cauchy stress	$\underline{\underline{\sigma}}^{\nabla J} = \underline{\underline{\underline{\underline{C}}}}^{\sigma J} : \underline{\underline{D}}$	$\underline{\underline{\sigma}}^{\nabla J} = \dot{\underline{\underline{\sigma}}} - \underline{\underline{W}} \cdot \underline{\underline{\sigma}} - \underline{\underline{\sigma}} \cdot \underline{\underline{W}}^t$
Jaumann rate of Kirchhoff stress	$\underline{\underline{\tau}}^{\nabla J} = \underline{\underline{\underline{\underline{C}}}}^{\tau J} : \underline{\underline{D}}$	$\underline{\underline{\tau}}^{\nabla J} = \dot{\underline{\underline{\tau}}} - \underline{\underline{W}} \cdot \underline{\underline{\tau}} - \underline{\underline{\tau}} \cdot \underline{\underline{W}}^t$
Green-Naghdi rate of Cauchy stress	$\underline{\underline{\sigma}}^{\nabla G} = \underline{\underline{\underline{\underline{C}}}}^{\sigma G} : \underline{\underline{D}}$	$\underline{\underline{\sigma}}^{\nabla G} = \dot{\underline{\underline{\sigma}}} - \underline{\underline{\Omega}} \cdot \underline{\underline{\sigma}} - \underline{\underline{\sigma}} \cdot \underline{\underline{\Omega}}^t \; \underline{\underline{\Omega}} = \dot{\underline{\underline{R}}} \cdot \underline{\underline{R}}^t$
Truesdell rate of Cauchy stress	$\underline{\underline{\sigma}}^{\nabla \tau} = \underline{\underline{\underline{\underline{C}}}}^{\sigma \tau} : \underline{\underline{D}}$	$\underline{\underline{\sigma}}^{\nabla \tau} = \dot{\underline{\underline{\sigma}}} + div\left(\underline{v}\right)\underline{\underline{\sigma}} - \left(\underline{\underline{D}} + \underline{\underline{W}}\right) \cdot \underline{\underline{\sigma}} - \underline{\underline{\sigma}} \cdot \left(\underline{\underline{D}} + \underline{\underline{W}}\right)^t$

TABLE 3.1 – Common objective derivatives and rate laws

3.1.3 Objective derivative frame for fibrous material

As have been discussed in section 3.1, the rigid rotation tensor $\underline{\underline{Q}}$ is an average rotation expression. This is not a big deal for those materials in which the material orientation is not obvious (concrete, metal, rubber, *etc.*). Nevertheless the property of composite reinforcement badly depends on the yarns' orientation, which implies the importance of monitoring yarns' orientation.

Hagege [HAG 04, BOI 05b] and Badel [BAD 07, BAD 08c, BAD 09] have noticed that the hypo-elastic constitutive law based on traditional rotations (Green-Naghdi,Jaumann,*etc.*) cannot correctly describe finite strains of a fibrous medium. So a new objective derivative frame $\underline{\underline{\Phi}}$ was developed based on the direction of yarn :

$$\underline{\underline{\sigma}}^{\nabla\Phi} = \underline{\underline{\underline{\underline{C}}}}^{\Phi} : \underline{\underline{D}} \tag{3.24}$$

in which $\underline{\underline{\sigma}}^{\nabla\Phi}$ is defined as follows :

$$\underline{\underline{\sigma}}^{\nabla\Phi} = \underline{\underline{\dot{\sigma}}} - \underline{\underline{\Omega}}_{\Phi} \cdot \underline{\underline{\sigma}} + \underline{\underline{\sigma}} \cdot \underline{\underline{\Omega}}_{\Phi} \tag{3.25}$$

where $\underline{\underline{\Omega}}_{\Phi} = \underline{\underline{\dot{\Phi}}} \cdot \underline{\underline{\Phi}}^T$ is the spin tensor.

$\mathbf{f}^0 = \left\{ \underline{f}_1^0, \underline{f}_2^0, \underline{f}_3^0 \right\}$ is the orthogonal base on the undeformed yarn, and $\underline{f}_1^0$ respects the orientation of the yarn. The rotation tensor $\underline{\underline{\Phi}}$ is calculated as follows (FIG. 3.2) :

Step 1. Updating the direction of yarn $\underline{f}_1$ from the initial $\underline{f}_1^0$. The updating is realized based on deformation gradient $\underline{\underline{F}}$:

$$\underline{f}_1 = \frac{\underline{\underline{F}} \cdot \underline{f}_1^0}{||\underline{\underline{F}} \cdot \underline{f}_1^0||} \tag{3.26}$$

Step 2. Projecting the 2^{nd} direction $\underline{\underline{F}} \cdot \underline{f}_2^0$ on the plane perpendicular to $\underline{f}_1$:

$$\underline{f}_2 = \frac{\underline{\underline{F}} \cdot \underline{f}_2^0 - \left(\left(\underline{\underline{F}} \cdot \underline{f}_2^0 \right) \cdot \underline{f}_1 \right) \cdot \underline{f}_1}{||\underline{\underline{F}} \cdot \underline{f}_2^0 - \left(\left(\underline{\underline{F}} \cdot \underline{f}_2^0 \right) \cdot \underline{f}_1 \right) \cdot \underline{f}_1||} \tag{3.27}$$

Step 3. Updating the 3^{rd} direction $\underline{f}_3$ according to $\underline{f}_1$ and $\underline{f}_2$:

$$\underline{f}_3 = \underline{f}_1 \bigwedge \underline{f}_2 \tag{3.28}$$

The rotation tensor could be written as the following form :

$$\underline{\underline{\Phi}} = \underline{f}_i \otimes \underline{f}_i^0 \tag{3.29}$$

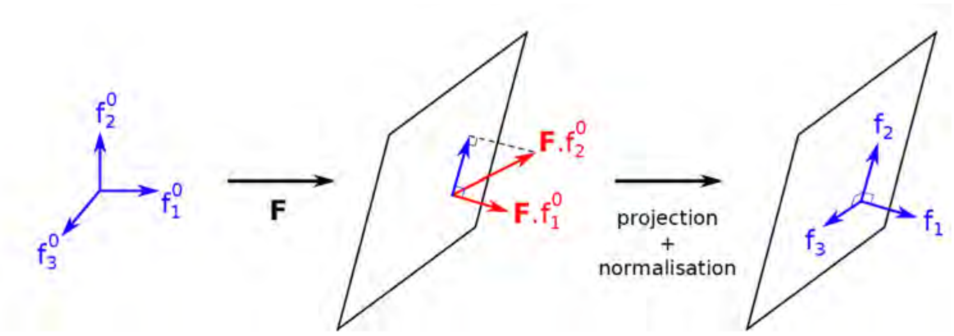

FIGURE 3.2 – Definition of the rotation to follow the direction of yarn [BAD 08b]

EQ. (3.24) is integrated with Hughes-Winget formula [HUG 80] over $\Delta t = t^{n+1} - t^n$:

$$[\sigma^{n+1}]_{f^{n+1}} = [\sigma^n]_{f^n} + [C^{n+\frac{1}{2}}]_{f^{n+\frac{1}{2}}} [\Delta\varepsilon^{n+1}]_{f^{n+\frac{1}{2}}} \tag{3.30}$$

The stress updating in EQ. (3.30) should be recognized in the commercial F.E. codes. For instance in ABAQUS/Explicit the user-defined material model is implemented in user subroutine VUMAT, and the strain increment is expressed on the work frame of Green-Naghdi in which the rotation is $\underline{\underline{R}}$:

$$\underline{e}_i = \underline{\underline{R}} \cdot \underline{e}_i^0 \tag{3.31}$$

where $\underline{e}_i^0$ is the vector base in the undeformed configuration (so $\underline{e}_i^0 = \underline{f}_i^0$). If we use $\underline{\underline{\Theta}}$ to denote the rotation between $\underline{f}_i$ and $\underline{e}_i$:

$$\underline{\underline{\Theta}} = \underline{f}_i \otimes \underline{e}_i \tag{3.32}$$

the corresponding matrix form of $\underline{\underline{\Theta}}$ used in F.E. loop is [T], that is to say :

$$[\sigma]_{e_i} = [T][\sigma]_{f_i} \tag{3.33}$$

so the strain increment on the Green-Naghdi base $\underline{e}_i$ is transformed into the base of $\underline{f}_i$ to update the stress, after which $[\Delta\sigma]$ is rotated back to the Green-Naghdi to continue the F.E. loop. The stress updating process based on the fiber frame $\underline{\underline{\Theta}}$ is displayed in the flow diagram in FIG. 3.3.

3.2 A mesoscopic model proposed in previous works

In order to obtain the expression of $[C]^{\Phi}$, the deformation of the yarn should be well studied. The deformation of the fibrous structure can be regarded as the combination of different deformation modes. In previous studies [BAD 07, BAD 08b, BAD 08c, BAD 09], four modes play the dominant roles : the elongation, the longitudinal shear, the transverse compaction and the transverse shear (FIG. 3.4).

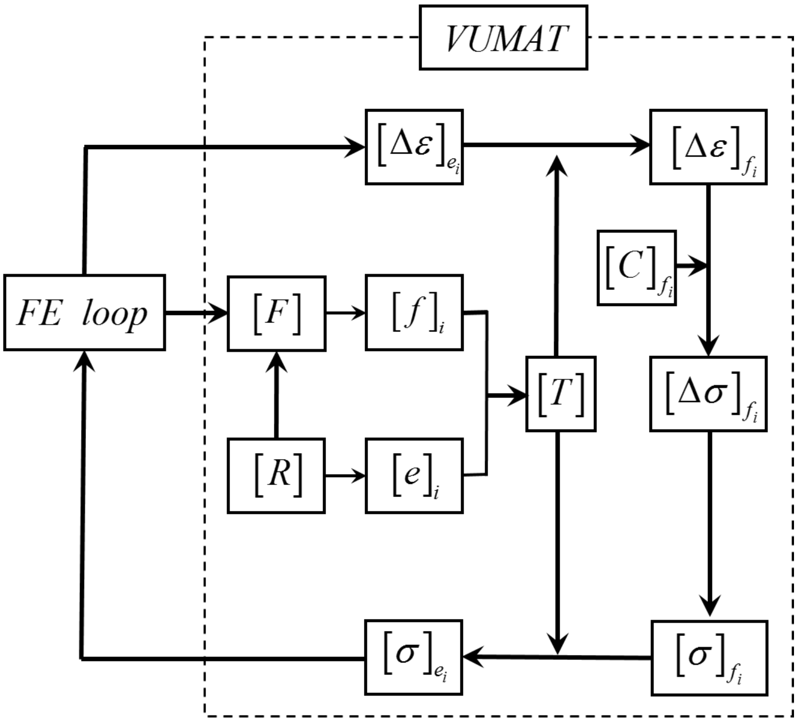

FIGURE 3.3 – Flow diagram of VUMAT to update stress for fibrous material [KHA 09, KHA 10]

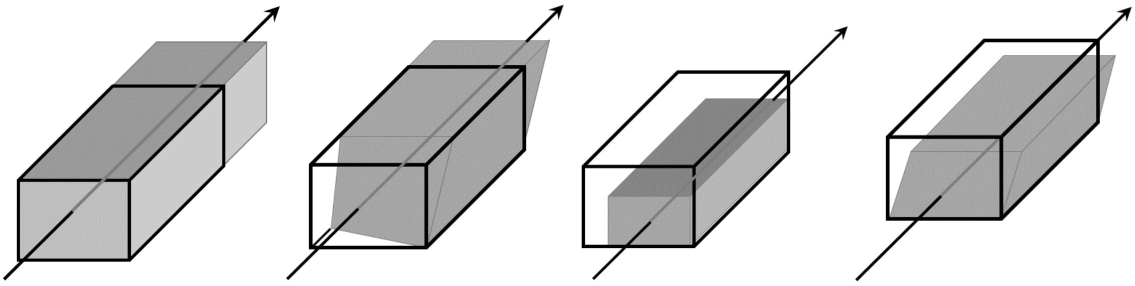

(a) Elongation **(b)** Longitunidal shear **(c)** Compaction of the cross section **(d)** Distortion of the cross section

FIGURE 3.4 – Mesoscale deformation modes considered in the previous works [CHA 11]

3.2.1 Elongation deformation

Elongation stiffness of the yarn K_l is the most important parameter for composite, because it provides the main resistance of the structure. The tension experiments on tapas fabric have been introduced in chapter 1 and the stiffness information of the three kind of yarns in tapas fabric (warp yarn, weft yarn and binder yarn) have been exhibited in FIG. 1.9a. All the stiffness curves start by a nonlinear part, which can be explained by the rearrangement of the fibers. So the tensile stiffness K_l is nonlinear (the minuscule l is always used to express *longitudinal* when it is written as subscript). Nonetheless, for the purpose of brevity, the nonlinear part of K_l can usually be ignored.

In this case, K_l should be converted into Young Modulus in F.E. loops :

$$E_l = \frac{K_l}{S} \tag{3.34}$$

where E_l is the longitudinal Young's modulus and S is the area of the cross section. E_l is not constant since S varies in the deformation. FIG. 3.5 shows how S is tracked :

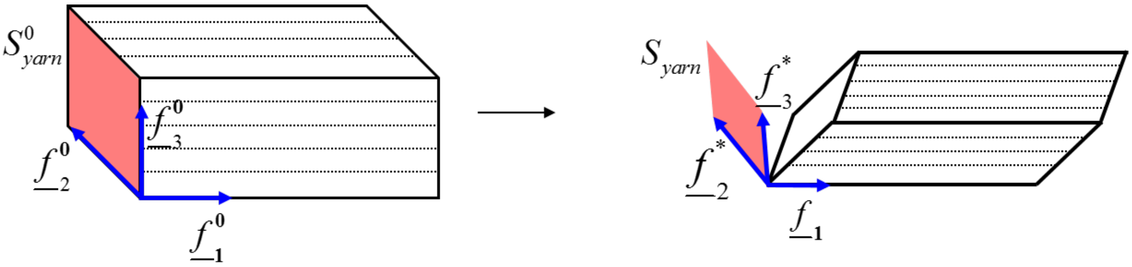

FIGURE 3.5 – Mornitoring the change of secion area of the yarn

Step 1. The surface element of the cross section in the undeformed yarn can be stated by $\underline{f}^0_2$ and $\underline{f}^0_3$:

$$dS_0 = \|\underline{f}^0_2 \times \underline{f}^0_3\| = 1 \tag{3.35}$$

Step 2. Projecting the deformed $\underline{f}^0_2$ and $\underline{f}^0_3$ on the new cross section that is normal to $\underline{f}_1$:

$$\underline{f}^*_2 = \underline{\underline{F}} \cdot \underline{f}^0_2 - \left(\left(\underline{\underline{F}} \cdot \underline{f}^0_2\right) \cdot \underline{f}_1\right) \cdot \underline{f}_1 \tag{3.36}$$

$$\underline{f}^*_3 = \underline{\underline{F}} \cdot \underline{f}^0_3 - \left(\left(\underline{\underline{F}} \cdot \underline{f}^0_3\right) \cdot \underline{f}_1\right) \cdot \underline{f}_1 \tag{3.37}$$

note that $\underline{f}^*_2$ and $\underline{f}^*_3$ are different with $\underline{f}_2$ and $\underline{f}_3$.

The new surface element of the cross section in the deformed yarn can be stated by $\underline{f}^*_2$ and $\underline{f}^*_3$:

$$dS = \|\underline{f}^*_2 \times \underline{f}^*_3\| \tag{3.38}$$

Step 3. The initial area S_0 can be measure from tomography experiment, and the results for tapas fabric are shown in table 3.2.

Step 4. The longitudinal Young's modulus is updated according to :

$$E_l = \frac{K_l}{S_0} \cdot \frac{dS_0}{dS} = \frac{E^0_l}{\|\underline{f}^*_2 \times \underline{f}^*_3\|} \tag{3.39}$$

	$K_l(N)$	S_0 (mm^2)	$Initial\ E_l(MPa)$
Warp yarn	19000	0.5735	~ 33130
Weft yarn	2740	0.0868	~ 31567
Binder yarn	2340	0.0798	~ 29323

TABLE 3.2 – Longitudinal tensile properties of yarns in tapas fabric

3.2.2 Longitudinal shear deformation

Longitudinal shear is the shear in the longitudinal section of the yarn, so its stiffness can be noted by G_{lt}(*l* means *longitudinal* and t is *transverse*). G_{lt} is small since the fibers in the yarn are slippery and tend to have relative sliding. This is proved by the fact that the fabric and the yarns have almost no resistance to bending (see section 1.3.4). But attention is still required, since improper shear stiffness in a simulation could lead to numerical failures such as hourglass problem. It is found that for the tapas fabric fabric, G_{lt} around 20 MPa is a suitable choice to keep the yarn's physical nature and keep the simulation away from the hourglass problem.

3.2.3 Two kinds of transverse deformations

Transverse compaction and transverse shear deformation modes in FIG. 3.4 exist in the cross-section of the yarn. The corresponding stiffness are E_t and G_t. When the yarn deforms, the shape and area of the cross section change simultaneously. This leads to a decomposition of the strain tensor : the strain field in the cross section of the yarn can be decomposed into a spherical part and a deviatoric part that characterize the area change and shape change respectively [BAD 07, BAD 08b] :

$$[\varepsilon_t]_f = \begin{bmatrix} \varepsilon_s & 0 \\ 0 & \varepsilon_s \end{bmatrix} + \begin{bmatrix} \varepsilon_d & \varepsilon_{23} \\ \varepsilon_{23} & -\varepsilon_d \end{bmatrix} \tag{3.40}$$

where $[\varepsilon_t]_f$ is the strain field of the transverse section, expressed on the fiber base ; ε_s is the spherical strain component ; ε_d and ε_{23} are the deviatoric strain components. So ε_s and ε_d have the following relationships with ε_{22} and ε_{33} :

$$\varepsilon_s = \frac{\varepsilon_{22} + \varepsilon_{33}}{2} \tag{3.41}$$

$$\varepsilon_d = \frac{\varepsilon_{22} - \varepsilon_{33}}{2} \tag{3.42}$$

The decomposition in EQ. (3.40) is also considered valid for strain and stress increments $[\Delta\varepsilon_t]_f$ and $[\Delta\sigma_t]_f$, which leads to the following constitutive relations :

$$\begin{aligned}\Delta\sigma_s &= A\Delta\varepsilon_s\\ \Delta\sigma_d &= B\Delta\varepsilon_d\\ \Delta\sigma_{23} &= C\Delta\varepsilon_{23}\end{aligned} \tag{3.43}$$

where A, B and C are stiffness parameters. In section 2.3, the transverse isotropy of the yarn has been proved. Based on this isotropy assumption, it is derived that B=C.

As is displayed in 3.43, the parameter of A provides the resistance to the variation of sectional area, which is affected by two kind of deformations : the elongation that stretches the fibers into a tighter state, and the transverse compression that improves the compactness of the cross section. Both of them make it more difficult to change the sectional area. So A becomes larger when the elongation state (ε_l) becomes larger, and becomes smaller when the spherical part of the transverse strain field (ε_s) is smaller :

$$A = A_0 e^{-p\varepsilon_s} e^{n\varepsilon_l} \tag{3.44}$$

where A_0 is the initial value of A ; the influence factors of ε_s and ε_l are p and n.

Another parameter B provides the resistance to the shape change of the cross section, which is affected by the compactness of the yarn :

$$B = B_0 e^{-p\varepsilon_s} \tag{3.45}$$

where B_0 is the initial value of B.

Finally, the constitutive matrix $[C]^\Phi$ is expressed as :

$$[C]^\Phi = \begin{bmatrix} E & 0 & 0 & 0 & 0 & 0\\ & \frac{A+B}{2} & \frac{A-B}{2} & 0 & 0 & 0\\ & & \frac{A+B}{2} & 0 & 0 & 0\\ & & & G_{lt} & 0 & 0\\ & syms & & & B & 0\\ & & & & & G_{lt}\end{bmatrix} \tag{3.46}$$

All the unknown parameters (A_0,B_0,p *and* n) will be obtained by the Levenberg-Marquardt (L-M) inverse fitting algorithm [LEV 44, MAR 63, SCH 92], which is a standard technique used to solve nonlinear least square problem. L-M is a combination of two minimization algorithms : the Gauss-Newton algorithm and the gradient descent method. It is more like the Gauss-Newton when the parameters are close to their optimal value, and acts more like gradient-descent method when the parameters are far from the optimal values [GAV 13]. Based on L-M, A_0, B_0 and p can be obtained by the compaction experiment, the fitting curves are shown in FIG. 3.6a.

Noting that n is a coupling parameter of the longitudinal deformation and transverse deformation, the biaxial tension experiment is the appropriate choice to evaluate the value of n. This is because tension and transverse compaction exist in the biaxial tension test simultaneously. The fitting curves are shown in FIG. 3.6b. For the tapas fabric in this study, the values for A_0, B_0 , p and n are shown in table 3.3.

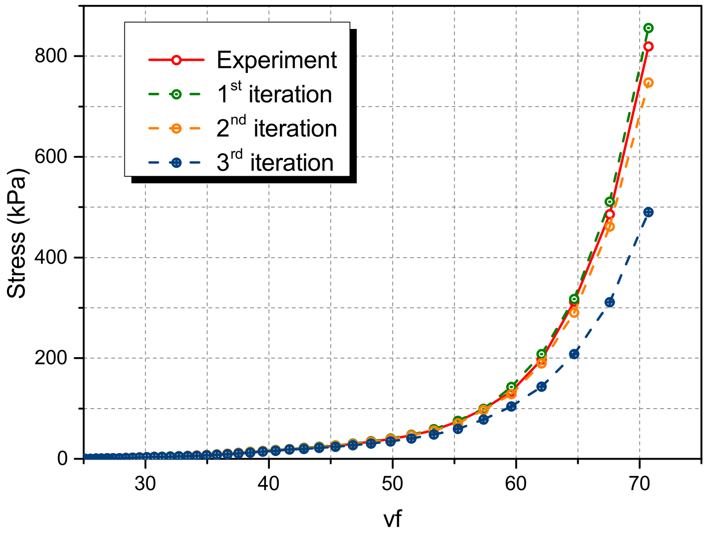

(a) Inverse fitting for A_0, B_0 and p based on compaction experiment

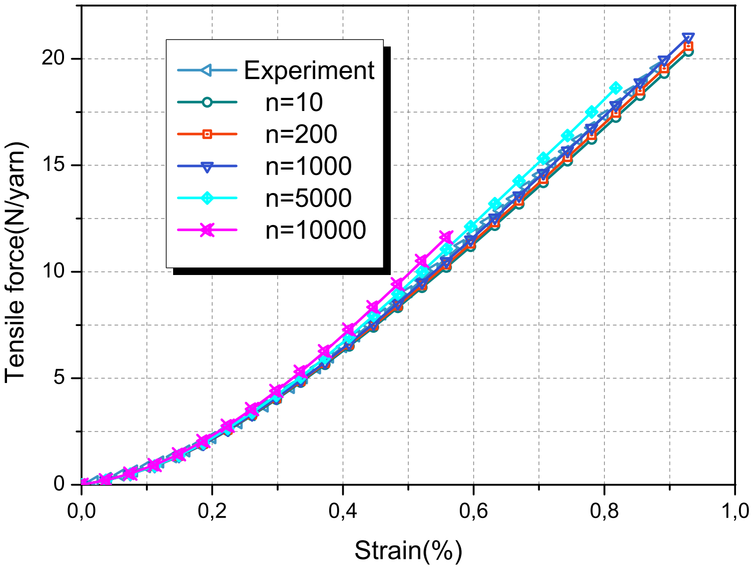

(b) The fitting process for n based on the biaxial tension test (weft direction, k=1)

FIGURE 3.6 – Measurement of parameters in the mesoscopic model

3.2.4 Applications and defects

In order to show the effectiveness and defects of the mesoscopic model proposed in the previous works, several simulations will be displayed. Some of these simulations are quite successful : the deformed structure is quite similar with the tomography results. Nevertheless for some others, there exist non-ignorable defects. These defects will be

Parameter	$A_0(MPa)$	$B_0(MPa)$	n	p
Value	0.16	0.14	1000	26.7

TABLE 3.3 – The optimised parameters concerning the transverse deformation of the mesoscopic model

well exhibited here while the reasons and solutions will be revealed in section 3.3 and section 3.4.

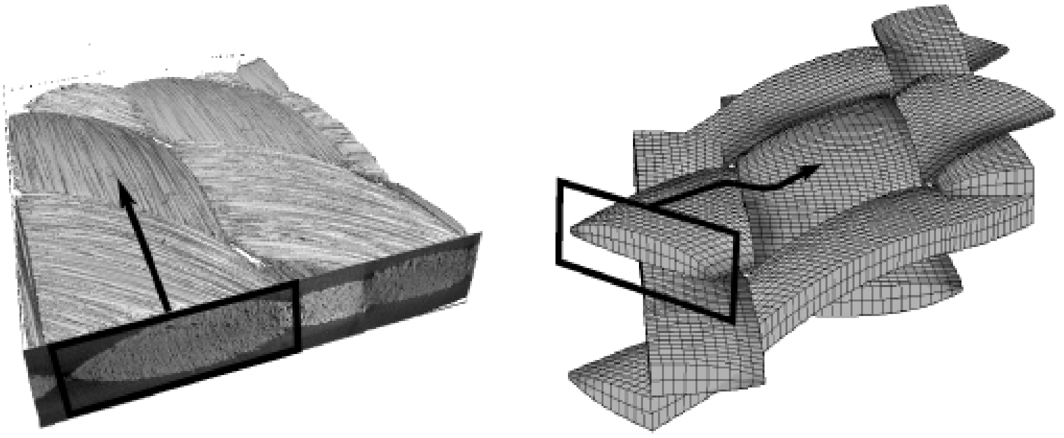

(a) Tomgraphy of sheared plain fabric **(b)** Simulation of the pure shear of plain fabric

FIGURE 3.7 – Comparison of shear simulaion and tomography [BAD 08b]

The first example is a shear simulation from the work of Badel [BAD 08b] (FIG. 3.7). The simulation is on the plain composite and the largest shear angle is 46^o. The geometrical model is the first kind of RUC in FIG. 1.33, so its initial geometric boundaries are material boundaries thus permit to directly impose the periodicity conditions. The cross sections of the deformed model are verified by tomography technology. From a qualitative points of view, it is found that the model could capture the main geometry features observed in tomography, including section asymmetry, significant decrease of the width, flat sides, rounded sides and overall decrease of the area. Moreover, the ratio of the area between initial and deformed states are 0.77 for the measure by tomography versus 0.71 for the simulation, and those for the width are 0.77 and 0.74 respectively. There are two error sources in this simulaion : the first one is the identification of constitutive parameters and the second one is the model itself. The conclusion is that although there exists minor different, the numerical simulation is able to reflect the main geometric trends observed in tomography [BAD 08b].

The second example is a compaction simulation on carbon twill fabric stacks [NGU 12] (FIG. 3.8), in which two kinds of fabric stacks are studied. There is no nesting between adjacent fabric layers in the first kind of fabric stack, while the nesting phenomenon of the second kind of the stack is very large. He found that the compaction

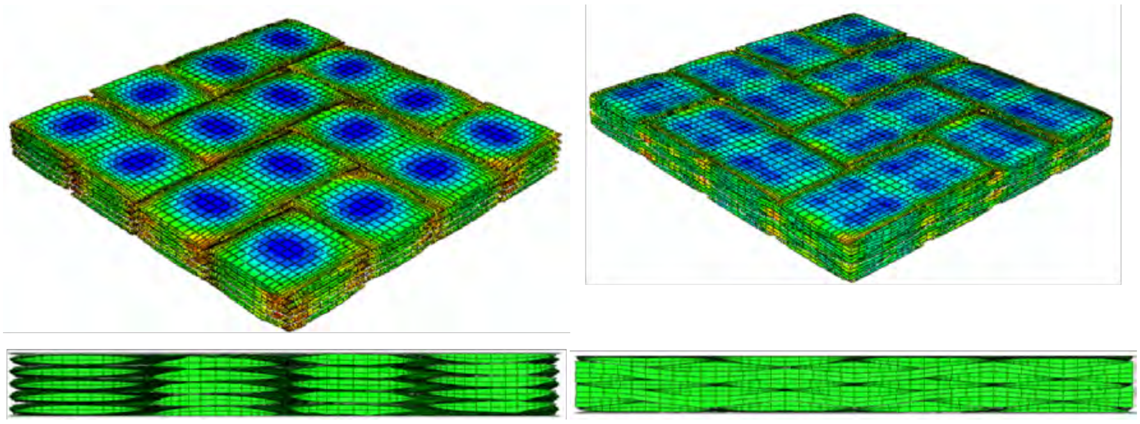

(a) The compaction simulation on carbon twill fabric stacks without nesting **(b)** The compaction simulation on carbon twill fabric stacks with large nesting

FIGURE 3.8 – The compaction simulations on carbon twill fabric stacks [NGU 12]

stiffness of the second stack is smaller because of the nesting phenomenon, and this conclusion is verified by experiment[NGU 12, NGU 13].

However the model proposed in the previous works is not always perfect. It is noticed that, among all the deformation modes considered in this model, the longitudinal compression performance of the yarn has not been determined, and equating it to the tension performance is probably not correct. The two above mentioned examples from previous works are successful because the longitudinal compression deformations in the deformations of these examples are quite small. However, when longitudinal compression becomes non-ignorable, some flaws arise. *E.g.*, the RUC of tapas fabric is compressed transversely by two rigid plates, and the compaction ratio is 55.4%, which is the same with the tomography experiment is FIG. 3.9a. Comparing the yarns observed in the tomography experiment and the compaction simulations, two kinds of defects could be found :

Spurious wrinkle. As can be observed, some spurious wrinkles exist in the binder yarn (FIG. 3.9). These wrinkles are numerical ones since they cannot be found in tomography radiography (FIG. 3.9a). The reason of this numerical problem is that the small longitudinal compression stiffness of the yarn is assumed to be equal to the tensile one. In other words, the large tension stiffness and small compression stiffness is not distinguished in the previously proposed mesoscopic model. More details and solutions can be found in section 3.3.

Insufficient transverse expansion. The comparisons between tomography and simulation (FIG. 3.9) reflects another shortcoming of the previously proposed mesomodel. As are marked by the arrows, the transverse expansion observed in the tomography radiography is much larger than the one in the simulations. This is because the transverse expansion phenomenon when the yarn is compressed longitudinally is ignored. This phenomenon will be considered in a new deformation mode named transverse expansion mode in section 3.4.

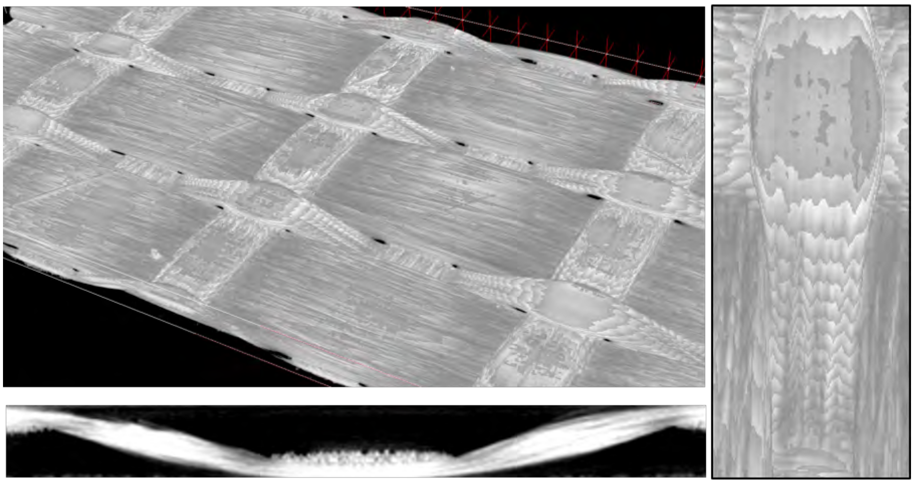

(a) Tomography of compacted tapas fabric

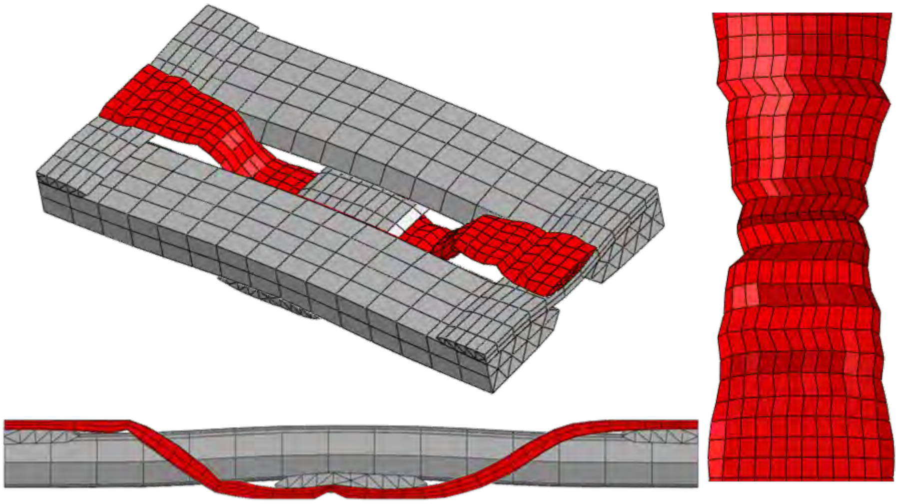

(b) Simulation of tapas fabric compaction

FIGURE 3.9 – simulation of compaction on tapas fabric with the mesoscale mechanical model proposed in the previous works (compaction ratio is 55.4%)

3.3 Longitudinal compression mode

To settle the spurious wrinkles found in FIG. 3.9, a new deformation mode called longitudinal compression (LC) will be developed in this section. The purpose of longitudinal compression is taking into account the weak longitudinal compression stiffness. It will be shown that it is possible to measure the value of longitudinal compression stiffness, nonetheless the main difficulty is the incompatibility problem between the small longitudinal compression stiffness K_l^{comp} and the large tensile stiffness K_l^{tens}.

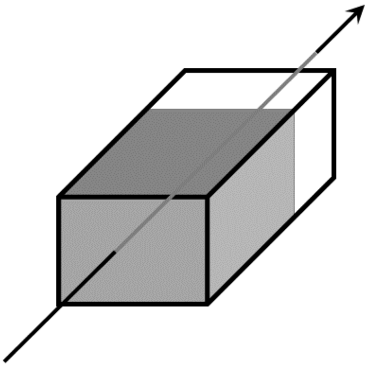

FIGURE 3.10 – Longitudinal compression mode

3.3.1 The necessity of longitudinal compression mode

When the constitutive matrix $[C]^{\Phi}$ is derived in section 3.2, the longitudinal compression is assumed to be equal to the tensile one. As a result, the longitudinal stiffness of the yarn is a constant (FIG. 3.11). This is not compatible with the physical characteristic of the yarn, since its longitudinal compression stiffness should be quite small. This is exactly the source of the spurious wrinkles.

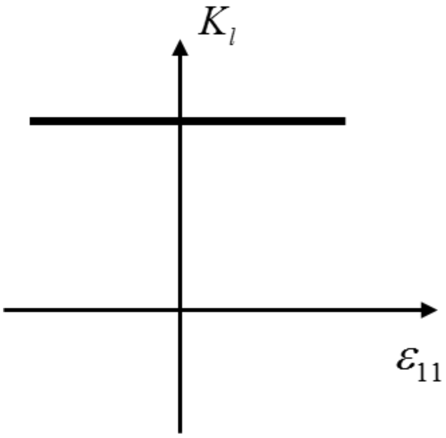

FIGURE 3.11 – K_l is constant in the model proposed in the previous works

FIG. 3.12 shows how the ignorance of longitudinal compaction stiffness leads to the spurious wrinkles. The 2-element structure is compressed by horizontal forces or displacements, and since the longitudinal compression stiffness is as large as the tension stiffness (around 20000 N/yarn for warp yarn, and 3000 N/yarn for weft and binder yarns in tapas fabric, see table 3.2), and the shear stiffness is very small (about 20 N/yarn in the model of tapas fabric), the deformation in FIG. 3.12 will happen.

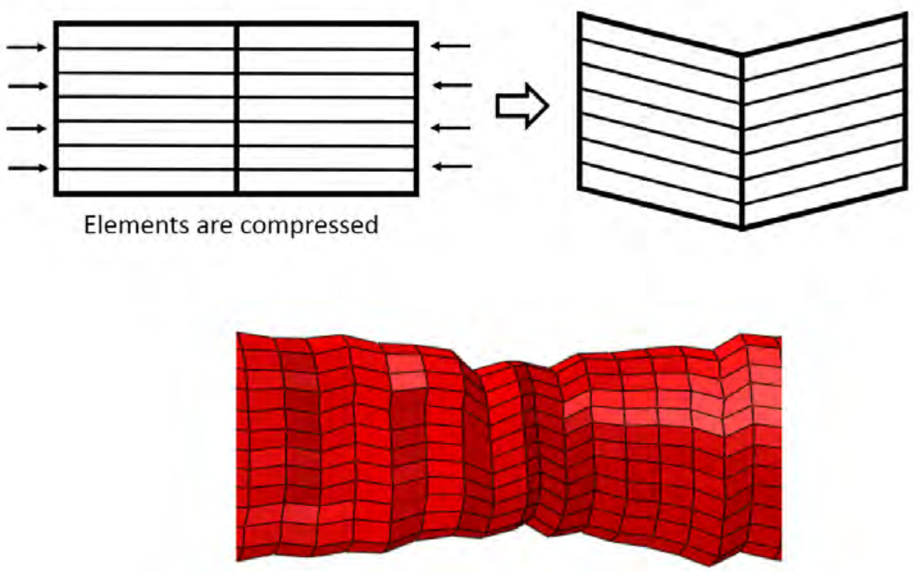

FIGURE 3.12 – The explanation for the source of spurious wrinkles

In a conclusion, the source of spurious wrinkle is that, when the yarn is compressed longitudinally, $E_l >> G_l$ in the simulation, which is quite physical unreasonable. It is necessary to take into account the weak Young's modulus of longitudinal compression.

3.3.2 Construction of longitudinal compression mode

Measurement of longitudinal compression stiffness

Longitudinal compression stiffness $K_l^c omp$ for different yarns are measured by longitudinal compression experiments. The experimental setups are shown in FIG. 3.13). It is noted that the yarns without resin are so soft that they have almost no resistance to longitudinal compression. For this consideration, high accuracy force sensor is required (the one in this study is a sensor of 10 N), and it is advised to compress several yarns at the same time (e.g., Fig. 3.13 shows a experiment sample of 10 binder yarns). The compression velocity is 2 mm/min, which is slow enough to eliminate the dynamic influence. As an example, the longitudinal compression stiffness curves of the binder yarn in the aforementioned 2D fabric are exhibited in Fig. 3.14. It is found that the shorter yarn has larger resistance to longitudinal compression. Moreover, comparing with any other stiffness such as , is small. With this in mind, $K_l^c omp$ could be approximately treated as small constants around 30 MPa in the simulation.

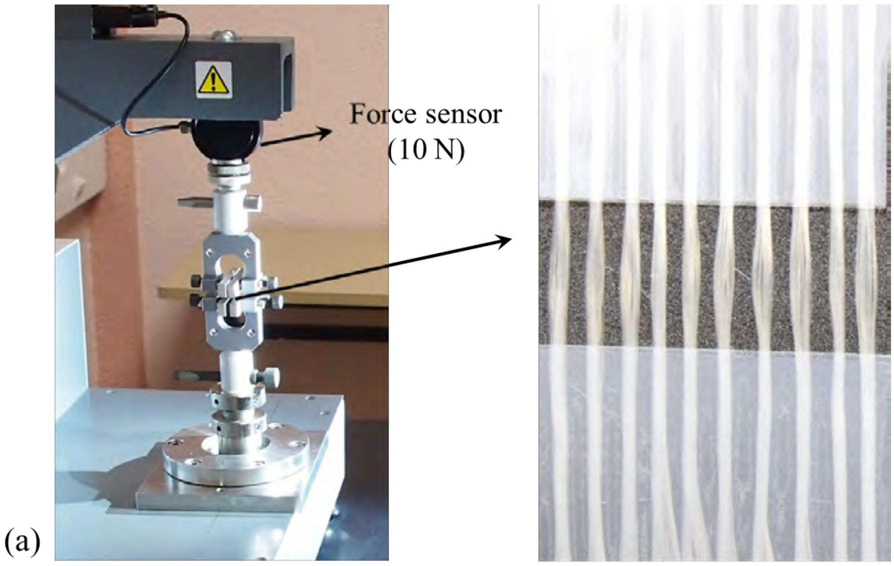

FIGURE 3.13 – The yarn sample during a longitudinal compression test

Now the longitudinal stiffness K_l is divided into two parts : the elongation stiffness K_l^{tens} and the longitudinal compression stiffness K_l^{comp} (FIG. 3.15) :

$$\begin{cases} K_l = K_l^{tens} & if \quad \varepsilon_l \geq 0 \\ K_l = K_l^{comp} & if \quad \varepsilon_l < 0 \end{cases} \tag{3.47}$$

Stiffness gap problem

The stiffness gap between K_l^{tens} and K_l^{comp} (FIG. 3.15) could be very large (*e.g.,* for the warp yarn in tapas fabric, this difference can be 18900 N/yarn). Although this gap is physically reasonable (in other words, it is the physical characteristic of the yarn), as will be shown, such a sudden and large transformation in the stiffness curve leads to incompatibility problem in F.E. simulations, and it is called *stiffness gap problem* in this study. A 2-element structure is applied (FIG. 3.16) to explain how the stiffness gap influences the simulation. $(\varepsilon_l^n)_A$ and $(\varepsilon_l^n)_B$ are the longitudinal strain states of elements A and B at the beginning of a time step n. Assuming they fulfill the following relations :

$$\begin{aligned} (\varepsilon_l^n)_A > 0 \\ (\varepsilon_l^n)_B < 0 \end{aligned} \tag{3.48}$$

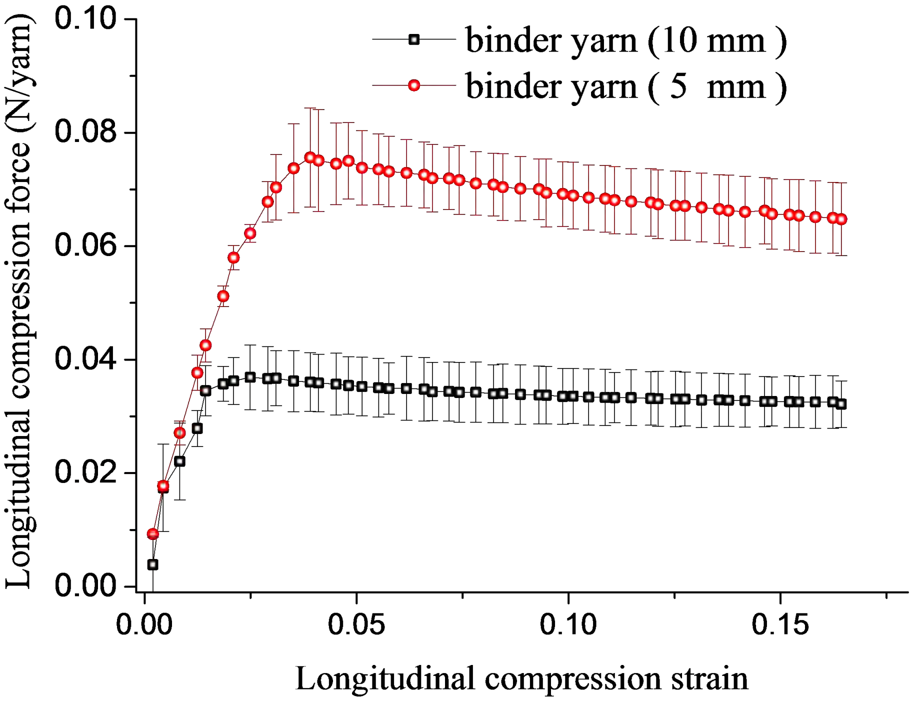

FIGURE 3.14 – The longitudinal compression curves of the three yarns (with length of 10 mm)

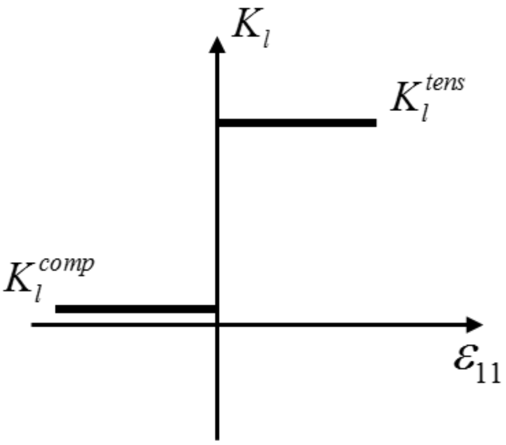

FIGURE 3.15 – K_l is decomposed into K_l^{comp} and K_l^{tens}

According to EQ. (3.47) and EQ. (3.48),the longitudinal stiffness of element A and element B at the beginning of this time step n are :

$$\begin{aligned} (K_l^n)_A &= K_l^{tens} \\ (K_l^n)_B &= K_l^{comp} \end{aligned} \tag{3.49}$$

so $(K_l^n)_A \gg (K_l^n)_B$. When the elements are stretched under forces or displacements, element B would have a larger deformation than element A, which leads to distortion of structure. An compaction simulation on the RUC of tapas fabric is given in FIG. 3.16. The RUC of tapas fabric is compressed transversely and the simulation is not finished successfully because of the distortion of some elements.

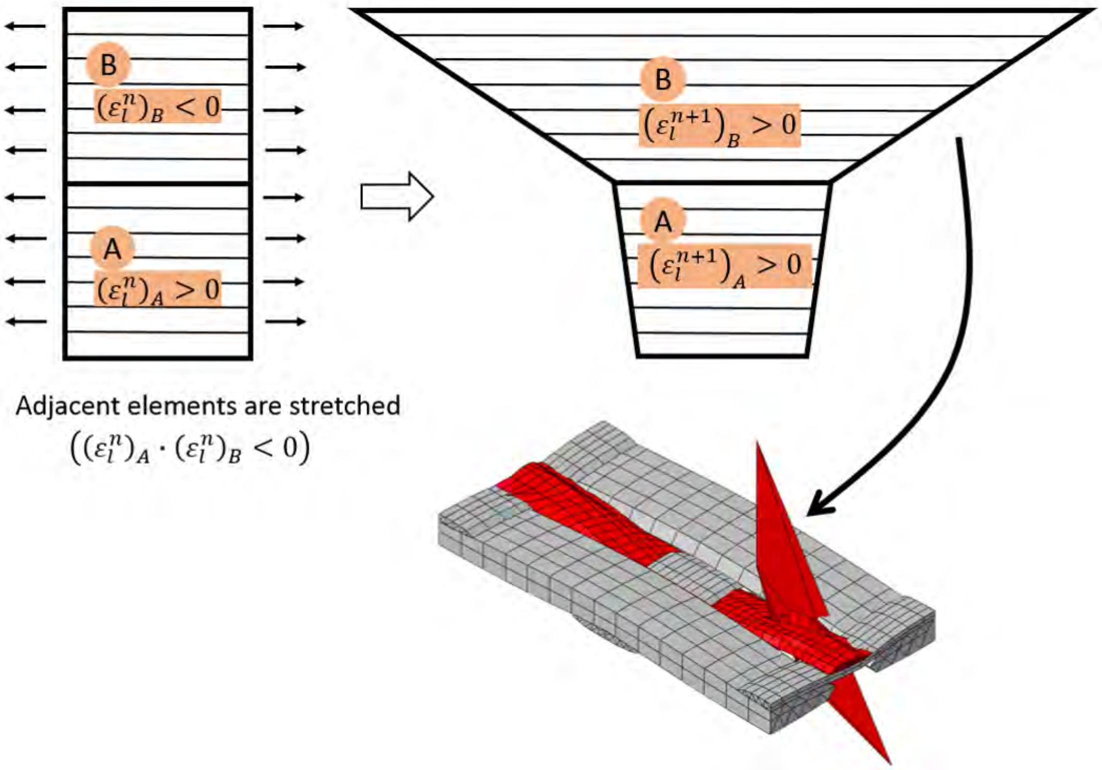

FIGURE 3.16 – The explanation for the stiffness gap problem

Solutions for stiffness gap problem

On the one hand, it has been pointed out that the stiffness curve of K_l in FIG. 3.15 could reflect the real characteristic of the yarn, that is to say, the stiffness gap between the longitudinal compression stiffness K_l^{comp} and elongation stiffness K_l^{tens} is physically reasonable. On the other hand, it has been proved that this stiffness gap makes the structure unstable in the F.E. numerical simulation. The stiffness gap problem should be well studied.

In F.E. method, the stiffness of an element in one time increment (Δt) is constant. This approximation is based on a precondition : the change of the real stiffness in Δt should be small enough. In view of this, normal F.E. code is incapable of dealing with sudden variation of stiffness, such as the stiffness gap in FIG. 3.15. To explain this more clearly, the element B in FIG. 3.16 is applied as an example. As is discussed, the initial and final strain state of element B in step *n* are :

$$\begin{aligned}(\varepsilon_l^n)_B &< 0 \\ \left(\varepsilon_l^{n+1}\right)_B &> 0\end{aligned} \tag{3.50}$$

as is shown in FIG. 3.17. The exact stress increment $(\Delta\sigma_l^n)$ should be written as the difference between $(\sigma_l^n)_B$ and $(\sigma_l^{n+1})_B$:

$$\begin{aligned}(\Delta\sigma_l^n)_B &= (\sigma_l^{n+1})_B - (\sigma_l^n)_B \\ &= \frac{K_l^{tens}}{S}\cdot(\varepsilon_l^{n+1})_B - \frac{K_l^{comp}}{S}\cdot(\varepsilon_l^n)_B\end{aligned} \tag{3.51}$$

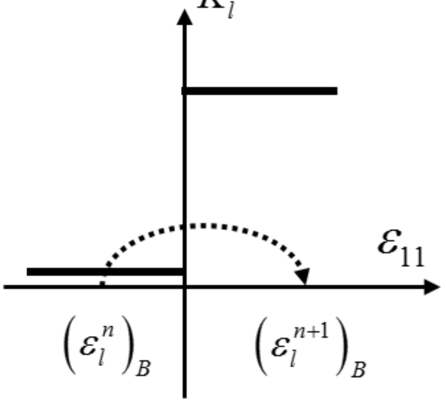

FIGURE 3.17 – The stress updating of element B in FIG. 3.16

However in the F.E. process, there is an approximate treatment : the longitudinal stiffness of the element is a constant that is evaluated at the beginning of the time step. Considering that at the beginning of the time step n, the longitudinal stiffness of element B is K_l^{comp}, the stress increment in the F.E. simulation is :

$$(\Delta\sigma_l^n)_B^{FE} = \frac{K_l^{comp}}{S}\cdot\left((\varepsilon_l^{n+1})_B - (\varepsilon_l^n)_B\right) \tag{3.52}$$

the error of this F.E. increment is :

$$\begin{aligned}(\Delta\sigma_l^n)_B^{FEerror} &= (\Delta\sigma_l^n)_B - (\Delta\sigma_l^n)_B^{FE} \\ &= \frac{K_l^{tens} - K_l^{comp}}{S}\cdot(\varepsilon_l^{n+1})_B\end{aligned} \tag{3.53}$$

this expression of error has an important significance, because it reveals how the F.E. process is affected by the stiffness gap.

EQ. (3.53) implies two possible ways to solve the stiffness gap problem : minifying the magnitude of the $\mid(\varepsilon_l^{n+1})_B\mid$ or scaling down the gap magnitude $\Delta K = K_l^{tens} - K_l^{comp}$. Or a more radical solution is replacing the stress updating process in EQ. (3.52) with a new stress updating strategy. These three strategies will be tested in sequence.

1. The 1^{st} solution for stiffness gap problem
   According to EQ. (3.53), restraining the value of $|(\varepsilon_l^{n+1})_B|$ could minify the F.E. error caused by stiffness gap problem. This is the main idea of the first solution for stiffness gap problem. This most direct way to restraining $|(\varepsilon_l^{n+1})_B|$ is constraining critical time step Δt. In order to check whether this strategy could solve the stiffness gap problem in FIG. 3.16, the compaction simulation on RUC of tapas fabric is repeated with a fixed critical time increment of 1E-7. The result in FIG. 3.23a shows that those distorted elements in FIG.3.16 basically disappear in the new simulation result. In spite of this, the shortcoming of this strategy is apparent : smaller critical step time leads to longer computation time. The normal computation time for the compaction simulation on tapas RUC is around 4 minutes (8 multiple processors), but it takes almost 1 hour (8 multiple processors) when the critical time is 1 E-7, which is unacceptable from the perspective of computational efficiency. So this strategy is recommended only when the model is small.
2. The 2^{nd} solution for stiffness gap problem According to EQ. (3.53), scaling down ΔK_{gap} can be helpful to constrain the F.E. error. This is the main idea of this 2^{nd} solution for stiffness gap problem. The magnitude of the stiffness gap is :

$$\Delta K_{gap} = K_l^{tens} - K_l^{comp} \tag{3.54}$$

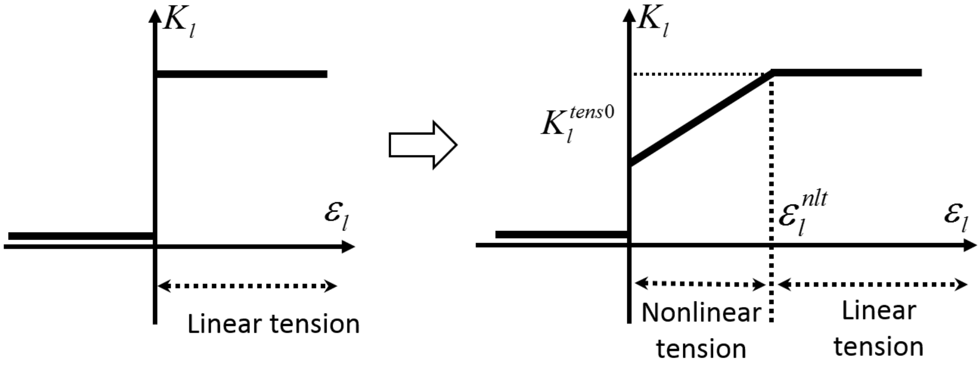

FIGURE 3.18 – The diagram to explain how the nonlinear tension is considered

For the purpose of reducing ΔK_{gap}, the nonlinear parts of the tension curves (FIG. 1.9a) are recalled. A diagram is displayed in FIG. 3.18, in which the longitudinal stiffness K_l includes three parts : the longitudinal stiffness K_l^{comp}, the nonlinear tensile stiffness and the linear tensile stiffness. So there are two unknown parameters for each yarn : the initial tension stiffness K_l^{tens0} and the demarcation longitudinal strain ε_l^{nlt} between the nonlinear tension part and linear tension part. These parameters can be measured from the tension stiffness curves of yarns in tapas fabric (FIG. 3.19 displays the slope information of the tension curves in FIG. 1.9a). They are listed in table 3.4. In this way, the stiffness gap is reduced to :

$$\Delta K_{gap} = K_l^{tens0} - K_l^{comp} \tag{3.55}$$

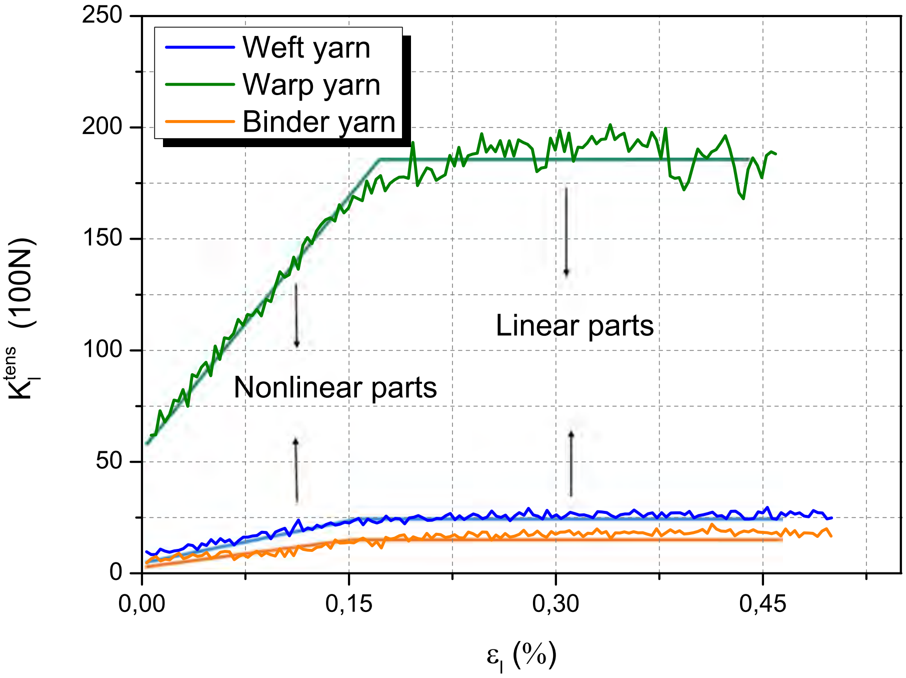

FIGURE 3.19 – Tension stiffness of the yarns in tapas fabric

Parameter	ε_l^{nlt}	$K_l^{tens0}(N)$
Warp	0.2%	6004
Binder	0.15%	855
Weft	0.15%	916

TABLE 3.4 – Nonlinear tensile parameters of tapas fabric

In order to check whether this strategy could solve the stiffness gap problem in FIG. 3.16, the compaction simulation on RUC of tapas fabric is repeated. The nonlinear tension parts of the yarns are considered in K_l, and the simulation result is shown in FIG. 3.23b. The result shows that those distorted elements in FIG.3.16 basically disappear. In spite of this, it has to be emphasized that the stiffness gap problem cannot be solved radically by this strategy, since the gap ΔK_l still exists. Moreover, adding the nonlinear tensile parts into the model makes the simulation complex and reduces the simulation efficiency.

3. The 3^{rd} solution for stiffness gap problem

   As is discussed above, two strategies have been tried to solve the incompatibility problem between the elongation stiffness K_l^{tens} and K_l^{comp}, but none of them could provide an ideal resolution. They could only decrease the error expressed in EQ. (3.53), instead of eliminating it thoroughly. To radically eliminate the F.E.

error $(\Delta\sigma_l^n)_B^{FEerror}$ (EQ. (3.53)), the 3^{rd} strategy is developed here to modify the stress updating process in F.E. loops. As will be shown, this strategy is a thorough solution since the error expression can be constrained to zero.

In a given time step during the F.E. simulation, the stiffness matrix of element ($\mathbf{K}^n_{element}$) is normally calculated at the beginning of time step and keeps constant during the whole time increment :

$$\mathbf{K}^n_{element} \equiv \mathbf{K}_{element}(t^n) \tag{3.56}$$

this is reasonable in most cases, because normally the change of stiffness matrix in a limited increment is small and can be ignored. In other words, The approximated approach in EQ. (3.56) is based on a precondition : the stiffness should not change extremely. The longitudinal stiffness curve for the composite yarn (FIG. 3.15) cannot fulfill this precondition, because of the existence of stiffness gap. So the F.E. codes should be improved to adapted to this character of composite yarn. To be exact, for those time steps influenced by stiffness gap, the stress updating process should be improved.

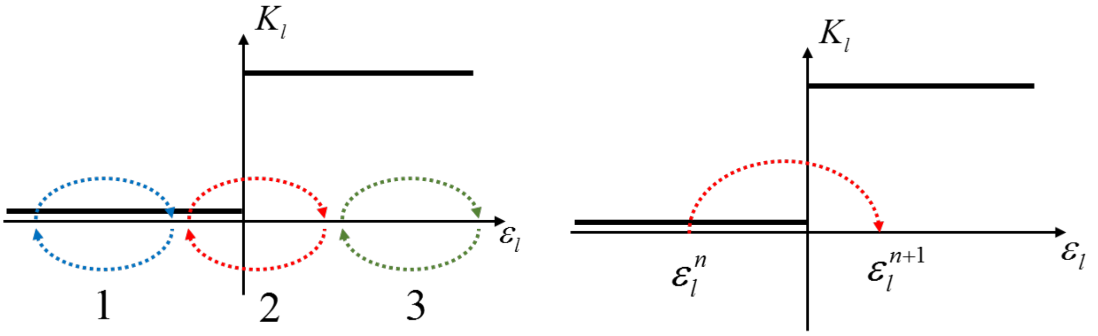

(a) Three different time steps according to the positon of stiffness gap **(b)** Updating stress for the 2^{nd} kind of time step in FIG. 3.20a

FIGURE 3.20 – A modification of the stress updating strategy in F.E. process, aiming to solve the stiffness gap problem

FIG. 3.20a shows three kinds of time steps according to their relative positions with the point of stiffness gap. The 1^{st} and 3^{rd} kind of steps are not affected by the stiffness gap points, thus the corresponding stress updating could be done in the normal way :

$$\begin{aligned} \Delta\sigma_l^n &= \frac{K_l^{comp}}{S} \cdot \Delta\varepsilon_l^n \\ or\ \ \Delta\sigma_l^n &= \frac{K_l^{tens}}{S} \cdot \Delta\varepsilon_l^n \end{aligned} \tag{3.57}$$

where S is the area of cross section. For the 2^{nd} kind of time step ($e.g.$,$\varepsilon_l^n < 0 < \varepsilon_l^{n+1}$), the stress increment is the sum of a compaction part and tension part

(FIG. 3.20b) :

$$\begin{aligned}\Delta\sigma_l^n &= (\Delta\sigma_l^n)^{tens} + (\Delta\sigma_l^n)^{comp} \\ &= \frac{K_l^{tens}}{S} \cdot (\Delta\varepsilon_l^n)^{tens} + \frac{K_l^{comp}}{S} \cdot (\Delta\varepsilon_l^n)^{comp}\end{aligned} \tag{3.58}$$

where $(\Delta\varepsilon_l^n)^{tens}$ and $(\Delta\varepsilon_l^n)^{comp}$ are (according to FIG. 3.20b) :

$$\begin{aligned}(\Delta\varepsilon_l^n)^{comp} &= \varepsilon_l^n \\ (\Delta\varepsilon_l^n)^{tens} &= \varepsilon_l^{n+1}\end{aligned} \tag{3.59}$$

ε_l^n and ε_l^{n+1} (ε_l^{n+1} is calculated based on the stiffness matrix of t^n, which is updated in last step) are calculated and passed into VUMAT. So they are known before stress updating. Plugging EQ. (3.59) into EQ. (3.58) :

$$\Delta\sigma_l^n = \frac{K_l(\varepsilon_l^{n+1})}{S} \cdot \varepsilon_l^{n+1} - \frac{K_l(\varepsilon_l^n)}{S} \cdot \varepsilon_l^n \tag{3.60}$$

where $K_l(\varepsilon_l)$ is expressed in EQ. (3.47). So $K_l(\varepsilon_l^n)$ and $K_l(\varepsilon_l^{n+1})$ could be K_l^{comp} or K_l^{tens}.

EQ. (3.60) gives the right stress increment when the time step is influenced by the stiffness gap, and in order to realize this stress updating, the following longitudinal stiffness should be applied in the corresponding F.E. loop :

$$\begin{aligned}K_l &= \frac{\Delta\sigma_l^n}{\varepsilon_l^{n+1} - \varepsilon_l^n} \\ &= \frac{K_l(\varepsilon_l^{n+1}) \cdot \varepsilon_l^{n+1} - K_l(\varepsilon_l^n) \cdot \varepsilon_l^n}{(\varepsilon_l^{n+1} - \varepsilon_l^n) \cdot S}\end{aligned} \tag{3.61}$$

This expression is in fact a value averaged from K_l^{comp} and K_l^{tens}. This can be more clearly understood in a diagram of $Strain - Load$ curve (FIG. 3.21), in which the stiffness gap corresponds to an extreme transition. When $\varepsilon_l^n \cdot \varepsilon_l^{n+1} \leq 0$, the value of K_l^n is neither K_l^{comp} nor K_l^{tens}. It is the slope value of the red ligature, which is decided by the relative size of ε_l^n and ε_l^{n+1} : when ε_l^n is larger, the slope value is closer to K_l^{comp} and vice versa.

Although all the above-mentioned conclusions are derived for the circumstance of $\varepsilon_l^n < 0 < \varepsilon_l^{n+1}$, they also apply to the circumstance of $\varepsilon_l^{n+1} < 0 < \varepsilon_l^n$.

As a conclusion, the 3^{rd} method to solve the stiffness gap problem is shown in the diagram of FIG. 3.22. It can be realized by VUMAT interface in ABAQUS. In order to check whether this strategy could solve the stiffness gap problem in FIG. 3.16, the compaction simulation on RUC of tapas fabric is repeated. The mechanical model is updated according to the diagram of FIG. 3.22. The results in FIG. 3.23c finishes in 4 minutes (8 multiple processors), which means the simulation efficiency is not affected. Most importantly, the numerical wrinkles disappeared completely in the simulation result.

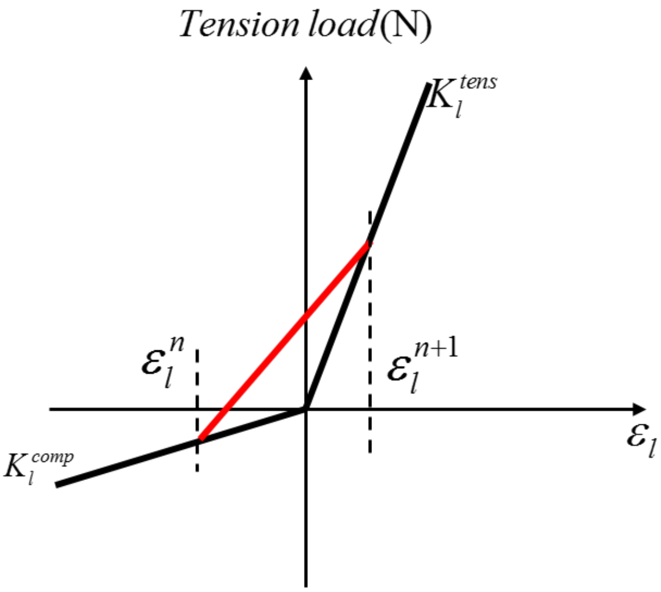

FIGURE 3.21 – A diagram of $\varepsilon_l - load$ curve

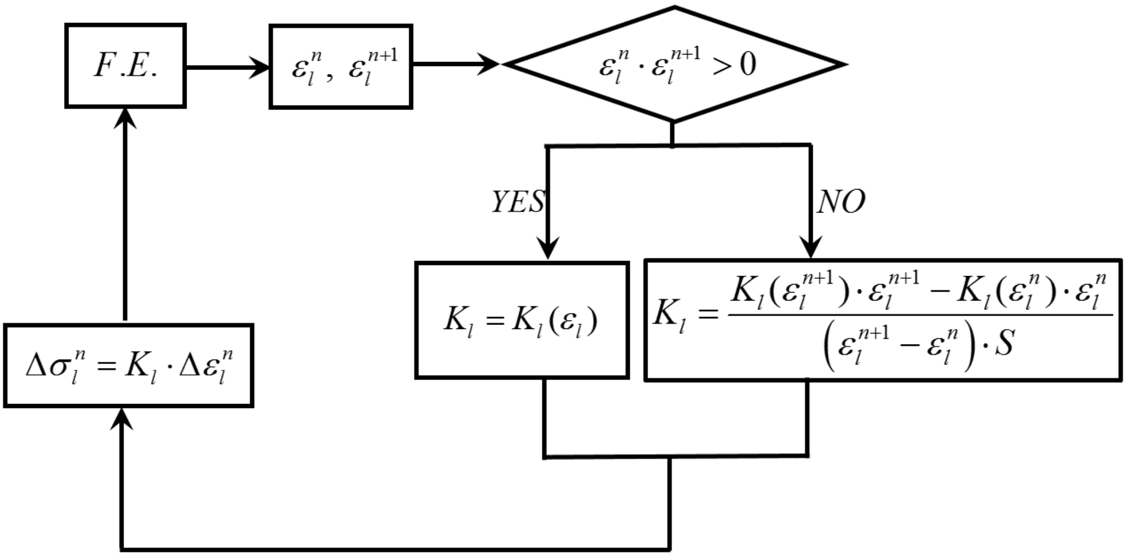

FIGURE 3.22 – A diagram of the 3^{rd} strategy for stiffness gap problem

3.3.3 Conclusion of longitudinal compression mode

Yarn's longitudinal compression stiffness is small. In order to distinguish it from tension stiffness K_l^{tens}, the longitudinal compression mode is developed. It is found the largest challenge is the incompatibility phenomenon between K_l^{tens} and K_l^{comp}, in light of the gap between them. To solve the stiffness gap problem, three different strategies are applied.

In the first attempt, the critical time increment is constrained to a small value, and it works well when the critical time is small enough (FIG. 3.23a). The advantage of this

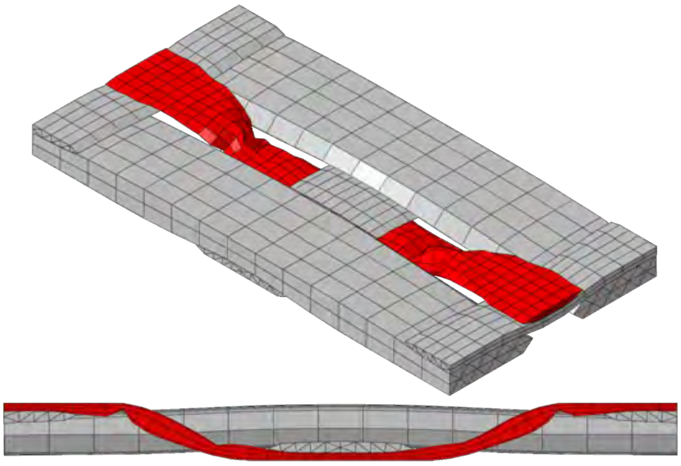

(a) The 1^{st} strategy ($\Delta t \equiv 1E-7$) to solve the stiffness gap problem

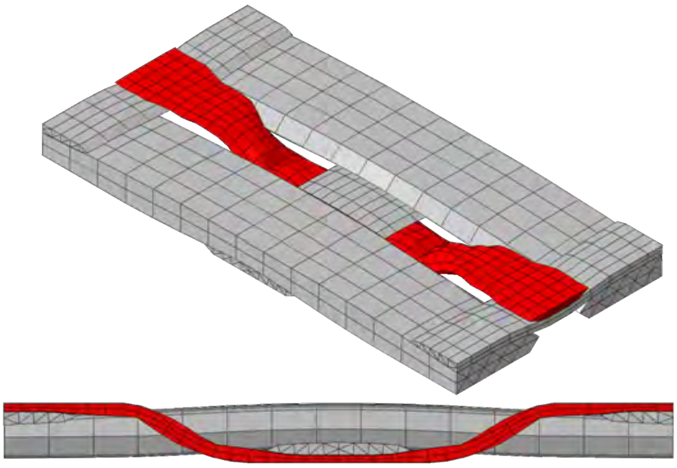

(b) The 2^{nd} strategy to solve the stiffness gap problem

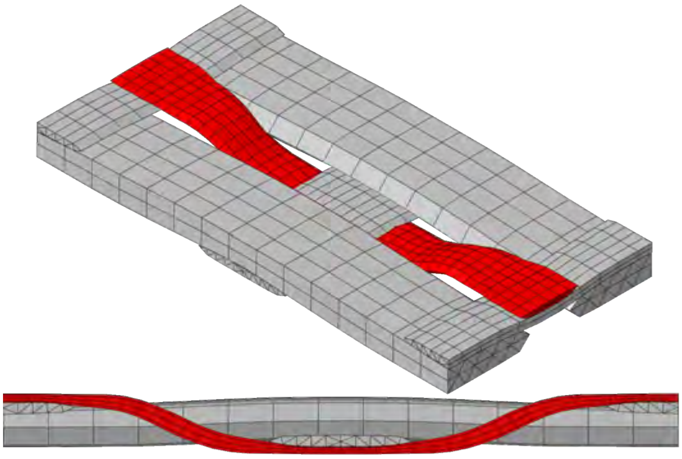

(c) The 3^{rd} strategy to solve the stiffness gap problem

FIGURE 3.23 – Comparison of efficacies of the three strategies for stiffness gap problem

strategy lies in its simplicity, but it is time consuming. So it is not workable for large structures.

The 2^{nd} strategy make use of the nonlinear phenomenon when the yarn is stretched. The nonlinear part of the tensile curve is used to diminish the stiffness gap. Its advantage is that, compared with the 1^{st} strategy, the simulation result is ameliorated without prolonging the simulation duration (FIG. 3.23b). In spite of this, the weakness is obvious : the gap cannot be eliminated from the root, and the result is barely satisfactory.

In order to thoroughly remove the F.E. error from the stiffness gap, the stress updating process is modified in the 3^{rd} strategy. The time increments are divided into different groups according to their relative position with the stiffness gap point. For those influenced by the gap problem, the longitudinal stiffness is defined as a value averaged from K_l^{tens} and K_l^{comp}. This strategy has almost no influence on the computation duration, and the final simulation result is quite acceptable (FIG. 3.23c).

Comparing the efficiency of the three strategies in FIG. 3.23, the 3^{rd} strategy is much better than the other two. For this reason, it is recommended to be applied for the longitudinal compression mode, and it will be used in the following simulations by default.

3.4 Transverse expansion mode

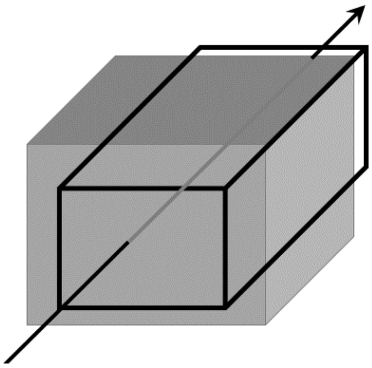

FIGURE 3.24 – The deformation mode of transverse expansion

The simulation result in FIG. 3.9 shows two defects of the initial mesoscale mechanical model described in section 3.2. The first one is the spurious wrinkle and has been solved by the longitudinal compression model in the last section. Besides the spurious wrinkles, it is also found that the transverse expansion of the yarn is not enough, and there are more and larger voids between adjacent yarns in the simulation result (FIG. 3.9b). This problem will be analyzed in this section.

The yarn's transverse deformation is affected by the load along the yarn. Nevertheless no deformation mode in the initial mesoscale mechanical model described in section 3.2 could reflect this phenomenon. For this reason, the transverse expansion mode (FIG. 3.24) is developed. The need of the transverse expansion mode will be firstly emphasized through the tomography observation, after which the transverse expansion mode is constructed. Finally an optical experiment and an inverse fitting process is carried out to identify the parameters.

3.4.1 The necessity of transverse expansion mode

As is mentioned, tomography is an useful tool to observe the internal structure of the loaded fabric. Two kinds of tomography observations are carried out for the transverse phenomenon of the yarn. They are realized on the tomography machine of laboratory MATEIS, INSA De Lyon (FIG. 2.1).

The first one is carried out for a transversely compacted tapas fabric. The resolution is 10 μm, and gives a mesoscopic view of the deformed tapas fabric (FIG. 3.26b). The fabric is compressed from initial state to a loaded state with a compaction ratio of 55.4 % . Expansion of the yarn exists in the compressed fabric, and the expansion ratio of the binder yarn can be larger than 50% in some areas. However, the same transverse expansion could not be found in the simulation in FIG. 3.26d, noting that the mechanical model used in the simulation in the one developed at the end of section 3.3 (the initial mesoscale mechanical model + the longitudinal compression mode). As can be seen, there is almost no transverse expansion on the binder yarn. This implies the necessity of the transverse expansion mode.

To get a better understanding of the fibers' behavior when the yarn is compressed longitudinally, a microscale tomography experiment is required. For this purpose, a yarn sample is compressed longitudinally ($\varepsilon_l \approx -5\%$) and scanned by the tomography device with a resolution of 5 μm (FIG. 3.25). The deformations of the fibers in this longitudinally compressed yarn seem like buckling and bending. The magnitudes of these deformations are very large, *e.g.*, the yarn's middle part almost doubles in width. So transverse expansion deformation rising from the longitudinal compression should be well studied.

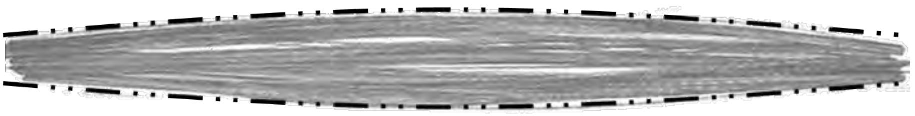

FIGURE 3.25 – Tomography observation of transverse expansion of the longitudinally compressed yarn (the ends of the yarn are fixed ; the longitudinal compaction ratio of this yarn is around -5%)

3.4.2 Construction of transverse expansion mode

Transverse expansion mode should reflect the influence from longitudinal deformation to transverse expansion, so it is to be constructed by means of longitudinal-transverse Poisson ratio, which is marked as υ_{lt}. As announced previously, *l* denotes the longitudinal direction while *t* is for transverse direction of the yarn. When the hypo elastic law is adapted as the stress update strategy, the corresponding Poisson ratio is expressed by

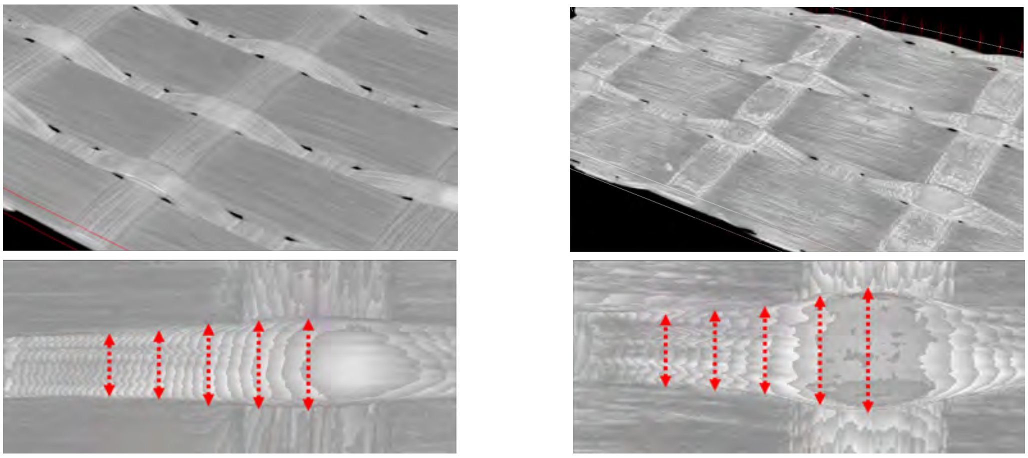

(a) Before compaction

(b) After compaction, the expansion of the yarn (compaction ratio is 55.4%)

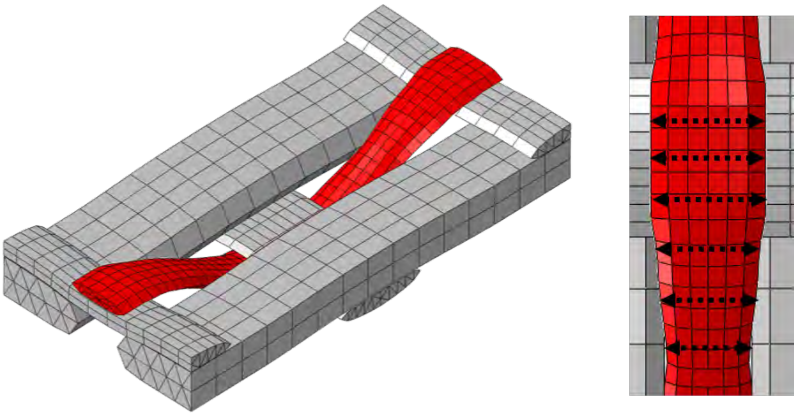

(c) Before compaction

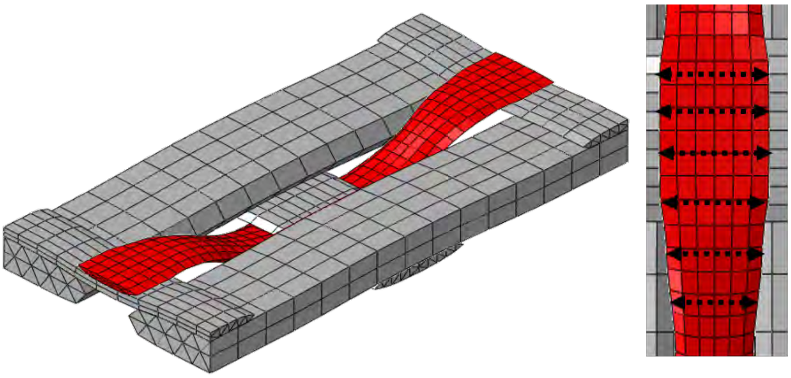

(d) After compaction, the transverse expansion of the yarn is small (compaction ratio is 55.4%)

FIGURE 3.26 – The transverse expansion of the yarn in simulation is too small (the transverse expansion mode is not considered in the mechanical model of the simulation)

increment quantities :

$$\upsilon_{lt} = -\frac{\Delta\varepsilon_t}{\Delta\varepsilon_l} \tag{3.62}$$

By the way, there is another similar Poisson ratio between longitudinal and transverse section that is marked as υ_{tl}. However as is known to all, υ_{tl} is not independent of υ_{lt} :

$$\upsilon_{tl} = \frac{E_t}{E_l} \cdot \upsilon_{lt} \tag{3.63}$$

where E_l is the longitudinal Young's Modulus and E_t is the transverse one, and both of them are known during the numerical simulation :

$$\begin{aligned} E_l &= K_l/S \\ E_t &= \frac{2A \cdot B}{A+B} \end{aligned} \tag{3.64}$$

where the meanings of A and B are the same with those in section 3.2. Before studying the value of υ_{lt}, three points are worth mentioning :

1. It has been mentioned that, for the mesosopic mechanical model introduced in section 3.2, the cross section of the yarn is isotropic. To keep compatible with this assumption, υ_{lt} should also be assumed to be transversely isotropic (FIG. 3.27), which might be inconsistent with the physical reality. Nevertheless as will be shown, it is found in the experiment that when the longitudinal compression is limited ($|\varepsilon_l| < 5\%$), υ_{lt} is independent of the geometry dimension of the yarn, so the transverse isotropy assumption is acceptable.

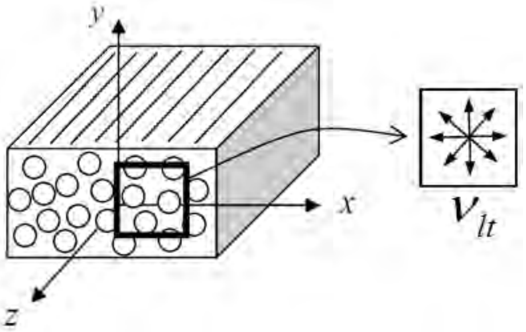

FIGURE 3.27 – In order to keep compatible with the model presented in section 3.2, υ_{lt} should be assumed to be constant in the transverse section

2. The yarn would expand transversely when it is compressed longitudinally, however when the yarn is stretched, the fibers tend to stay straight, and υ_{lt} could be considered as zero :

$$\upsilon_{lt} = 0 \quad if \;\; \varepsilon_l \geq 0 \tag{3.65}$$

3. The longitudinal compression is normally slight during the deformation of textile composite. This is because the bending stiffness of the yarn is normally small, so when the longitudinal compression arrives a certain degree, the bending of yarn would appear, which precludes the possibility of a large longitudinal compression. *E.g.*, for the tapas fabric in this study, it is found in the simulations that ε_l is always larger than -5%. As will be shown, this precondition simplifies the work to measure the value of υ_{lt}.

Now υ_{lt} can be supplemented into the constitutive model. For the purpose of brevity, this work will be effectuated by means of compliance matrix $[D]^{\Phi}$. As is known, it has a inverse relation with stiffness matrix $[C]^{\Phi}$:

$$[D]^{\Phi} = [C]^{\Phi^{-1}} \tag{3.66}$$

Φ implies that this constitutive relation is expressed on the fiber base (see EQ. (3.29)). So the stiffness matrix in EQ. (3.46) could be written in its compliance form :

$$[D]^{\Phi} = \begin{bmatrix} \frac{1}{E_l} & 0 & 0 & 0 & 0 & 0 \\ & \frac{A+B}{2A\cdot B} & \frac{B-A}{2A\cdot B} & 0 & 0 & 0 \\ & & \frac{A+B}{2A\cdot B} & 0 & 0 & 0 \\ & & & \frac{1}{G_{lt}} & 0 & 0 \\ & syms & & & \frac{1}{B} & 0 \\ & & & & & \frac{1}{G_{lt}} \end{bmatrix} \tag{3.67}$$

where the meaning of A and B can be found in section 3.2. It is convenient to add the υ_{lt} into compliance matrix, since υ_{lt} only concerns two independent elements in $[D]^{\Phi}$:

$$[D]^{\Phi} = \begin{bmatrix} \frac{1}{E_l} & -\frac{\upsilon_{lt}}{E_l} & -\frac{\upsilon_{lt}}{E_l} & 0 & 0 & 0 \\ & \frac{A+B}{2A\cdot B} & \frac{B-A}{2A\cdot B} & 0 & 0 & 0 \\ & & \frac{A+B}{2A\cdot B} & 0 & 0 & 0 \\ & & & \frac{1}{G_{lt}} & 0 & 0 \\ & syms & & & \frac{1}{B} & 0 \\ & & & & & \frac{1}{G_{lt}} \end{bmatrix} \tag{3.68}$$

$[D]^{\Phi}{}_{12}$ and $[D]^{\Phi}{}_{13}$ has the same expression because of the transverse isotropy assumption. EQ. (3.66) is turned to account again to calculate $[C]^{\Phi}$:

$$[C]^{\Phi} = \begin{bmatrix} \frac{E_l^2}{E_l - 2A\cdot\upsilon_{lt}^2} & \frac{A\cdot E_l\cdot\upsilon_{lt}}{E_l - 2A\cdot\upsilon_{lt}^2} & \frac{A\cdot E_l\cdot\upsilon_{lt}}{E_l - 2A\cdot\upsilon_{lt}^2} & 0 & 0 & 0 \\ & \frac{2A\cdot B\cdot\upsilon_{lt}^2 - (A+B)E_l}{2E_l - 4A\cdot\upsilon_{lt}^2} & \frac{2A\cdot B\cdot\upsilon_{lt}^2 + (A-B)E_l}{2E_l - 4A\cdot\upsilon_{lt}^2} & 0 & 0 & 0 \\ & & \frac{2A\cdot B\cdot\upsilon_{lt}^2 - (A+B)E_l}{2E_l - 4A\cdot\upsilon_{lt}^2} & 0 & 0 & 0 \\ & & & G_{lt} & 0 & 0 \\ & syms & & & B & 0 \\ & & & & & G_{lt} \end{bmatrix} \tag{3.69}$$

according to the prerequisite of positive definiteness of strain energy density, the determinant of $[C]^{\Phi}$ should be positive :

$$det([C]^{\Phi}) \ > \ 0 \tag{3.70}$$

which leads to a restriction on the value range of υ_{lt} :

$$0 \leq \upsilon_{lt} < \sqrt{\frac{E_l}{2A}} \tag{3.71}$$

Experimental setup to record the transverse expansion

To measure the Poisson ratio υ_{lt} of the yarns in the tapas fabric, the transverse expansion phenomenon should be recorded and measured. Since it would be difficult to measure the transverse expansion of the yarn from the fabric directly, the experiment could be carried out on single yarns. In this case, it is important to make sure the states of the yarns (the shape, the tightness, *etc.*) are not changed when the yarn is moved out of the fabric.

To measure the deformation of the yarn, optical methodology is preferred since it is precise and could avoid destructive factors. For this reason, the experiment setup (FIG. 3.28) is designed. It is based on Zwick Meca Bi-axes of LaMCoS, INSA de Lyon. The ends of the yarn are fixed on two fixtures that can move towards each other. A high resolution camera is positioned above the sample to record the compression process. The compression velocity is 2 mm/min and the camera takes 10 photos every second. Here are several notes worth mentioning.

1. In the woven fabric the yarn is curved constantly, so that its straight segments are short. *E.g.*, the size of the straight yarn segments in tapas fabric is shown in FIG. 3.29. Referring to this, the length of the yarn samples should be shorter than 10 mm.

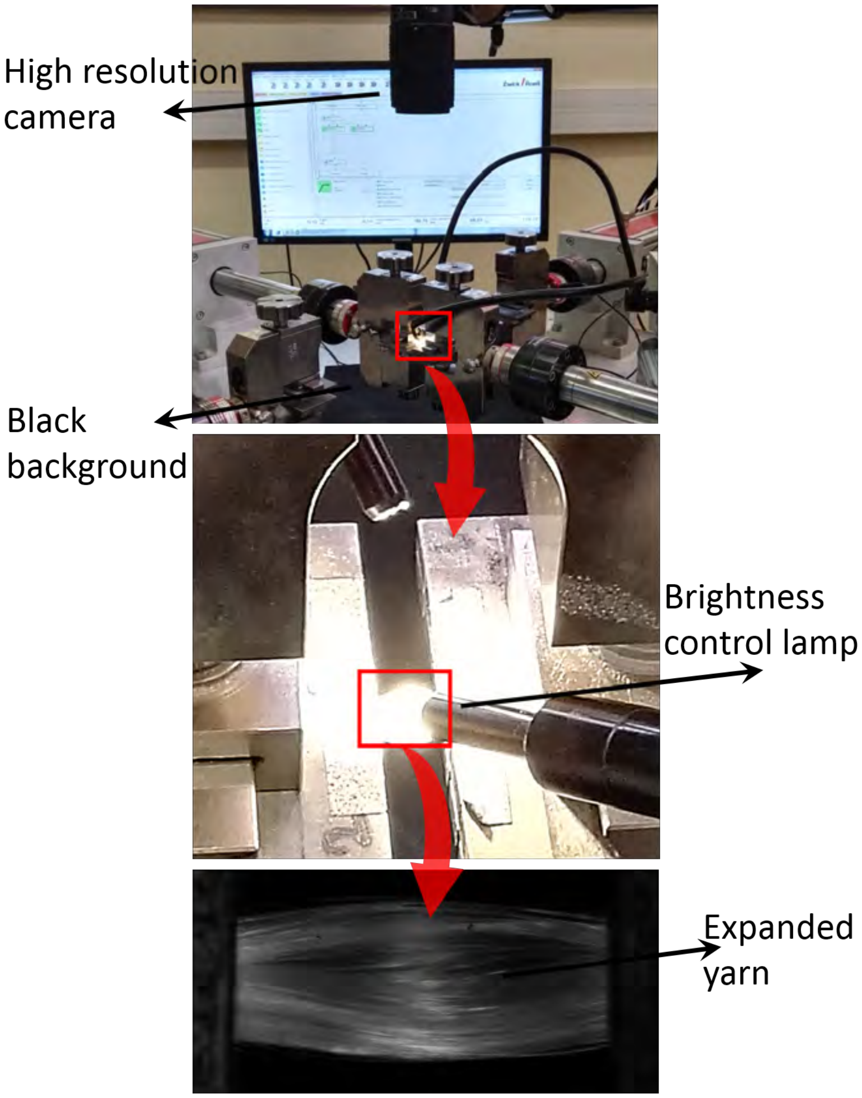

FIGURE 3.28 – The experiment setup to measure the transverse expansion

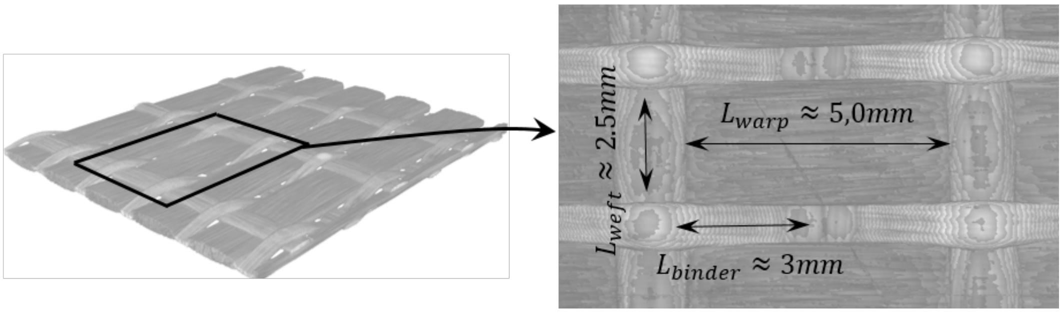

FIGURE 3.29 – The dimension of the straight yarn segments in tapas fabric

2. It has been highlighted that the yarn sample should keep its state (fiber tightness, section shape, *etc.*) when the experiment is prepared. In this study the liquid glue is applied to stick the yarn on the holders, the ends of the yarn is fixed firmly when the glue becomes dry.
3. The expansion of the yarn is measured from the images, so it is important to use the lamp to adjust the brightness (FIG. 3.28), and black backdrop is placed in the background to improve the contrast between the yarn and the environment.

Processing the experiment images

To measure the expansion of the yarn, the boundaries of the yarn should be found in the images. Here is an example to explain how the images are processed : the initial length of the yarn is 10 mm, and its initial visible width is 2 mm. The largest longitudinal compression in the experiment is $\varepsilon_l = -4.422\%$ (FIG. 3.30). An image is in fact a matrix of brightness value from 0 to 255 ('0' denotes absolute black while '255' is absolute white). The brightness demarcation between yarn and background is effected by many factors such as the brightness of lamps and experiment site, so this value should be found out individually for each experiment. This is not difficult for a high-contrast image, because the matrix gradient is very large near the boundary (FIG. 3.30), the values change sharply from values smaller than 10 to values larger than 20. So for this group of experiment, the brightness demarcation is 10 (any number between 9 and 13 are acceptable, since their corresponding boundaries differs by just several micrometers).

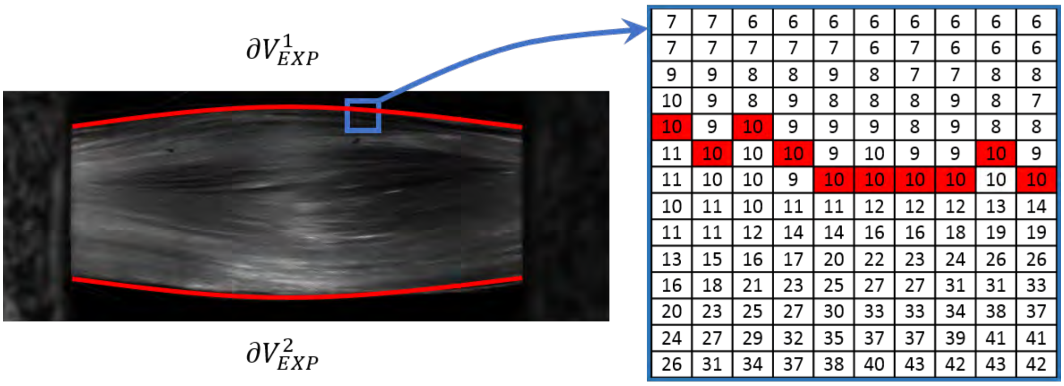

7	7	6	6	6	6	6	6	6	6
7	7	7	7	7	6	7	6	6	6
9	9	8	8	9	8	7	7	8	8
10	9	8	9	8	8	8	9	8	7
10	9	10	9	9	9	8	9	8	8
11	10	10	10	9	10	9	9	10	9
11	10	10	9	10	10	10	10	10	10
10	11	10	11	11	12	12	12	13	14
11	11	12	14	14	16	16	18	19	19
13	15	16	17	20	22	23	24	26	26
16	18	21	23	25	27	27	31	31	33
20	23	25	27	30	33	33	34	38	37
24	27	29	32	35	37	37	39	41	41
26	31	34	37	38	40	43	42	43	42

FIGURE 3.30 – Extracting the boundaries of the yarn

The upper and lower boundary of the yarn are ∂V^1_{EXP} and ∂V^2_{EXP}. The average shape of ∂V^1_{EXP} and ∂V^2_{EXP} is shown in FIG. 3.30.

Inverse fitting process to measure the υ_{lt}

In order to study how the υ_{lt} varies with ε_l, the compression is discretized averagely into six stages (FIG. 3.32a).

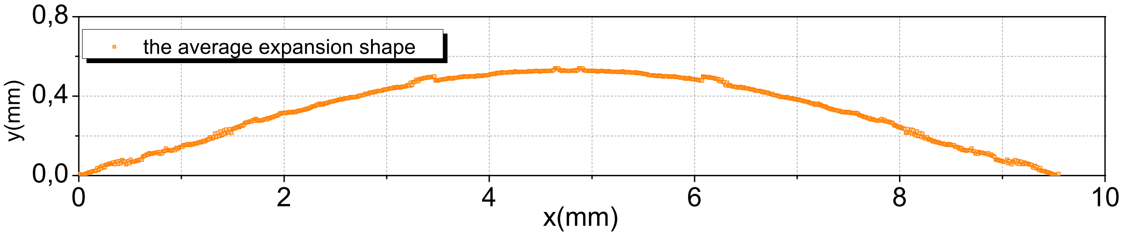

FIGURE 3.31 – The average shape of ∂V^1_{EXP} and ∂V^2_{EXP}

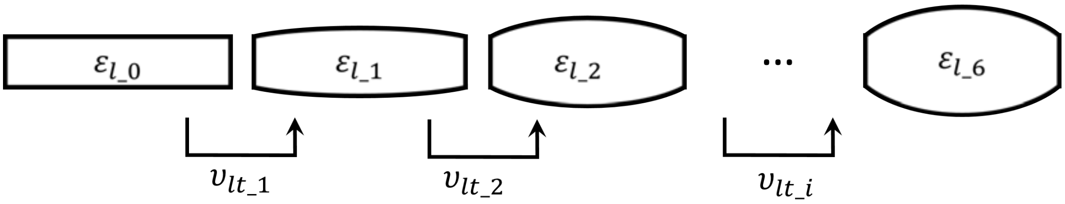

(a) Since the increment of ε_l in each stage is limited, υ_{lt_i} are assumed to be constants

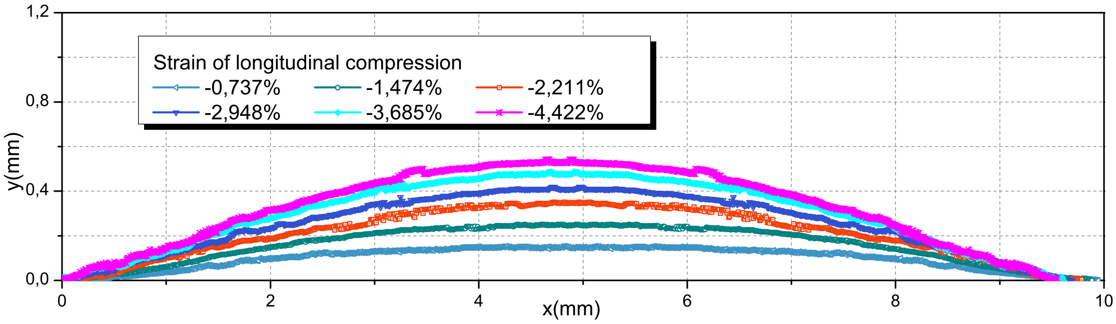

(b) The experimental expansion shapes at the end of each stage

FIGURE 3.32 – The compression process is discretized into small stages

Since the largest compression is -4.422%, the discretization is as follows :

$$
\begin{aligned}
&\varepsilon_{l\_0} = 0 \\
&\varepsilon_{l\_1} = -0.737\%,\ \varepsilon_{l\_2} = -1.474\% \\
&\varepsilon_{l\_3} = -2.211\%,\ \varepsilon_{l\_4} = -2.948\% \\
&\varepsilon_{l\_5} = -3.685\%,\ \varepsilon_{l\_6} = -4.422\%
\end{aligned}
\tag{3.72}
$$

the $\Delta\varepsilon_l$ is so small that υ_{lt_i} could be treated as a constant in each stage. And the expansion shapes at the end of each stage are shown in FIG. 3.32b. Here is how these curves are used to get the υ_{lt_i} in each stage :

Step 1. The F.E. model for the yarn sample is established. The transverse displacements of its two ends are constrained to zero. Monitoring those black element nodes in the model (FIG. 3.33), the expanding shapes of the two boundaries ∂V^1_{FE} and ∂V^2_{FE} are

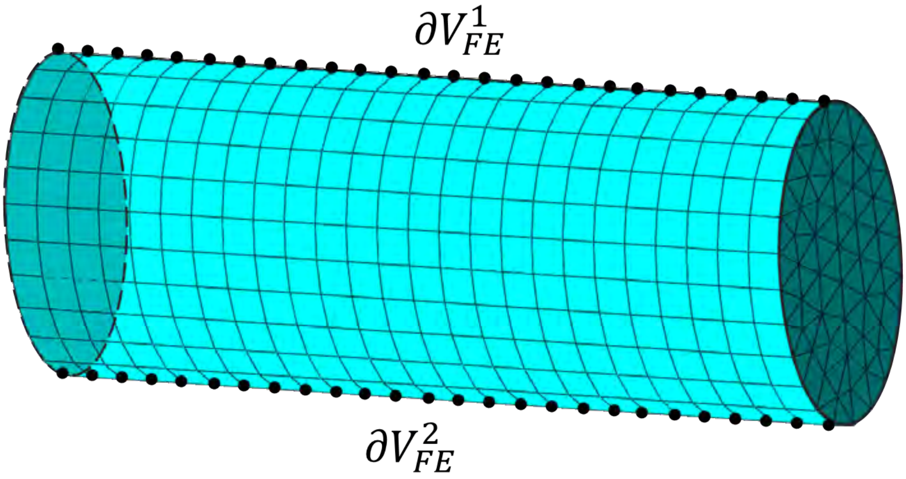

FIGURE 3.33 – The F.E. model for the yarn experiment

followed. The dimension of the model is completely the same with the experimental sample, and ∂V_{FE}^i corresponds to ∂V_{EXP}^i.

Step 2. The model is firstly compressed to the deformation state of $\varepsilon_{l\_1} = -0.737\%$. At the end of the compression, the coordinates of the nodes on ∂V_{FE}^1 and ∂V_{FE}^2 are extracted, and they are compared with the experiment curve (the curve of -0.737% in FIG. 3.32) in the Levenberg-Marquardt [LEV 44, MAR 63, SCH 92] inverse fitting program, in which υ_{lt} is updated. This process is repeated for several times until a good fitting is reached, as is shown in FIG. 3.34a, an expansion of the numerical model is close to the experiment result. The optimized υ_{lt} is 12.0065, and it is the optimized longitudinal-transverse Poisson ratio of the deformation from $\varepsilon_{l\_0} = 0$ to $\varepsilon_{l\_1} = -0.737\%$.

Step 3. The purpose of this step is to find out an optimized longitudinal-transverse Poisson ratio of the deformation from $\varepsilon_{l\_1} = -0.737\%$ to $\varepsilon_{l\_2} = -1.474\%$. Starting from the optimized expansion shape in last step, the yarn is further compressed to $\varepsilon_{l\_2} = -1.474\%$ (FIG. 3.34b). That is to say, the yarn is compressed from ε_{l_1} to ε_{l_2}. And the simulation is compared with the experiment curve (the curve of -1.474% in FIG. 3.32). The optimized υ_{lt} in this process is 11.8024, which is a little smaller than last compression step.

Step 4 $\sim$ Step 7. Similar with step 3, the yarn model is compressed from ε_{l_2} to ε_{l_3}, ε_{l_3} to ε_{l_4}, ε_{l_4} to ε_{l_5}, and finally, ε_{l_5} to ε_{l_6}. In each step an optimized υ_{lt} could be obtained. All the υ_{lt_i} are given in FIG. 3.34.

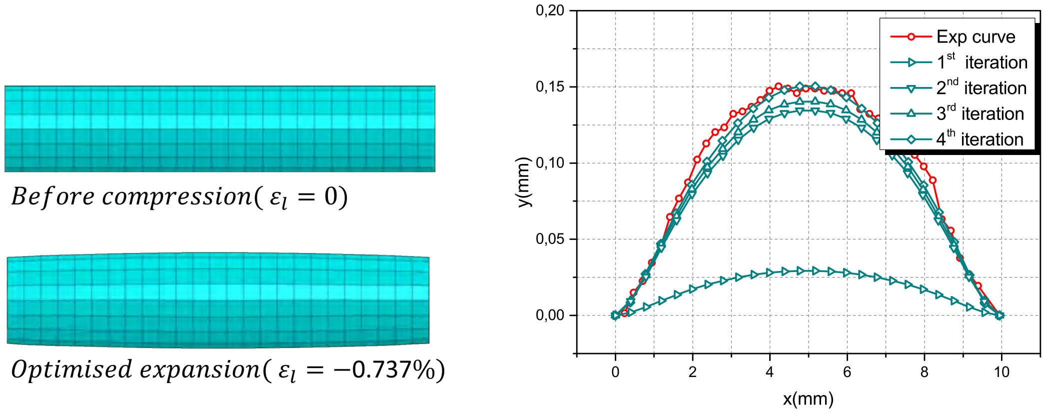

(a) From ε_{l_0} to ε_{l_1}

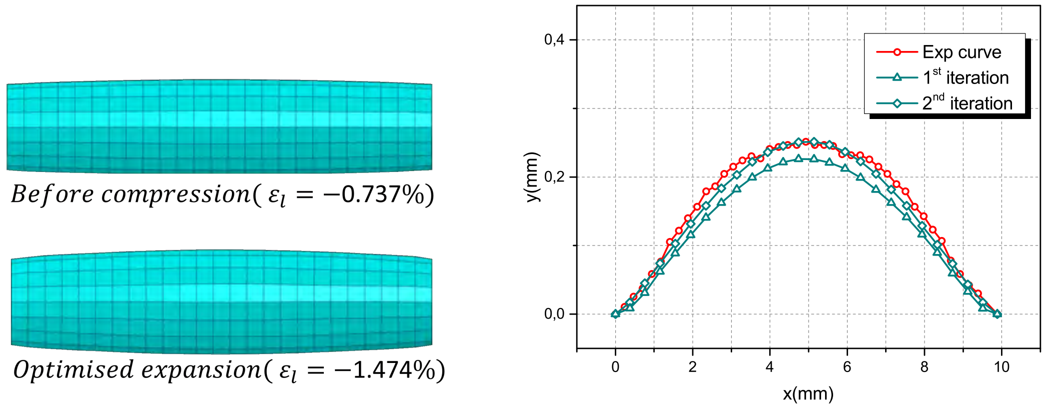

(b) From ε_{l_1} to ε_{l_2}

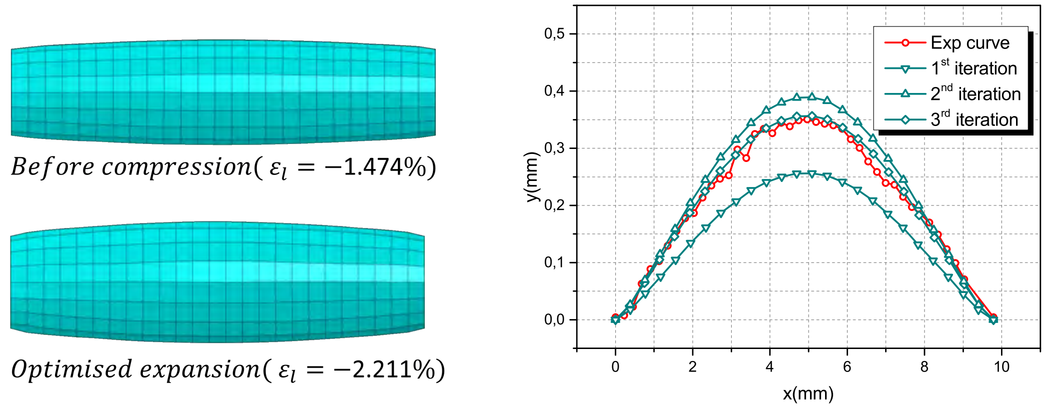

(c) From ε_{l_2} to ε_{l_3}

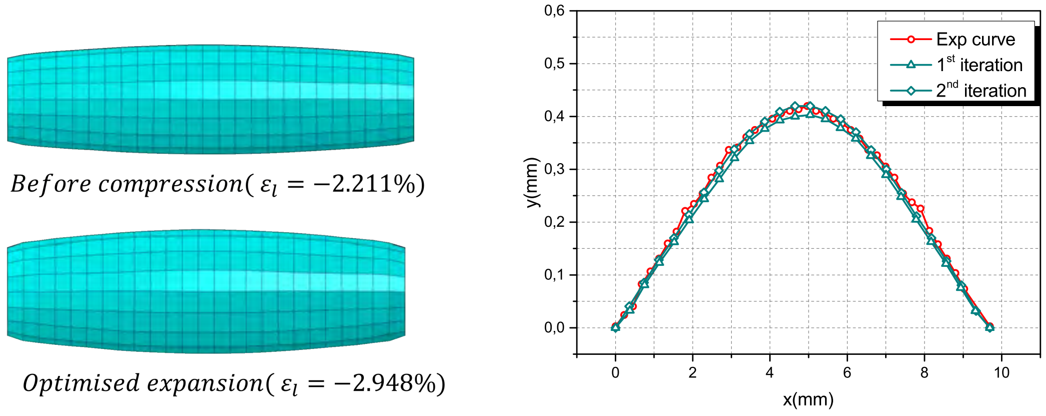

(a) From ε_{l_3} to ε_{l_4}

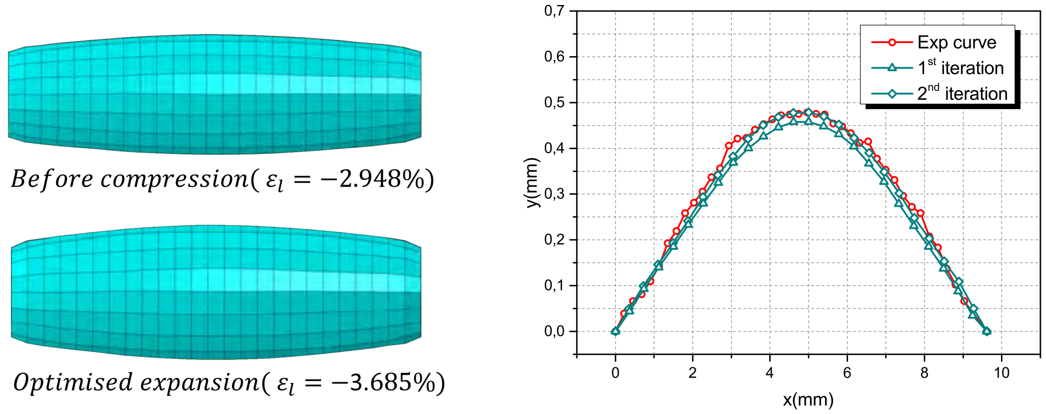

(b) From ε_{l_4} to ε_{l_5}

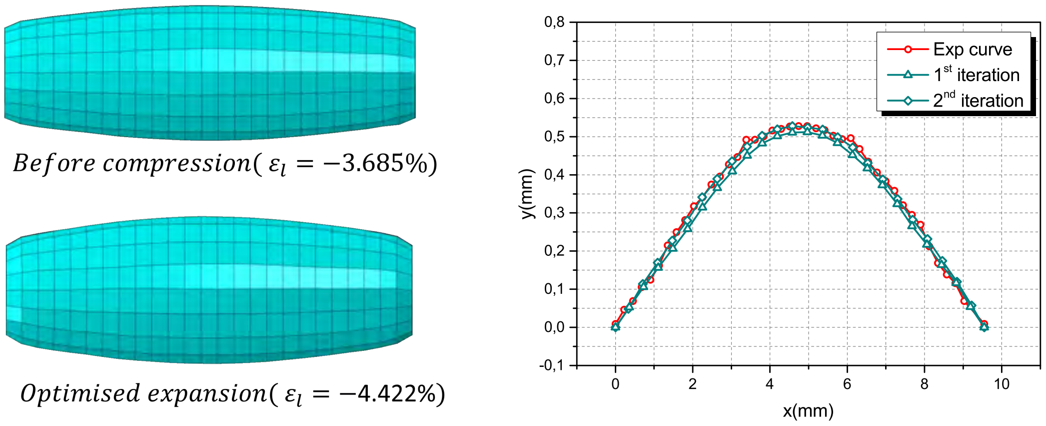

(c) From ε_{l_5} to ε_{l_6}

FIGURE 3.33 – The optimisation for υ_{lt} from $\varepsilon_l = 0$ to $\varepsilon_l = \varepsilon_{l\_6}$

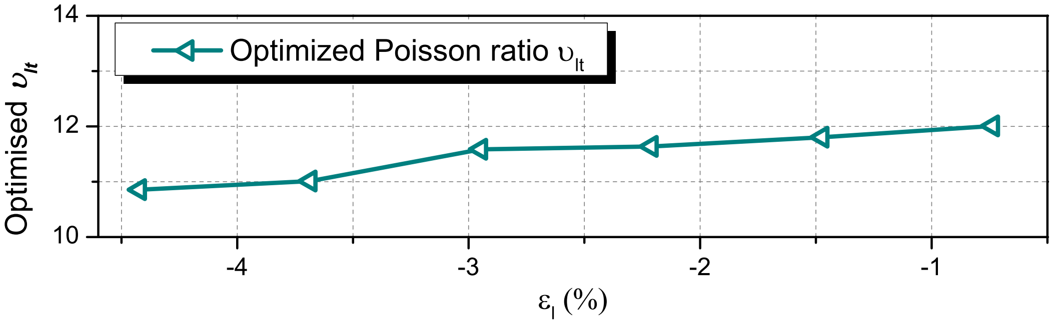

FIGURE 3.34 – υ_{lt} in each optimization step

All the optimized υ_{lt} from step 2 step 7 are listed in FIG. 3.34. There are several points worth noting :

1. The magnitude of υ_{lt} is around $11 \sim 12$, which is quite large. It is known that for the isotropic material, the Poisson ratio should smaller than 0.5.

   Here is a way to explain the rationality of this large Poisson ratio. When the yarn is compressed longitudinally, the fibers would bend or buckle, which leads to a large void ratio (FIG. 3.25). As a result, the yarn has almost no resistance to the transverse compression load, in other words, the E_t becomes null. As can be seen in EQ. (3.63), when E_t becomes null, υ_{lt} would be much larger than υ_{tl}.

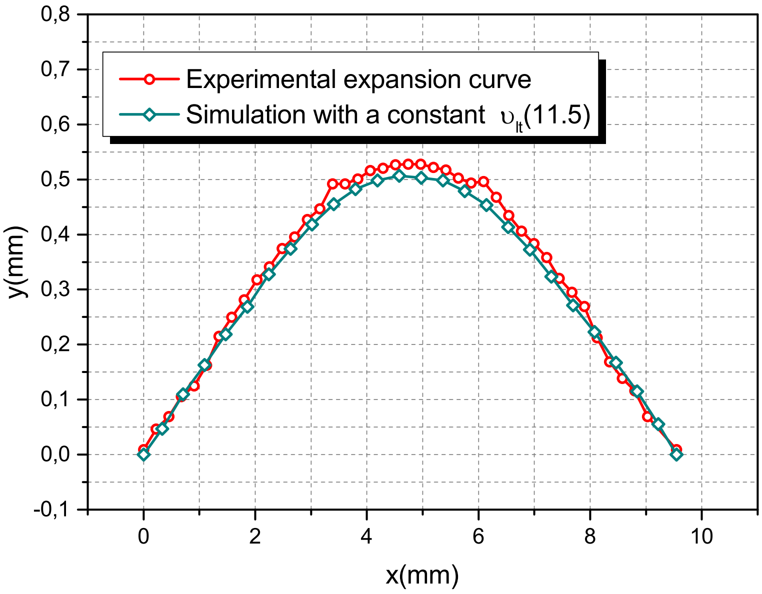

FIGURE 3.35 – υ_{lt} of a yarn could be considered as a constant

2. The fluctuation of the υ_{lt} curve in FIG. 3.34 is slight in the limited longitudinal compression range ($\varepsilon_l > -5\%$). So the υ_{lt} could be considered as constant during the compression. To verify this, a new simulation is performed. The yarn model in FIG. 3.33 is compressed from $\varepsilon_{l\_0} = 0$ to $\varepsilon_{l\_6} = -4.422\%$ with a constant υ_{lt} of 11.5 (it is the average value of υ_{lt_i} in FIG. 3.34), and the result is shown in FIG. 3.35. It is very close to the experimental expansion shape of the yarn. So the υ_{lt} for a yarn can be considered as a constant, nevertheless it remains to compare the υ_{lt} between different yarns.

Experiments on different yarn samples

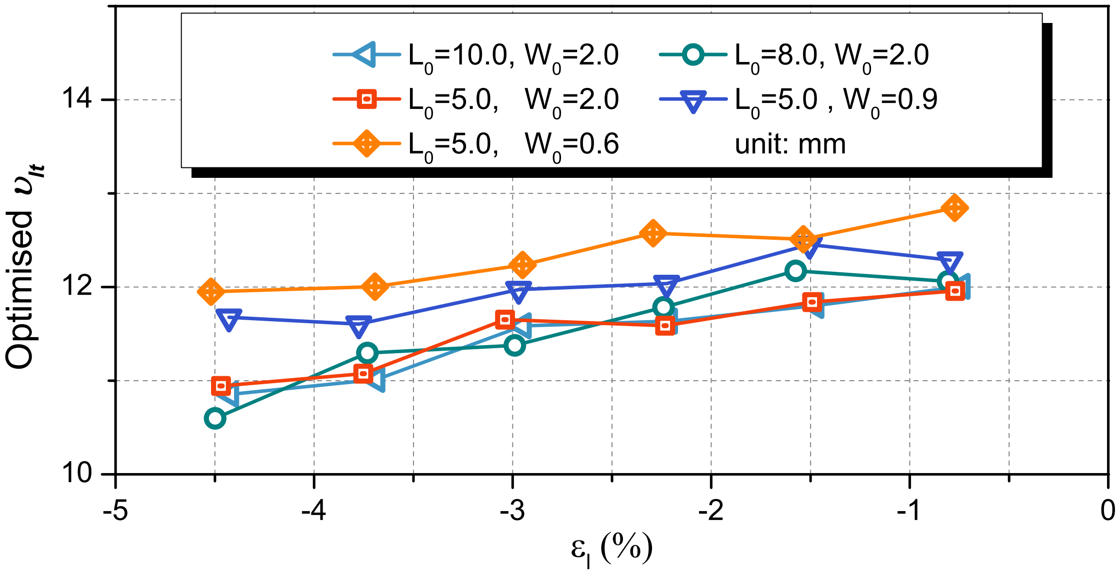

FIGURE 3.36 – The optimised υ_{lt} for different yarn samples

Repeating the above-introduced experiment and inverse fitting processes on different yarns, different curves of υ_{lt} are exhibited in FIG. 3.36. It seems that the L_0 has negligible influence on the evaluation of υ_{lt}, while the yarns with smaller sectional dimensions (W_0) tend to have larger values of υ_{lt}. Since these curves are quite close, it is interesting to study whether it is possible to chose the same value of υ_{lt} for all the yarns in tapas fabric. For this purpose, two simulations are carried out. The υ_{lt} are 11.8 and 13 respectively (11.8 is chosen because it it the average value of all the points in FIG. 3.36, and 13 it their upper limit). The two simulations are compared at different strain states, from $\varepsilon_l = -0.073\%$ to $\varepsilon_l = -4.422\%$ (FIG. 3.37). At the initial phase of the deformation, the difference is small, and it becomes larger when ε_l surpasses -2.948%. The difference when $\varepsilon_l = -4.422\%$ is about 0.037 mm in the middle of the yarn. In spite of this, the relative magnitude of this error is small since the corresponding expansion value is around 0.57 mm. So this error could be ignored and it is possible to use a value around 12 for υ_{lt} of all the yarns in tapas fabric.

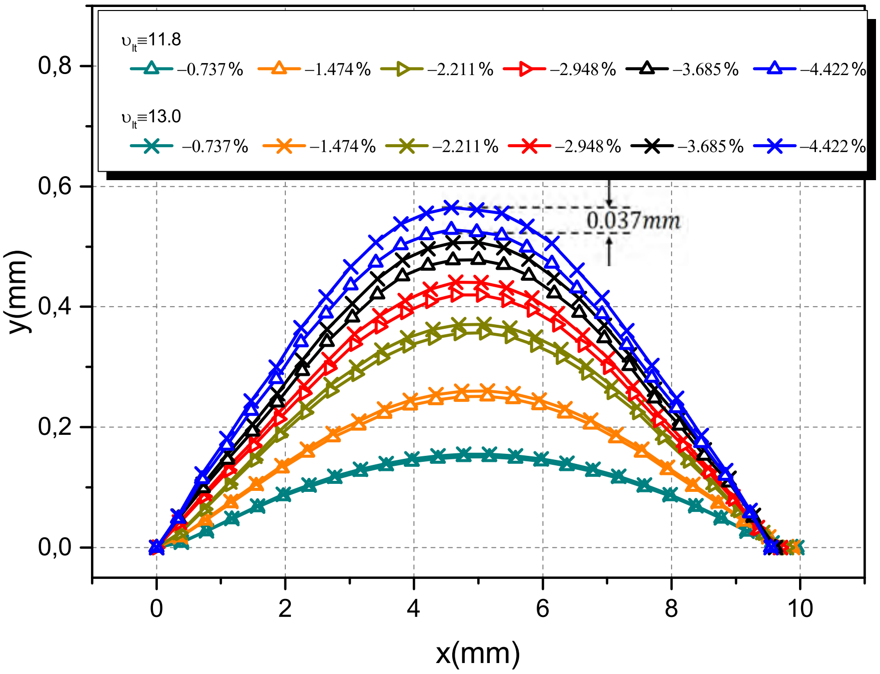

FIGURE 3.37 – Comparison between $\upsilon_{lt} = 11.8$ and $\upsilon_{lt} = 13$

3.4.3 Conclusion of transverse expansion mode

The transverse expansion of the yarn should be taken into account. In order to include this deformation phenomenon into the mesoscale model for the fibrous structure, the transverse expansion mode is developed based on υ_{lt}. It has been found that υ_{lt} is independent of the dimensions of the yarn, so υ_{lt} is isotropic in the cross section.

The compaction simulation of the tapas RUC is effectuated to verify the effect of transverse expansion mode 3.38b. The compaction ratio is 55.4%. Compared with the simulation result in which the transverse expansion is not considered, the shape of the new simulation result is closer : the binder yarn is similar to the one in tomography result in FIG. 3.26b, and yarns' transverse expansion minifies the voids between the yarns.

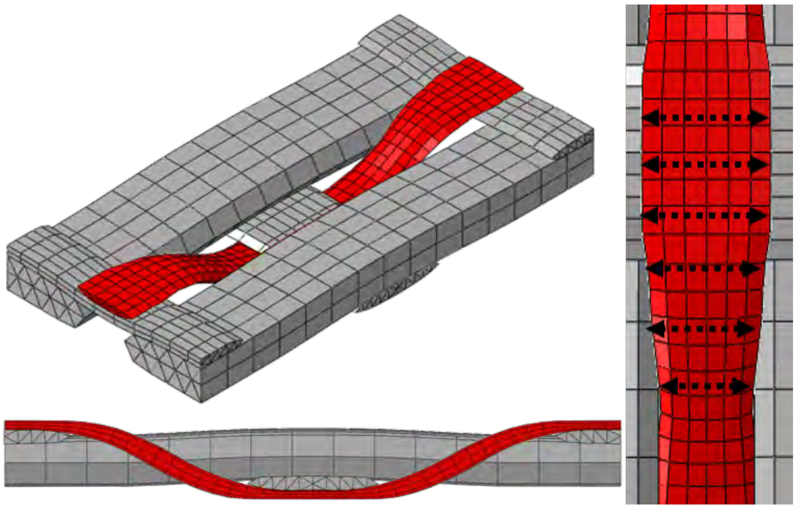

(a) Transverse expansion is not considered in the mechanical model

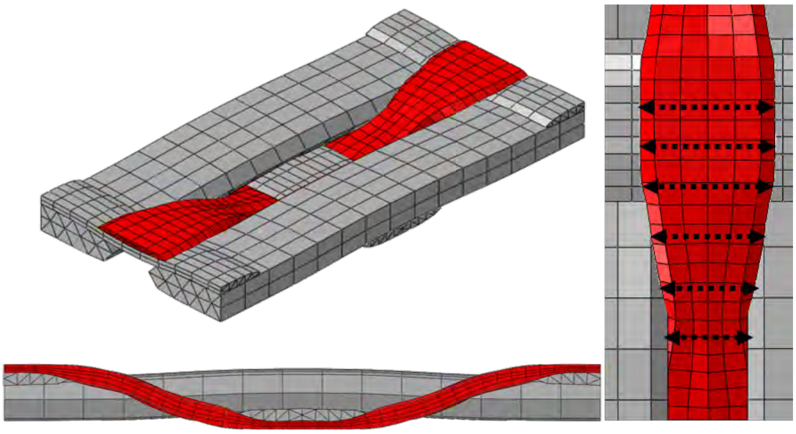

(b) Transverse expansion is added into the mechanical model, and $\upsilon_{lt} = 11.5$

FIGURE 3.38 – The effect of transverse expansion mode

3.5 Conclusions of chapter 3

Two kinds of new deformation modes are developed in this section and are added to the existed mesoscopic model.

Longitudinal compaction mode is quite helpful to eliminate the annoying numerical wrinkles on the longitudinally compressed yarns, and this thesis provides three possible strategies to make sure longitudinal compression is compatible with the elongation mode. Among them the 3^{rd} one in which a new strategy to update stress is developed is recommended since it has no influence on the simulation time.

The transverse expansion deformation mode concerns the expansion arises from the longitudinal compression. The study begins from an experimental observation, and an inverse fitting method is used to find out the appropriate value for υ_{lt}. It is found that a constant υ_{lt} is sufficient when the longitudinal compression is normally small (which is true for most deformations of tapas fabric).

Both of these modes improve the reliability of the simulation, which has been proved by tomography results. In the next chapter, more simulation results will be given on new/old model to further show the advantage of longitudinal compression and transverse expansion modes.

Chapitre 4

Numerical simulations

In this chapter, various numerical simulations are carried out on the numerical model of tapas fabric. In section 4.1, the transverse compaction simulation of single layer fabric is carried out on the previously proposed mesoscale model and the new mesoscale model developed in chapter 3. The simulation results are compared with the tomography data and the effectiveness of longitudinal compression mode and transverse expansion mode is verified. With that in mind, the rest of the simulations of chapter 4 are carried out with this improved mesoscale model. These simulations include the compaction of different tapas fabric stacks, the compaction of sheared tapas fabric, as well as the shear simulations. The numerical results are compared with the mechanical experiment results of chapter 1, or the tomography experiment results of chapter 2.

Contents

Transverse compaction deformation and in-plane shear deformation are two most important deformations for composite reinforcement, since they are the dominant deformation modes when the composite products are manufactured. In order to get a better understanding of the yarns' activities in the preforming process of the fabric, these two kinds of deformations should be studied by mechanical experiments, tomography experiments as well as numerical simulations. For the tapas fabric, the mechanical experiments (tension tests on tapas fabric and yarns, picture frame test, transverse compaction test, *etc.*) have been presented in details in chapter 1, and the tomography study of tapas fabric has been presented in chapter 2. In this chapter, different kinds of compaction and shear simulations are carried out, the parameters of the model for tapas fabric have been given in chapter 3. The numerical results will be compared with the results of mechanical experiments and tomography experiments.

4.1 Simulations of compaction

Compaction deformation of the fabric is one of the most important deformations in LCM process, and should be carefully simulated by numerical tools which help to monitor the deformation of yarns and predicting the permeability of the deformed fabric. The simulations in this section concern compaction simulations on various tapas fabric models.

First of all, the simulation on single layer tapas fabric is achieved on the mesoscale model proposed in the previous works and the new mesoscale model developed in chapter 3. Both of them will be compared with the tomography experiment result. The purpose of this work is to further verify the effectiveness of the two new deformation modes (longitudinal compression and transverse expansion). Then the simulations of compaction are performed on tapas fabric stacks, in which the composite fabric could be 0^o, 45^o or 90^o to each other. The compaction stiffness obtained in the simulations will be compared with the mechanical experiment results in chapter 1, moreover, the internal structures of the deformed fabric stacks in the simulations will be verified by tomography experiments. The third kind of compaction test is realized on the sheared fabric with different in-plane shear angles. The compaction stiffness obtained in the simulation will be verified by the corresponding experiments from chapter 1.

4.1.1 Compaction simulations of single layer fabric

The purpose of this simulation is to exhibit the effectiveness of the two deformation modes developed in chapter 3 (longitudinal compression deformation mode and transverse expansion deformation mode). The model in the simulation is a fabric model of $20.6mm \times 20.4mm$ (FIG. 4.1), which is generated by repeating the smallest RUC model in FIG. 2.9a from chapter 2. This model is meshed by wedge elements C3D6. Two rigid plates are defined over and below the fabric to compress the model transversely. In order to compared the simulation results with the tomography result, in which the compaction

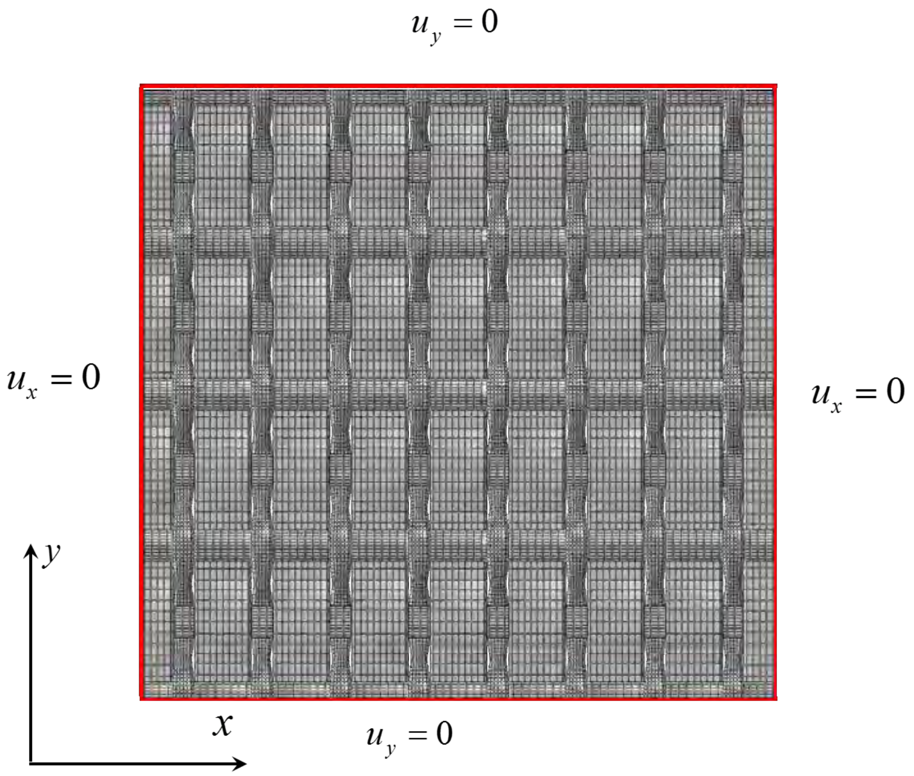

FIGURE 4.1 – The geometrical model of tapas fabric

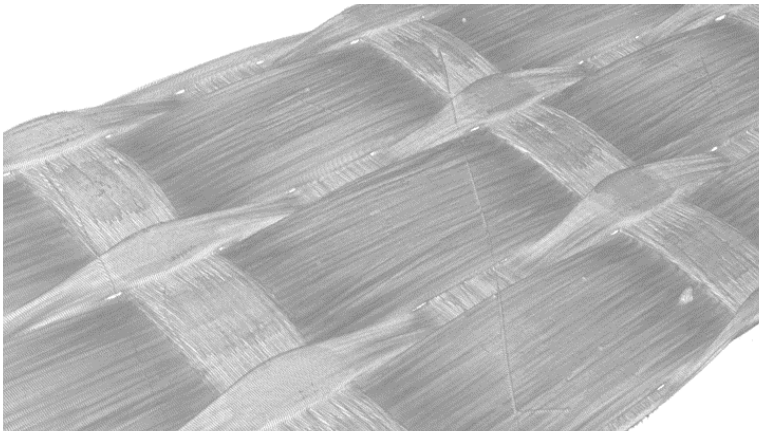

FIGURE 4.2 – The compacted tapas fabric observed in tomography experiment (compaction ratio is 55.4%)

ratio of tapas fabric is 55.4%, the compaction ratio of the fabric model in the simulation is also 55.4%. Three kinds of mechanical models are adopted in this simulation : the mesoscopic model proposed in previous works ; the model in which the longitudinal compression mode is considered ; and the model in which the longitudinal compression mode and transverse expansion deformation mode are considered.

1. Simulation with the mesoscale model proposed in previous works.

   The previously proposed mesoscopic model for textile structure considers four deformation modes of the yarn : elongation, longitudinal shear, transverse compaction and transverse shear deformation. The compaction simulation on the tapas fabric is firstly executed using this mechanical model.

   The result is shown in FIG. 4.3a. From a general point of view, this simulation result is close to the tomography observation (FIG. 4.2). However there are mainly two drawbacks : firstly, there are some spurious wrinkles in the simulation result, which cannot be found in the tomography image ; Secondly, comparing with the compacted tapas fabric observed in the tomography experiment, the transverse expansion of the yarns (especially the binder yarns) are not large enough in the simulation. For example, there is no voids between the binder yarns and warp yarns from the tomography result, however, some large voids exist in the simulation result. In fact these two kinds of defects are the same with those discovered in section 3.2.4.

2. <Longitudinal compression mode> is considered

   In chapter 3, the longitudinal compression deformation mode is developed to constrain the spurious wrinkles observed in the deformation simulations of composite fabric. Here this new mode is added to the previously proposed mesoscopic model, and this new model is applied in the compaction simulation of tapas fabric.

   The result is given in FIG. 4.3b. Comparing with simulation result on the previous mesoscale model 4.3a, the spurious wrinkles disappear, which implies that the new mode of longitudinal compression is efficient. However, comparing with the compacted tapas fabric observed in the tomography result, the voids between the yarns still exist.

3. Both <longitudinal compression mode> and <transverse expansion mode> are considered

   In chapter 3, another new deformation mode which is called transverse expansion deformation mode is constructed to describe the transverse expansion of the yarn under longitudinal compression. Now along with the longitudinal compression mode, it is added into the previously used mesoscopic mechanical model. The compaction simulation result on this improved mechanical model is displayed in FIG. 4.3c. Compared with the simulation result in FIG. 4.3b in which the transverse expansion is not considered, the expansion of yarns are larger and the voids between yarns become smaller. In a word, among the three simulation results in FIG. 4.3, the last one is closest to the compacted tapas fabric observed in the tomography test.

The compaction simulation of the tapas fabric is executed on three kinds of mechanical models separately. The analysis of the simulation results prove the effectiveness of the deformation modes of longitudinal compression and transverse expression. For this reason, the following simulations in this chapter will be performed on the mechanical

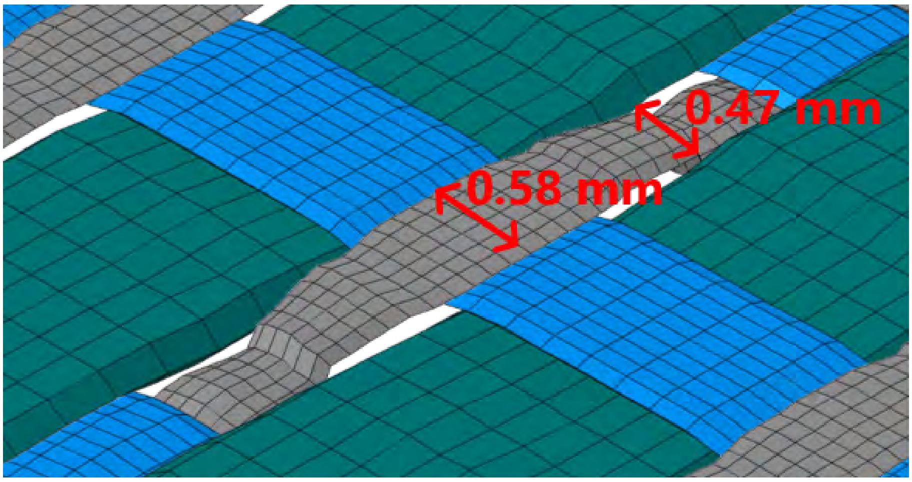

(a) The mesoscopic model used in the simulation is the one proposed in previous works

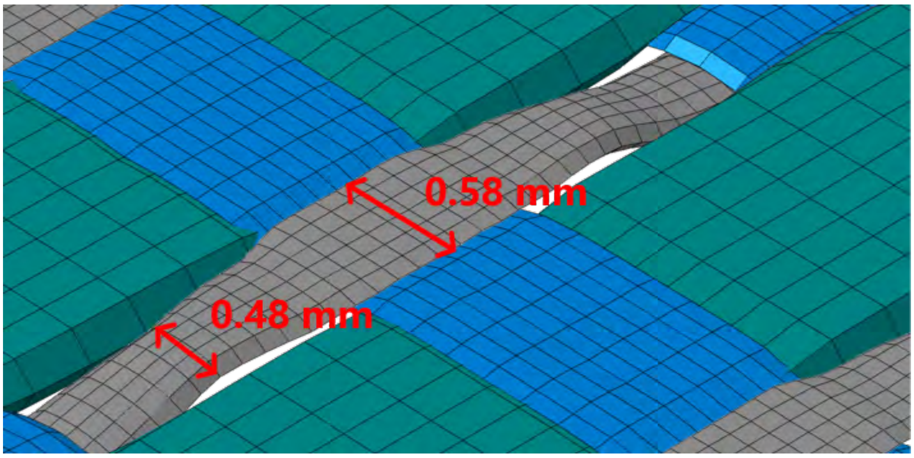

(b) The longitudinal compression mode is considered in the compaction simulation

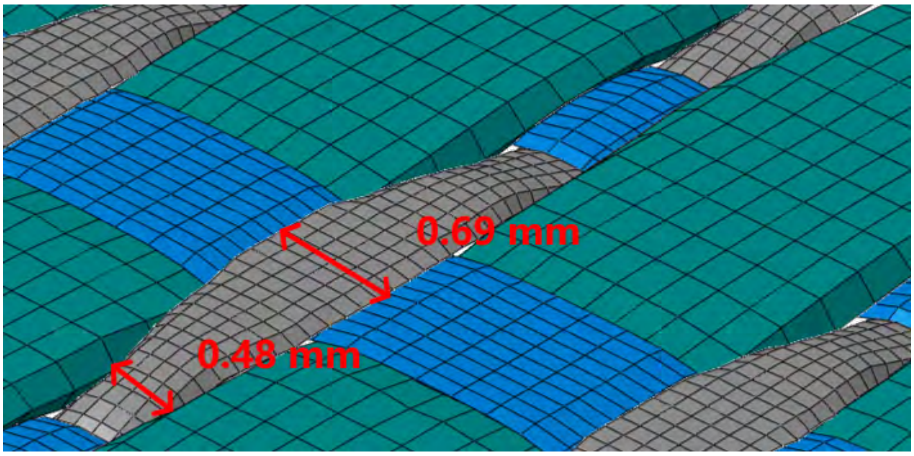

(c) Both the longitudinal compaction mode and transverse expansion mode are considered

FIGURE 4.3 – Three compaction simulations on tapas fabric with different mechanical models (compaction ratio is 55.4%)

model of *the model proposed in the previous works + longitudinal compression mode + transverse expansion mode*.

4.1.2 Compaction simulations of fabric stacks

In chapter 1, the compaction experiments of tapas stacks have been introduced, and in this section, the corresponding simulations will be executed. Special attention will be given to the nesting between fabrics. Considering that the layout of fabric stacks can be multiply, the compaction simulation on fabric stacks could be complex. Here three kinds of layouts will be considered.

1. Stack of $0^o/0^o/0^o/0^o/0^o$

   FIG. 4.4 gives two kind of layouts for the parallel stacks. The first one has the smallest nesting level while the second one has a large nesting level.

   The compaction results of the parallel tapas stacks is given in FIG. 4.5a. The layout with the small nesting level is stiffer than the experiment result while the second simulation result has a smaller compaction stiffness. This is reasonable since in the experiment, the five parallel layers are arranged randomly and the nesting should be at an average level. FIG. 4.5b shows the nesting of fabric in the stacks. The same nesting can be found in the tomography image and simulation results, which verifies the effectiveness of the simulation results.

2. Stack of $0^o/45^o/0^o/45^o/0^o$

   FIG. 4.6 gives the stack model of $0^o/45^o/0^o/45^o/0^o$. When the stack model is compressed transversely, the compaction area is octagonal. The simulation results is compared with the experimental compaction curve and an acceptable coincidence could be found.

   The nesting phenomenon of this 45^o stack can be observed in FIG. 4.7, from the tomography result and simulation result. As can be seen, they are quite close, and the nesting level of 45^o stack is smaller than it in the parallel stack (FIG. 4.5c). This explains why 45^o stack has a higher compaction stiffness.

3. Stack of $0^o/90^o/0^o/90^o/0^o$

   The stack model of $0^o/90^o/0^o/90^o/0^o$ is shown in FIG. 4.10a. The simulation results of compaction coincides well with the experiment stiffness curve, as is shown in FIG. 4.9a. Almost no nesting can be found in the tomography result in FIG. 4.9b, and this is very well reflected by the simulation (FIG. 4.9c). The low nesting level explains why this kind of tapas stack has the highest compaction stiffness.

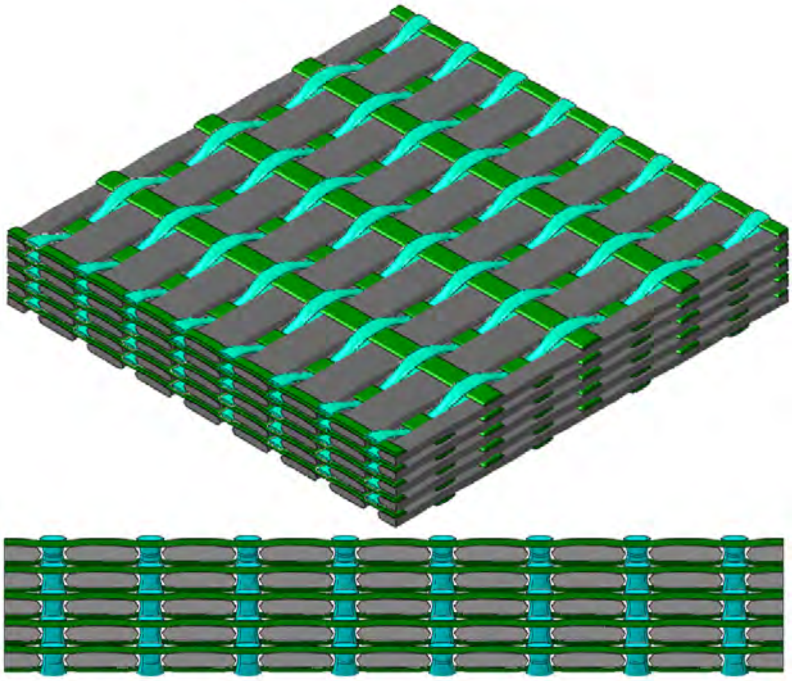

(a) Stack with small nesting

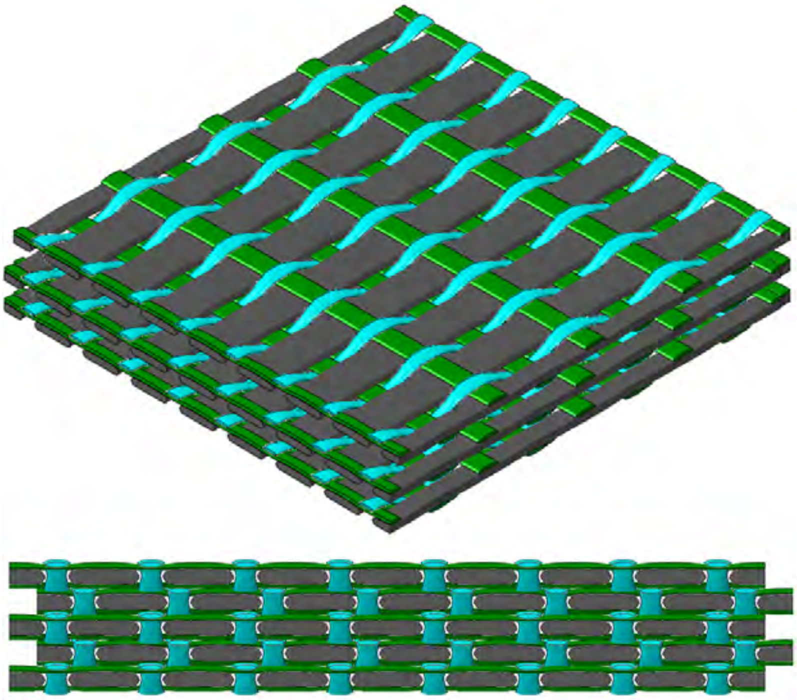

(b) Stack with large nesting

FIGURE 4.4 – The geometrical models for the tapas fabric stacks of $0^o/0^o/0^o/0^o/0^o$

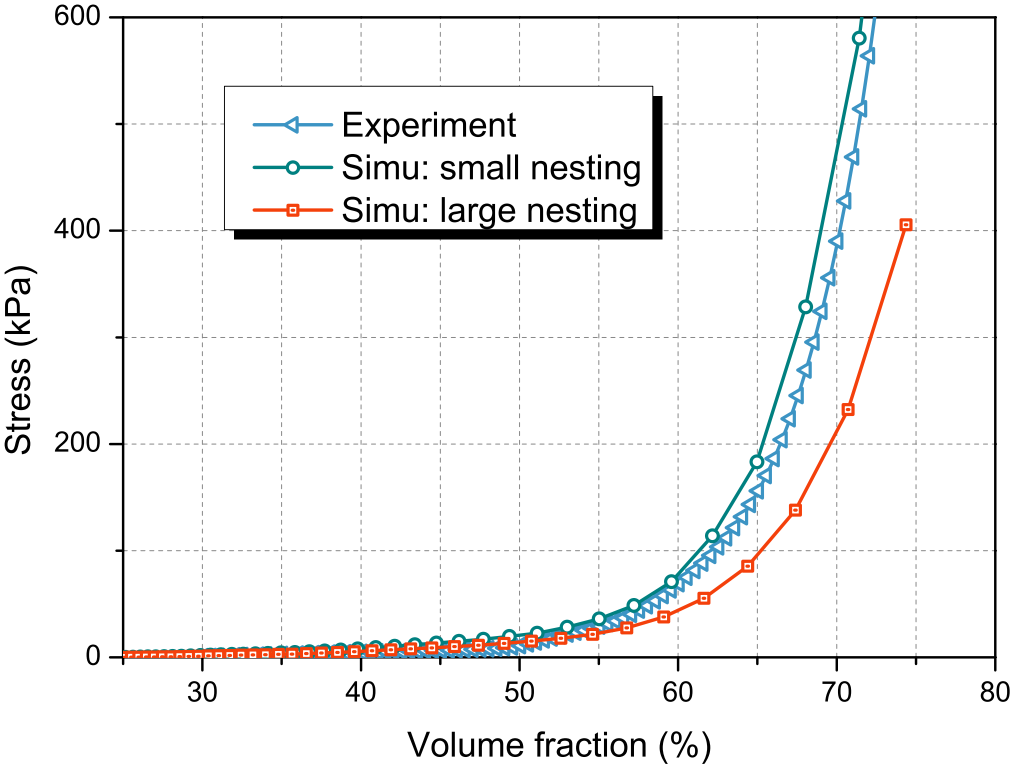

(a) Compaction stiffness curves from experiment and simulations

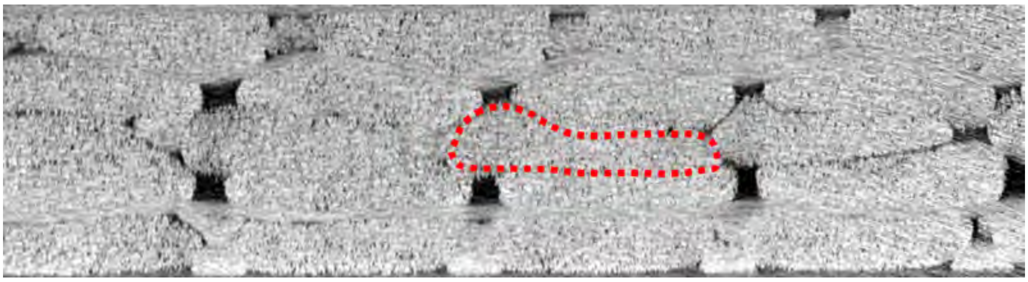

(b) Nesting observed in tomography experiment

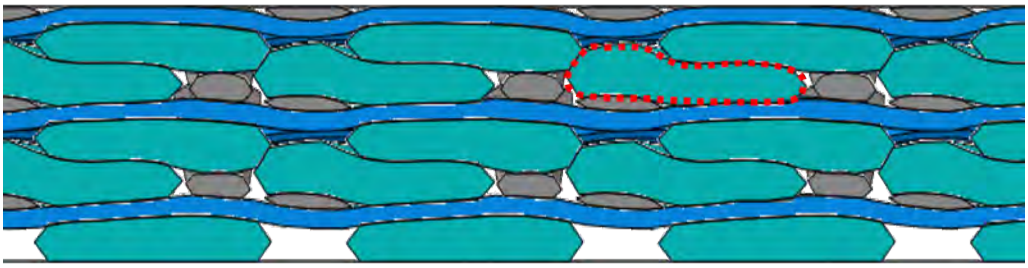

(c) Nesting observed in the simulation results

FIGURE 4.5 – Compaction simulations of tapas stacks of $0^o/0^o/0^o/0^o/0^o$

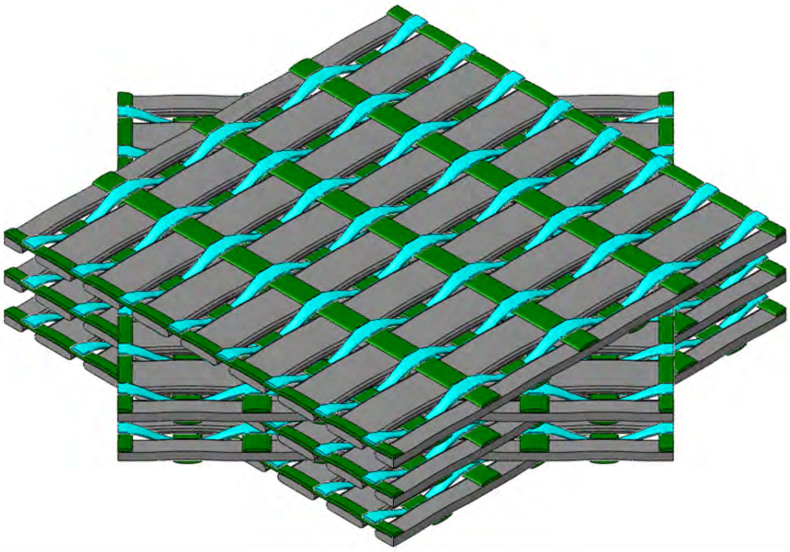

FIGURE 4.6 – The geometrical models for the tapas fabric stacks of $0^o/45^o/0^o/45^o/0^o$

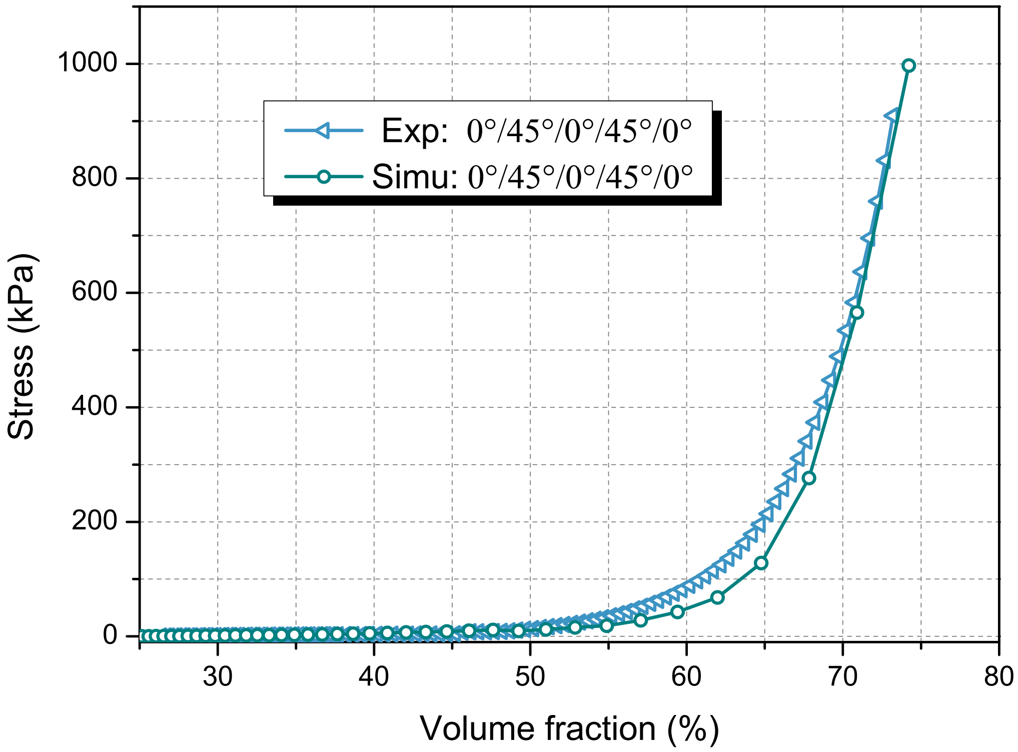

(**a**) Compaction stiffness curves from experiment and simulations

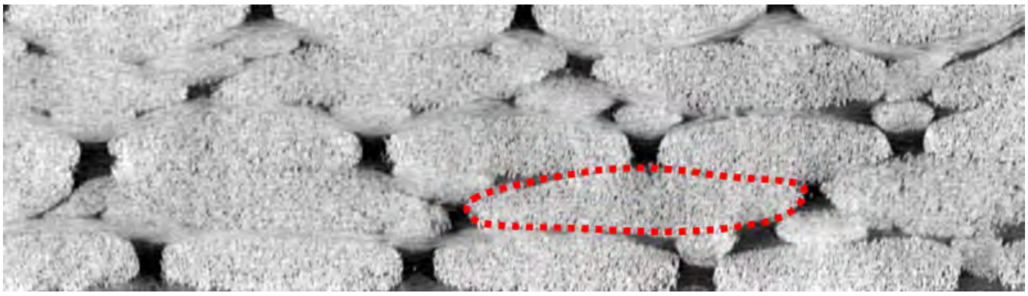

(**b**) Nesting observed in tomography experiment

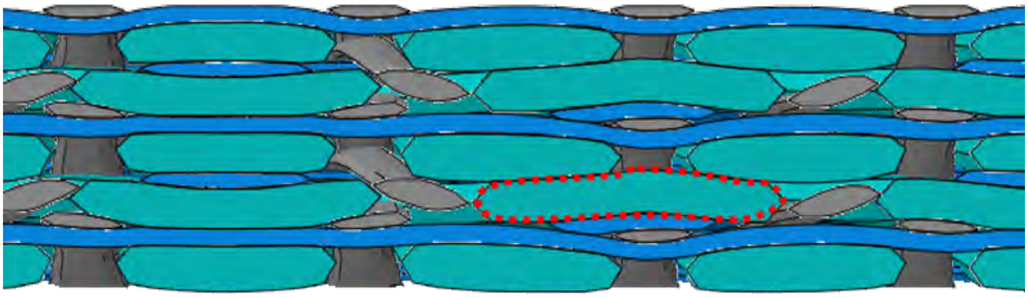

(**c**) Nesting observed in the simulation results

Figure 4.7 – Compaction simulations of tapas stacks of $0^o/45^o/0^o/45^o/0^o$

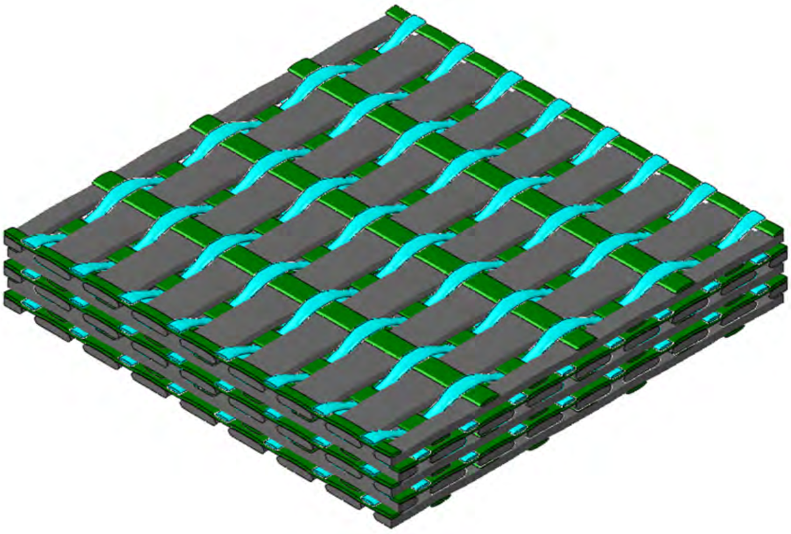

FIGURE 4.8 – The geometrical models for the tapas fabric stacks of $0^o/90^o/0^o/90^o/0^o$

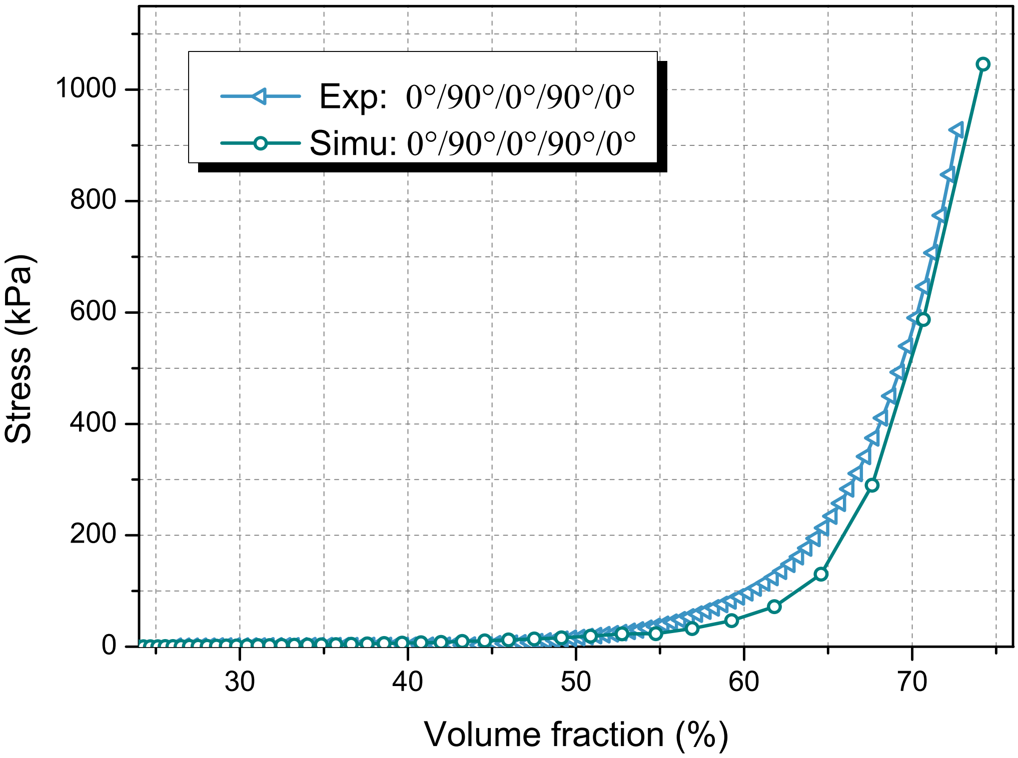

(a) Compaction stiffness curves from experiment and simulations

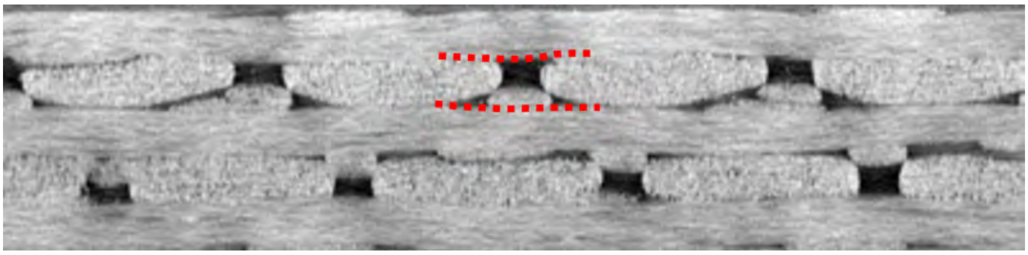

(b) Nesting observed in the tomography test

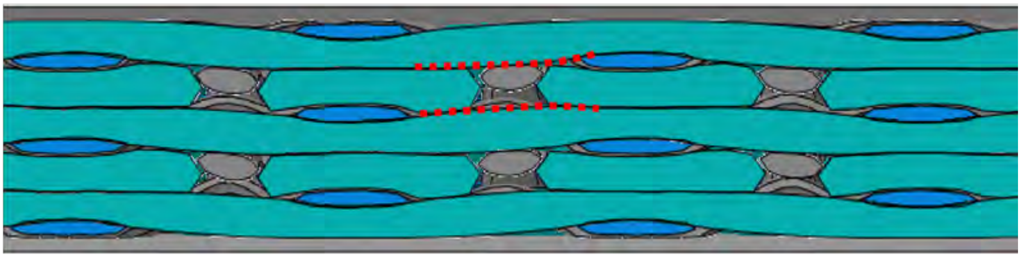

(c) Nesting observed in the simulation

FIGURE 4.9 – Compaction simulations of tapas stacks of $0^o/90^o/0^o/90^o/0^o$

4.1.3 Compaction simulations of sheared fabric

In-plane shear is a kind of common deformation for composite, so it is necessary to study compaction performance of sheared fabric (this simulation will be introduced in the next section). The model in FIG. 4.10b is obtained from a shear simulation (the shear angle is 16.7^o). The compaction ratio is 53.2%.

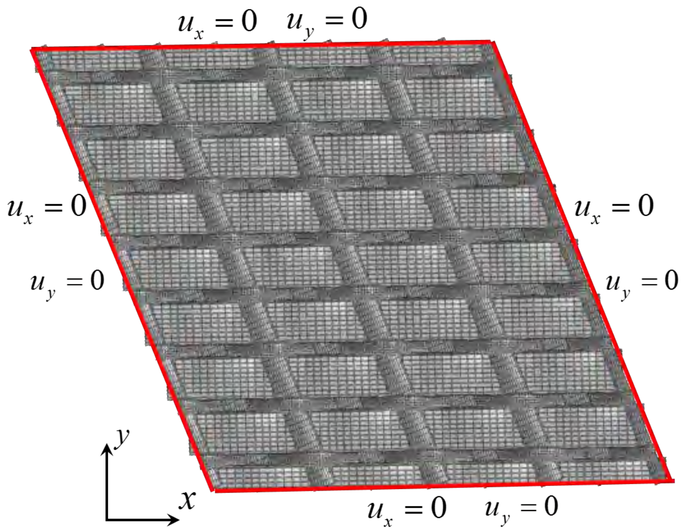

(a) Model of tapas with in-plane shear

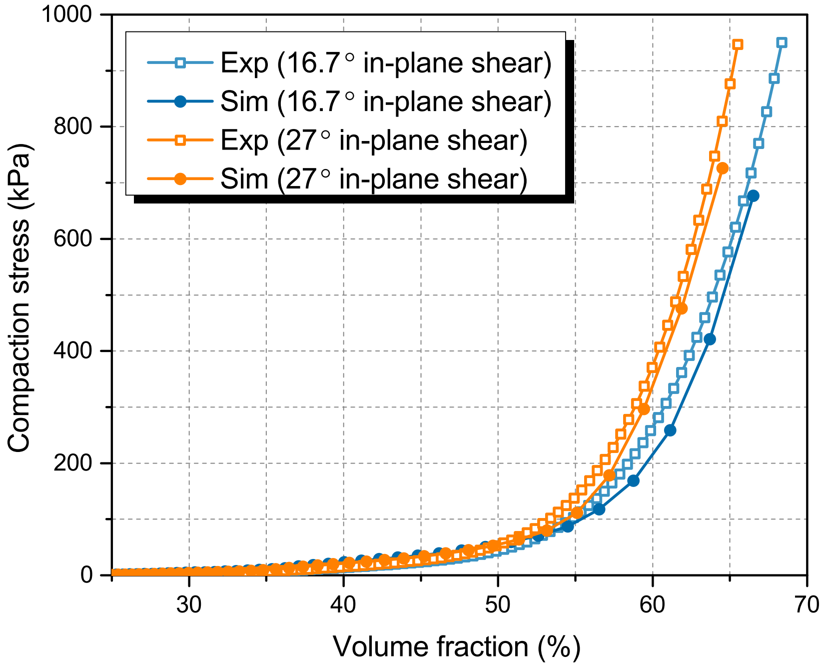

(b) Compaction stiffness curves from experiment and simulations

FIGURE 4.10 – Compaction simulations on tapas fabrics with in-plane shear deformation

4.2 Simulations of in-plane shear deformation

The importance of shear deformation cannot be over-emphasized. The shear tests (bias extension and picture frame test) on tapas fabric has been provided in chapter 1. In this section, shear deformation will be studied by numerical tools. Two models are applied to do the shear simulation of tapas fabric (FIG. 4.11) : the first model is the smallest RUC of tapas reinforcement, in which six pin-joint constrains are defined on the ends of the yarns ; the second geometrical model for the shear simulation is a fabric model, and pin joint constrains are also defined on the ends of each yarn. An example of the pin-joint constrain is shown in FIG. 4.11, as can be seen in FIG. 4.13a, all the nodes along the pin-joints could only rotate along the pin-joint axis.

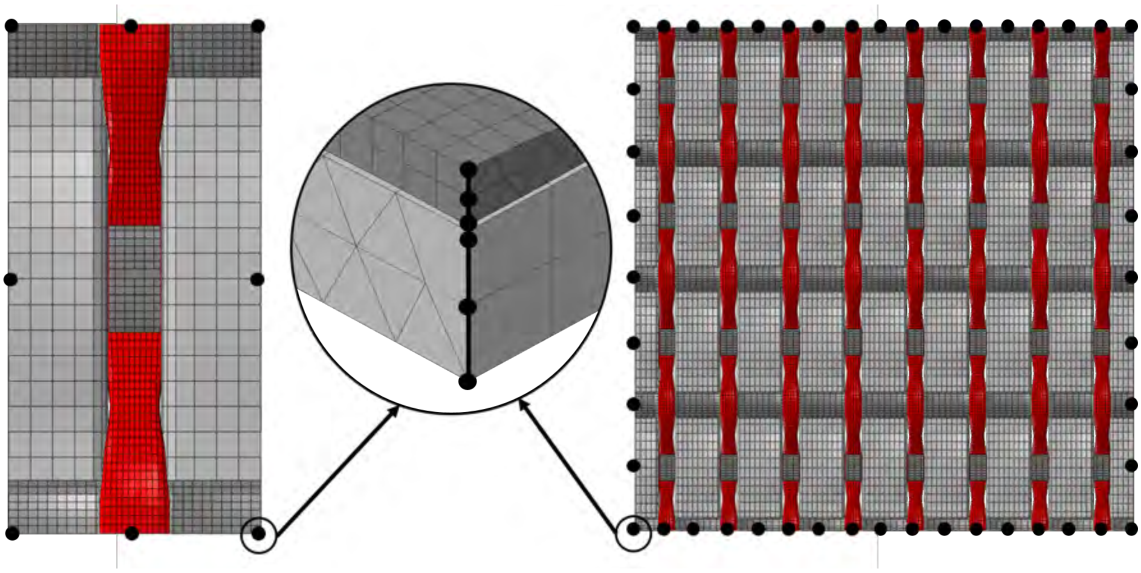

FIGURE 4.11 – Two goemetrical models for the shear simulation and their pin-joints boundary conditions

The shear happens in a bias extension test or picture frame test is pure shear, and for the pure shear deformation, the deformation gradient is homogeneous over the structure. According to this principle, the displacements of all the pin-joints in the two models are calculated, and defined in the two geometrical models as boundary condition. The simulation results will be discussed from the perspectives of shear stiffness and sheared geometry.

The shear stiffness of both simulations are shown in FIG. 4.12. The larger model get a better result than the small RUC model. The possible reason is that a smaller model is normally more sensitive to the defects of boundary conditions. For example, for both of these two geometrical models, when the shear angle becomes large, several parts of the yarns leave the geometric domain and become overhanging [BAD 07]. When the shear angle is large, the proportion of the overhanging parts are large for the small RUC model, however for the fabric model, the proportion of the overhanging parts is small comparing

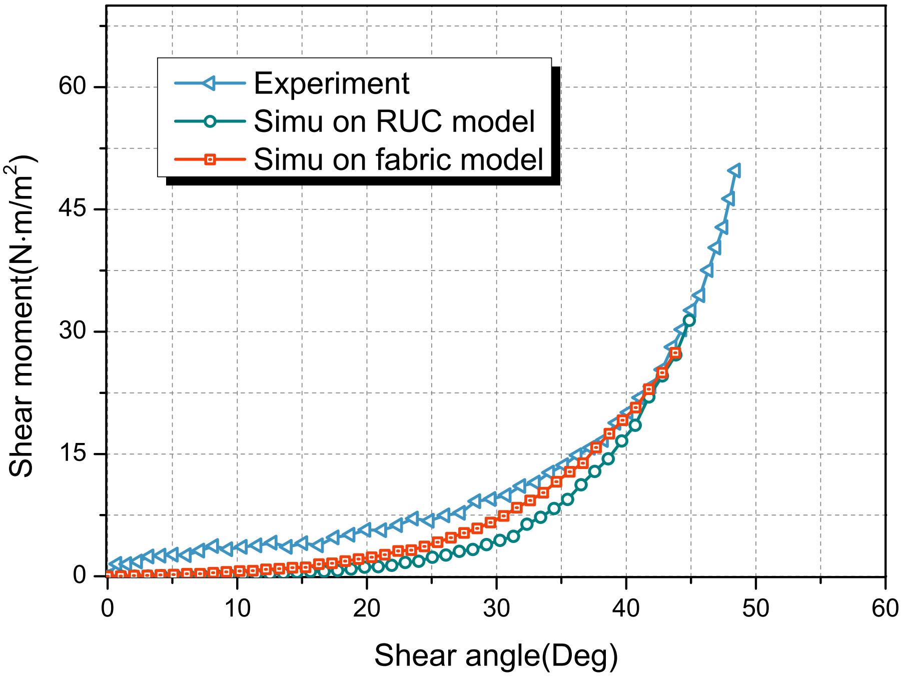

FIGURE 4.12 – Shear stiffness curves obtained from in-plane shear simulations on RUC and fabirc model

with its large surface area (FIG. 4.12).

The sheared geometries of the numerical simulations are shown in FIG. 4.12. Both models realize pure shear deformations. The deformations are homogeneous and close to the real shear deformation observed in the tomography result (FIG. 4.12). Nevertheless some defects exist. During the real shear deformation on tapas fabric, there are some specific deformation types concerning the yarns' discrete nature. For example, when the shear angle is large, the gaps inside the yarns will appear and some wrinkles on the surface of the yarns arise. These two kinds of deformation could not be reflected in the mesoscale simulations in which the yarns are considered as continuous medium.

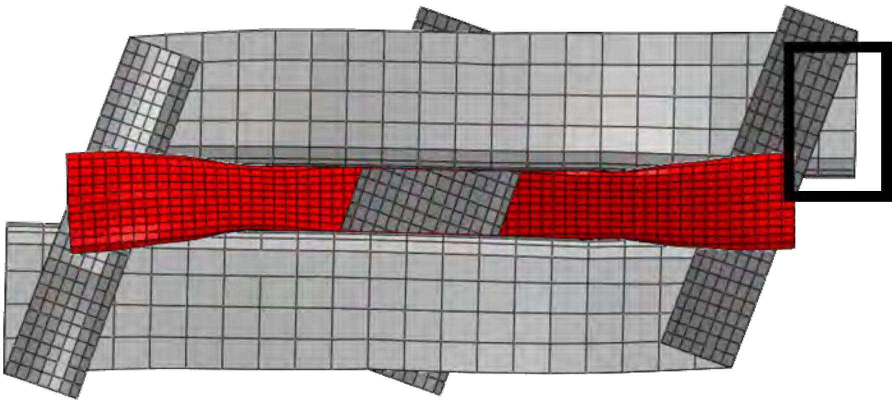

(a) The sheared RUC model

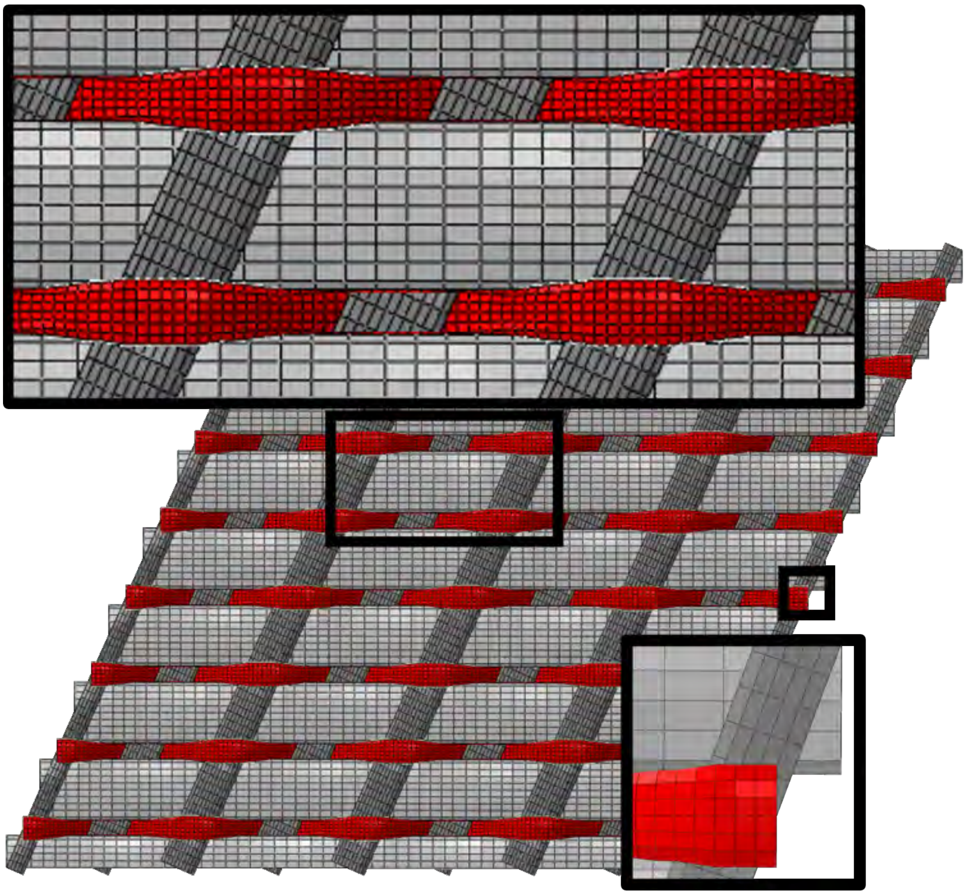

(a) The sheared fabric model

FIGURE 4.12 – The sheared models and the overhanging parts

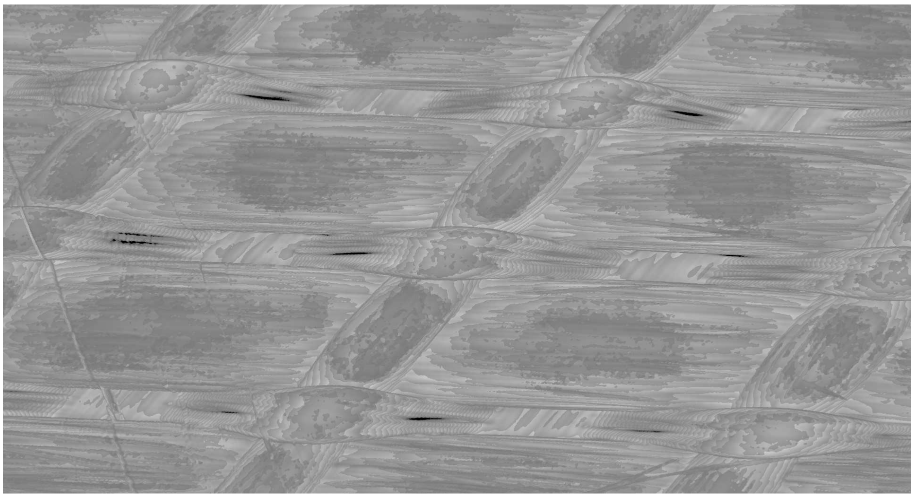

(a) Tapas fabric with a in-plane shear angle of 35.4^o

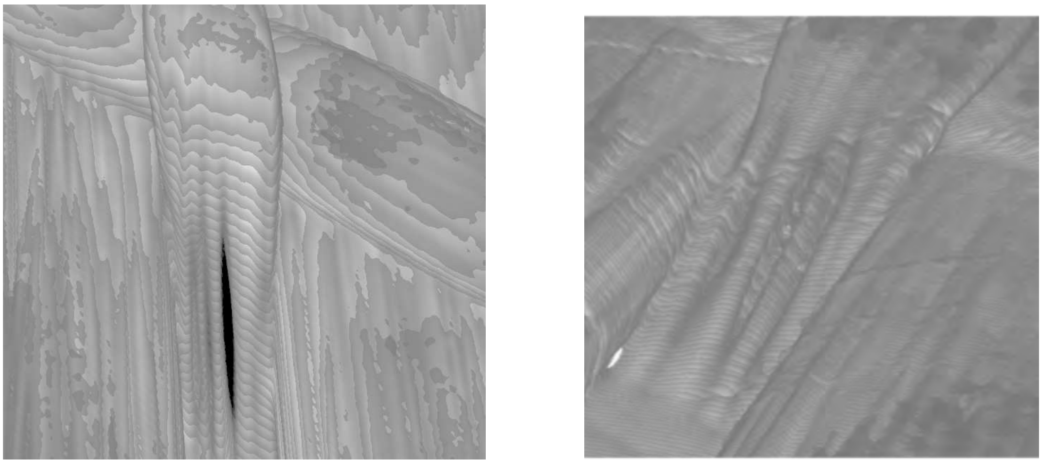

(a) The gaps inside the yarn **(b)** The wrinkles on the surface of the yarn

FIGURE 4.12 – The observation of the sheared tapas fabric with tomography technology

Chapitre 5

Conclusions and perspectives

Conclusions The mesoscopic mechanical model for the forming simulation of composite reinforcements has been developed for years, and its efficiency has been proved in previous research works. Nevertheless some aspects about the deformation of the yarn are not well considered in this model, in particular the longitudinal compression stiffness and the transverse expansion phenomenon. The consequence is that the forming simulations cannot accurately predict the deformation of reinforcements, *e.g.*, spurious wrinkles arise at the yarn level, and comparing with the physical deformation observed in the tomography results, the transverse expansion of the yarn in the simulation is not enough. To improve the mesoscopic model, new deformation modes are analyzed in this study.

The first one is longitudinal compression mode, which is used to distinguish the longitudinal compression stiffness with the elongation stiffness. The main difficulty is the stiffness gap problem, which is an incompatibility problem between the small longitudinal compression stiffness and the large elongation stiffness. Three strategies are provided to constrain this problem : restriction of the critical step increment, reduction of the stiffness gap magnitude by virtue of yarns' nonlinear tension parts, or the modification of stress updating strategy. The 3^{rd} one is recommended to be applied for the longitudinal compression model, since it is more efficient than the others. The second deformation mode is transverse expansion mode. It is a mode that could reflect the transverse expansion of the yarn when it is compression longitudinally. An experiment is designed to measure the expansion shape of the yarns, and combining with the inverse fitting process , the values of longitudinal-transverse Poisson ratio for different kinds of yarn samples are measured. It is finally found that this ratio could be considered as a constant around $11.5 \sim 13$ for all yarns in tapas fabric.

Perspectives Based on the above mentioned conclusions, and considering the deficiencies of the work in this study, additional investigations could be done in the future. They are summarized as follows :

- The simulations in this study are mainly transverse compaction simulations and shear simulations. It is expected to apply the new mechanical model on larger structures and more complex deformations. To do this, the execution efficiency of the F.E. loop must be improved (*e.g.*, it is possible to compare the simulation results of different element types and meshing densities).

- The study on the transverse expansion mode is based on the yarns in tapas fabric, in which the yarns are consist of glass fibers. It is interesting to study the same phenomenon on yarns made up of other glass fibers, carbon fibers or other materials.
- For the tapas fabric, macroscopic study is expected. This is because, although the mesosopic simulations help to study the yarn-level phenomenons of the tapas fabric, it is difficult to simulate the complete preforming process of a large fabric layer. Moreover, the microscopic study on tapas fabric would also be valuable to study the corresponding fiber-level deformation and damage, and so on.

Bibliographie

[ABB 51] ABBOTT N.
The Measurement of Stiffness in Textile Fabrics. *Textile Research Journal*, vol. 21, n° 6, 1951, p. 435–441, SAGE Publications.

[ADA 87] ADAMS K. L., REBENFELD L.
In-Plane Flow of Fluids in Fabrics : Structure/Flow Characterization. *Textile Research Journal*, vol. 57, n° 11, 1987, p. 647–654.

[ALL 11] ALLAOUI S., BOISSE P., CHATEL S., HAMILA N., HIVET G., SOULAT D., VIDAL-SALLE E.
Experimental and numerical analyses of textile reinforcement forming of a tetrahedral shape. *Composites Part A : Applied Science and Manufacturing*, vol. 42, n° 6, 2011, p. 612–622.

[AON 94] AONO M., BREEN D. E., WOZNY M. J.
Fitting a woven-cloth model to a curved surface : mapping algorithms. *Computer-Aided Design*, vol. 26, n° 4, 1994, p. 278–292.

[ARB 11] ARBTER R., BERAUD J., BINETRUY C., BIZET L., BRÉARD J., COMAS-CARDONA S., DEMARIA C., ENDRUWEIT A., ERMANNI P., GOMMER F., HASANOVIC S., HENRAT P., KLUNKER F., LAINE B., LAVANCHY S., LOMOV S., LONG A., MICHAUD V., MORREN G., RUIZ E., SOL H., TROCHU F., VERLEYE B., WIETGREFE M., WU W., ZIEGMANN G.
Experimental determination of the permeability of textiles : A benchmark exercise. *Composites Part A : Applied Science and Manufacturing*, vol. 42, n° 9, 2011, p. 1157–1168.

[BAD 07] BADEL P., VIDAL-SALLÉ E., BOISSE P.
Computational determination of in-plane shear mechanical behaviour of textile composite reinforcements. *Computational Materials Science*, vol. 40, n° 4, 2007, p. 439–448.

[BAD 08a] BADEL P., VIDAL-SALLÉ E., MAIRE E., BOISSE P.
Simulation and tomography analysis of textile composite reinforcement deformation at the mesoscopic scale. *Composites Science and Technology*, vol. 68, n° 12, 2008, p. 2433–2440.

[BAD 08b] BADEL P.
Mesoscopic analysis of the mechanical behavior of textile composite reinforcements - Validation with X-ray tomography. Thèse de doctorat, INSA DE LYON, 2008.

[BAD 08c] BADEL P., VIDAL-SALLÉ E., BOISSE P.
Large deformation analysis of fibrous materials using rate constitutive equations. *Computers & Structures*, vol. 86, n° 11-12, 2008, p. 1164–1175.

[BAD 09] BADEL P., GAUTHIER S., VIDAL-SALLÉ E., BOISSE P.
Rate constitutive equations for computational analyses of textile composite reinforcement mechanical behaviour during forming. *Composites Part A : Applied Science and Manufacturing*, vol. 40, n° 8, 2009, p. 997–1007.

[BAD 11] BADEL P.
X-ray tomography analysis of the mechanical behaviour of reinforcements in composites. BOISSE P., Ed., *Composite reinforcements for optimum performance*, Chapitre 18, p. 565-586 Elsevier, 2011.

[BAH 04] BAHEI-EL-DIN Y., RAJENDRAN A., ZIKRY M.
A micromechanical model for damage progression in woven composite systems. *International Journal of Solids and Structures*, vol. 41, n° 9-10, 2004, p. 2307–2330.

[BAR 00] BARUCHEL J., BUFFIERE J., MAIRE E., MERLE P., PEIX G.
X Ray Tomography in Material Science. HERMES science Publications, 2000.

[BAR 16] BARBAGALLO G., MADEO A., AZEHAF I., GIORGIO I., MORESTIN F., BOISSE P.
Bias extension test on an unbalanced woven composite reinforcement : Experiments and modeling via a second-gradient continuum approach. *Journal of Composite Materials*, vol. 60, 2016, p. 1–21.

[BEL 11] BEL S.
Analysis and simulation of NCF composite reinforcement preforming. Thèse de doctorat, INSA DE LYON, 2011.

[BIC 97] BICKERTON S., ŠIMÁČEK P., GUGLIELMI S. E., ADVANI S. G.
Investigation of draping and its effects on the mold filling process during manufacturing of a compound curved composite part. *Composites Part A : Applied Science and Manufacturing*, vol. 28, n° 9-10, 1997, p. 801–816.

[BIC 03] BICKERTON S., BUNTAIN M., SOMASHEKAR A.
The viscoelastic compression behavior of liquid composite molding preforms. *Composites Part A : Applied Science and Manufacturing*, vol. 34, n° 5, 2003, p. 431–444.

[BIL 09] DE BILBAO E., SOULAT D., HIVET G., GASSER A.
Experimental Study of Bending Behaviour of Reinforcements. *Experimental Mechanics*, vol. 50, n° 3, 2009, p. 333–351.

[BIR 04] BIRT E. A., SMITH R. A.
A review of NDE methods for porosity measurement in fibre-reinforced polymer composites. *Insight - Non-Destructive Testing and Condition Monitoring*, vol. 46, n° 11, 2004, p. 681–686.

[BIR 13] BIRCH S.
. « BMW i3, the inside story : what it is made of, how it is made ». `http://articles.sae.org/12056/`, 2013.

[BOI 04] BOISSE P.
Mise en forme des renforts fibreux de composites. *TECHNIQUES DE L'INGENIEUR*, vol. AM 3734, n° AM 3734, 2004, page 10.

[BOI 05a] BOISSE P., ZOUARI B., GASSER A.
A mesoscopic approach for the simulation of woven fibre composite forming. *Composites Science and Technology*, vol. 65, n° 3-4, 2005, p. 429–436.

[BOI 05b] BOISSE P., GASSER A., HAGEGE B., BILLOET J.-L.
Analysis of the mechanical behavior of woven fibrous material using virtual tests at the unit cell level. *Journal of Materials Science*, vol. 40, n° 22, 2005, p. 5955–5962.

[BOI 11] BOISSE P., HAMILA N., VIDAL-SALLÉ E., DUMONT F.
Simulation of wrinkling during textile composite reinforcement forming. Influence of tensile, in-plane shear and bending stiffnesses. *Composites Science and Technology*, vol. 71, n° 5, 2011, p. 683–692.

[BOR 99] BORGEFORS G., NYSTRÖM I., DI BAJA G. S.
Computing skeletons in three dimensions. *Pattern Recognition*, vol. 32, n° 7, 1999, p. 1225–1236, Pergamon.

[BUE 01] BUET-GAUTIER K., BOISSE P.
Experimental analysis and modeling of biaxial mechanical behavior of woven composite reinforcements. *Experimental Mechanics*, vol. 41, n° 3, 2001, p. 260–269.

[CAL 68] CALABI L., HARTNETT W.
Shape recognition, prairie fires, convex deficiencies and skeletons. *The American Mathematical Monthly*, vol. 75(4), 1968, p. 335–342.

[CAO 08] CAO J., AKKERMAN R., BOISSE P., CHEN J., CHENG H. S., DE GRAAF E. F., GORCZYCA J. L., HARRISON P., HIVET G., LAUNAY J., LEE W., LIU L., LOMOV S., LONG A., DE LUYCKER E., MORESTIN F., PADVOISKIS J., PENG X. Q., SHERWOOD J., STOILOVA T., TAO X. M., VERPOEST I., WILLEMS A., WIGGERS J., YU T. X., ZHU B.
Characterization of mechanical behavior of woven fabrics : Experimental methods and benchmark results. *Composites Part A : Applied Science and Manufacturing*, vol. 39, 2008, p. 1037–1053.

[CHA 11] CHARMETANT A., VIDAL-SALLÉ E., BOISSE P.
Hyperelastic modelling for mesoscopic analyses of composite reinforcements. *Composites Science and Technology*, vol. 71, n° 14, 2011, p. 1623–1631.

[CHA 12] CHARMETANT A., ORLIAC J., VIDAL-SALLÉ E., BOISSE P.
Hyperelastic model for large deformation analyses of 3D interlock composite preforms. *Composites Science and Technology*, vol. 72, n° 12, 2012, p. 1352–1360.

[CHE 93] CHEN A., MATTHEWS F.
A review of multiaxial/biaxial loading tests for composite materials. *Composites*, vol. 24, n° 5, 1993, p. 395–406.

[CIN 13] CINZIA T., CAROSENA M., MARIA C.
Porosity distribution in composite structures with infrared thermography. *Journal of Composites*, vol. 5, 2013.

[DAN 92] DANIEL I., WOOH S., KOMSKY I.
Quantitative porosity characterization of composite materials by means of ultrasonic attenuation measurements. *Journal of nondestructive evaluation*, vol. 5, 1992.

[DES 05] DESPLENTERE F., LOMOV S., WOERDEMAN D., VERPOEST I., WEVERS M., BOGDANOVICH A.
Micro-CT characterization of variability in 3D textile architecture. *Composites Science and Technology*, vol. 65, n° 13, 2005, p. 1920–1930.

[DOU 03] DOUMALIN P., BORNERT M., CRÉPIN J.
Characterisation of the strain distribution in heterogeneous materials. *Mécanique & Industries*, vol. 5, 2003.

[DUR 05] DURVILLE D.
Numerical simulation of entangled materials mechanical properties. *Journal of Materials Science*, vol. 40, n° 22, 2005, p. 5941–5948.

[DUR 10] DURVILLE D.
Simulation of the mechanical behaviour of woven fabrics at the scale of fibers. *International Journal of Material Forming*, vol. 3, n° S2, 2010, p. 1241–1251.

[DUR 11] DURVILLE D.
Microscopic approaches for understanding the mechanical behaviour of reinforcements in composites. BOISSE P., Ed., *Composite reinforcements for optimum performance*, Chapitre 15, p. 461-485 Elsevier, 2011.

[DUR 12] DURVILLE D.
Contact-friction modeling within elastic beam assemblies : an application to knot tightening. *Computational Mechanics*, vol. 49(6), 2012, p. 687–707.

[EBE 97] EBERHARDT B., WEBER A.
Modeling the Draping Behavior of Woven Cloth. *MapleTech*, vol. 4, n° 2, 1997, p. 25–31.

[El 14] EL SAID B., GREEN S., HALLETT S. R.
Kinematic modelling of 3D woven fabric deformation for structural scale features. *Composites Part A : Applied Science and Manufacturing*, vol. 57, 2014, p. 95–107.

[FLO 13] FLORIMOND C.
Contributions à la modélisation mécanique du comportement de mèches de renforts tissés à l'aide d'un schéma éléments finis implicite. Thèse de doctorat, INSA DE LYON, 2013.

[FRE 98] FREY P. J., BOROUCHAKI H.
Geometric surface mesh optimization. *Computing and Visualization in Science*, vol. 1, n° 3, 1998, p. 113–121, Springer-Verlag.

[GAV 13] GAVIN H. P.
The Levenberg-Marquardt method for nonlinear least squares curve-fitting problems. *Department of Civil and Environmental Engineering, Duke University*, vol. 5, 2013, p. 1–17.

[GOW 97] GOWAYED Y., YI L.
Mechanical behavior of textile composite materials using a hybrid finite element approach. *Polymer Composites*, vol. 18, n° 3, 1997, p. 313–319.

[GUZ 15] GUZMAN-MALDONADO E., HAMILA N., BOISSE P., BIKARD J.
Thermomechanical analysis, modelling and simulation of the forming of pre-impregnated thermoplastics composites. *Composites Part A : Applied Science and Manufacturing*, vol. 78, 2015, p. 211–222.

[HAA 14] HAANAPPEL S., AKKERMAN R.
Shear characterisation of uni-directional fibre reinforced thermoplastic melts by means of torsion. *Composites Part A : Applied Science and*, vol. 5, 2014.

[HAG 04] HAGEGE B.
Simulation du comportement mecanique des milieux fibreux en grandes transformations : application aux renforts tricotes. Thèse de doctorat, Ecole Nationale Superieure d'Arts et Metiers Centre de Paris, 2004.

[HAM 08] HAMILA N., BOISSE P.
Simulations of textile composite reinforcement draping using a new semi-discrete three node finite element. *Composites Part B : Engineering*, vol. 39, n° 6, 2008, p. 999–1010.

[HAM 09] HAMILA N., BOISSE P., SABOURIN F., BRUNET M.
A semi-discrete shell finite element for textile composite reinforcement forming simulation. *International Journal for Numerical Methods in Engineering*, vol. 79, n° 12, 2009, p. 1443–1466.

[HER 09] HERMAN G. T.
Fundamentals of Computerized Tomography. Advances in Pattern Recognition Springer London, London, 2009.

[HIN 96] HINTON M. J., SODEN P. D., KADDOUR A. S.
Strength of composite laminates under biaxial loads. *Applied Composite Materials*, vol. 3, n° 3, 1996, p. 151–162.

[HIV 05] HIVET G., BOISSE P.
Consistent 3D geometrical model of fabric elementary cell. Application to a meshing preprocessor for 3D finite element analysis. *Finite Elements in Analysis and Design*, vol. 42, n° 1, 2005, p. 25–49.

[HIV 08] HIVET G., BOISSE P.
Consistent mesoscopic mechanical behaviour model for woven composite reinforcements in biaxial tension. *Composites Part B : Engineering*, vol. 39, n° 2, 2008, p. 345–361.

[HSI 09] HSIEH J.
Computed tomography : principles, design, artifacts, and recent advances. SPIE Press, 1000 20th Street, Bellingham, WA 98227-0010 USA, oct 2009.

[HUG 80] HUGHES T. J. R., WINGET J.
Finite rotation effects in numerical integration of rate constitutive equations arising in large-deformation analysis. *International Journal for Numerical Methods in Engineering*, vol. 15, n° 12, 1980, p. 1862–1867.

[IVA 01] IVANOV I., TABIEI A.
Three-dimensional computational micro-mechanical model for woven fabric composites. *Composite Structures*, vol. 54, n° 4, 2001, p. 489–496.

[IVA 02] IVANOV I., TABIEI A.
Flexible Woven Fabric Micromechanical Material Model with Fiber Reorientation. *Mechanics of Advanced Materials and Structures*, vol. 9, n° 1, 2002, p. 37–51, Informa UK Ltd.

[JEU 08] JEULIN D., MOREAUD M.
Segmentation of 2D and 3D textures from estimates of the local orientation. *Image Analysis & Stereology*, vol. 27, n° 3, 2008, p. 183–192.

[KAS 10] KASTNER J.
. « Defect and Porosity Determination of Fibre Reinforced Polymers by X-ray Computed Tomography », 2010.

[KAW 73] KAWABATA S., NIWA M., KAWAI H.
3-The finite-deformation theory of plain-weave fabrics part I : the biaxial-deformation theory. *The Journal of The Textile Institute*, vol. 64, n° 1, 1973, p. 21–46, Taylor & Francis Group.

[KAW 08] KAWABATA S., NIWA M.
Fabric Performance in Clothing and Clothing Manufacture. *The Journal of The Textile Institute*, vol. 80, n° 1, 2008, p. 19–50, Taylor & Francis Group.

[KEL 11] KELLY P.
Transverse compression properties of composite reinforcements. BOISSE P., Ed., *Composite reinforcements for optimum performance*, Chapitre 11, p. 345-366 Elsevier, 2011.

[KHA 09] KHAN M. A.
Numerical and experimental forming analyses of textile composite reiforcements based on a hypoelastic behaviour. Thèse de doctorat, INSA DE LYON, 2009.

[KHA 10] KHAN M., MABROUKI T., VIDAL-SALLÉ E., BOISSE P.
Numerical and experimental analyses of woven composite reinforcement forming using a hypoelastic behaviour. Application to the double dome benchmark. *Journal of Materials Processing Technology*, vol. 210, n° 2, 2010, p. 378–388.

[LAD 06] LADEVÈZE P., LUBINEAU G., MARSAL D.
Towards a bridge between the micro- and mesomechanics of delamination for lami-

nated composites. *Composites Science and Technology*, vol. 66, n° 6, 2006, p. 698–712.

[LAT 11] LATIL P., ORGÉAS L., GEINDREAU C., DUMONT P., ROLLAND DU ROSCOAT S.
Towards the 3D in situ characterisation of deformation micro-mechanisms within a compressed bundle of fibres. *Composites Science and Technology*, vol. 71, n° 4, 2011, p. 480–488.

[LEV 44] LEVENBERG K.
A method for the solution of certain non-linear problems in least squares. *Quarterly of applied mathematics*, vol. 2, 1944, p. 164–168.

[LIA 14] LIANG B., HAMILA N., PEILLON M., BOISSE P.
Analysis of thermoplastic prepreg bending stiffness during manufacturing and of its influence on wrinkling simulations. *Composites Part A : Applied Science and Manufacturing*, vol. 67, 2014, p. 111–122.

[LIA 16] LIANG B.
Experimental and numerical study of the bending behaviour of textile reinforcements and thermoplastic prepregs. Thèse de doctorat, INSA DE LYON, 2016.

[LIN 08] LIN L., LUO M., TIAN H., LI X., GUO G.
Experimental investigation on porosity of carbon fiber-reinforced composite using ultrasonic attenuation coefficient. Citeseer, 2008.

[LOI 08] LOIX F., BADEL P., ORGÉAS L., GEINDREAU C., BOISSE P.
Woven fabric permeability : From textile deformation to fluid flow mesoscale simulations. *Composites Science and Technology*, vol. 68, n° 7-8, 2008, p. 1624–1630.

[LOM 03] LOMOV S., VERPOEST I., PEETERS T., ROOSE D.
Nesting in textile laminates : geometrical modelling of the laminate. *Composites Science and*, vol. 63(7), 2003, p. 993–1007.

[LOM 07] LOMOV S., IVANOV D., VERPOEST I., ZAKO M., KURASHIKI T., NAKAI H., HIROSAWA S.
Meso-FE modelling of textile composites : Road map, data flow and algorithms. *Composites Science and Technology*, vol. 67, n° 9, 2007, p. 1870–1891.

[LOM 11] LOMOV S.
Modelling the geometry of textile reinforcements for composites : WiseTex. BOISSE P., Ed., *Composite reinforcements for optimum performance*, Chapitre 7, p. 200-238 Elsevier, 2011.

[LON 11] LONG A., BROWN L.
Modelling the geometry of textile reinforcements for composites : TexGen. BOISSE P., Ed., *Composite reinforcements for optimum performance*, Chapitre 8, p. 239-264 Elsevier, 2011.

[LUN 95] LUNDBLAD W., DIXON C., OLHER H.
. « Bib », octobre 10 1995. U.S. Patent 5,456,974.

[LUO 99] LUO Y., VERPOEST I.
Compressibility and relaxation of a new sandwich textile preform for liquid composite molding. *Polymer composites*, vol. 20, 1999, p. 179–91.

[MAC 56] MACK C., TAYLOR H. M.
The fitting of woven cloth to surfaces. *Journal of the Textile Institute Transactions*, vol. 47, n^o 9, 1956, p. T477–T488, Taylor & Francis.

[MAI 14] MAIRE E., WITHERS P.
Quantitative X-ray tomography. *International materials reviews*, vol. 59, 2014, p. 1–43.

[MAR 63] MARQUARDT D.
An algorithm for least-squares estimation of nonlinear parameters. *Journal of the society for Industrial and Applied*, vol. 11 (2), 1963, p. 431–441.

[MAR 12] MARULIER C., DUMONT P., ORGÉAS L.
Towards 3D analysis of pulp fibre networks at the fibre and bond levels. *Nordic Pulp and*, vol. 27(2), 2012, page 245.

[MIA 08] MIAO Y., ZHOU E., WANG Y., CHEESEMAN B. A.
Mechanics of textile composites : Micro-geometry. *Composites Science and Technology*, vol. 68, n^o 7-8, 2008, p. 1671–1678.

[MIE 04] MIEHE C., DETTMAR J.
A framework for micro-macro transitions in periodic particle aggregates of granular materials. *Computer Methods in Applied Mechanics and Engineering*, vol. 193, n^o 3, 2004, p. 225–256.

[MIN 10] MINGALLON M.
. « FIBRE COMPOSITE ADAPTIVE SYSTEMS ». `http://fr.archello.com/en/project/fibre-composite-adaptive-systems/145965`, 2010.

[MOU 99] MOURITZ A., BANNISTER M., FALZON P., LEONG K.
Review of applications for advanced three-dimensional fibre textile composites. *Composites Part A : Applied Science and Manufacturing*, vol. 30, n^o 12, 1999, p. 1445–1461.

[NAO 14] NAOUAR N., VIDAL-SALLÉ E., SCHNEIDER J., MAIRE E., BOISSE P.
Meso-scale FE analyses of textile composite reinforcement deformation based on X-ray computed tomography. *Composite Structures*, vol. 116, 2014, p. 165–176.

[NAO 15a] NAOUAR N., VIDAL-SALLE E., SCHNEIDER J., MAIRE E., BOISSE P.
3D composite reinforcement meso F.E. analyses based on X-ray computed tomography. *Composite Structures*, vol. 132, 2015, p. 1094–1104.

[NAO 15b] NAOUAR N.
2D and 3D composite reinforcement meso F.E. analyses based on X-ray computed tomography. Thèse de doctorat, INSA DE LYON, 2015.

[NGU 12] NGUYEN Q. T.
Analyse experimentale et numerique de la compaction des renforts fibreux. Thèse de doctorat, INSA DE LYON, 2012.

[NGU 13] NGUYEN Q., VIDAL-SALLÉ E., BOISSE P., PARK C., SAOUAB A., BRÉARD J., HIVET G.
Mesoscopic scale analyses of textile composite reinforcement compaction. *Composites Part B : Engineering*, vol. 44, n^{o} 1, 2013, p. 231–241.

[PEN 02] PENG X., CAO J.
A dual homogenization and finite element approach for material characterization of textile composites. *Composites Part B : Engineering*, vol. 5, 2002.

[PEN 04] PENG X., CAO J., CHEN J., XUE P., LUSSIER D., LIU L.
Experimental and numerical analysis on normalization of picture frame tests for composite materials. *Composites Science and Technology*, vol. 64, n^{o} 1, 2004, p. 11–21.

[PIC 06] PICKETT A., FOUINNETEAU M.
Material characterisation and calibration of a meso-mechanical damage model for braid reinforced composites. *Composites Part A : Applied Science and Manufacturing*, vol. 37, n^{o} 2, 2006, p. 368–377.

[POT 01] POTLURI P., SHARMA S., RAMGULAM R.
Comprehensive drape modelling for moulding 3D textile preforms. *Composites Part A : Applied Science and Manufacturing*, vol. 32, n^{o} 10, 2001, p. 1415–1424.

[PRO 97] PRODROMOU A., CHEN J.
On the relationship between shear angle and wrinkling of textile composite preforms. *Composites Part A : Applied Science and Manufacturing*, vol. 28, n^{o} 5, 1997, p. 491–503.

[REZ 12] REZAKHANIHA R., AGIANNIOTIS A., SCHRAUWEN J. T. C., GRIFFA A., SAGE D., BOUTEN C. V. C., VAN DE VOSSE F. N., UNSER M., STERGIOPULOS N.
Experimental investigation of collagen waviness and orientation in the arterial adventitia using confocal laser scanning microscopy. *Biomechanics and modeling in mechanobiology*, vol. 11, n^{o} 3-4, 2012, p. 461–473.

[ROB 81] ROBERTSON R. E., HSIUE E. S., SICKAFUS E. N., YEH G. S. Y.
Fiber rearrangements during the molding of continuous fiber composites. I. Flat cloth to a hemisphere. *Polymer Composites*, vol. 2, n^{o} 3, 1981, p. 126–131.

[ROB 84] ROBERTSON R., HSIUE E., YEH G.
Continuous Fiber Rearrangements During The Molding Of Fiber Composites .2. Flat Cloth To A Rounded Cone. *Polymer Composites*, vol. 5, 1984.

[SAI 16] SAID B. E., IVANOV D., LONG A., HALLETT S.
Multi-scale modelling of strongly heterogeneous 3D composite structures using spatial Voronoi tessellation. *of the Mechanics and Physics of . . .*, vol. 88,, 2016, p. 50–71.

[SCH 92] SCHNUR D., ZABARAS N.
An inverse method for determining elastic material properties and a material interface. *Int. J. Numer. Methods Eng.*, vol. 33, 1992, p. 2039–2057.

[SLO 14] SLOAN J.
. « The making of the BMW i3 ». `http://www.compositesworld.com/blog/post/the-making-of-the-bmw-i3`, 2014.

[SON 03] SONG X.
Vacuum Assisted Resin Transfer Molding. Thèse de doctorat, Virginia Polytechnic Institute and State University, apr 2003.

[STO 99] STOCK S.
X-ray microtomography of materials. *International Materials Reviews*, vol. 44, 1999, p. 141–164.

[STO 08] STOCK S. R.
Recent advances in X-ray microtomography applied to materials. *International Materials Reviews*, vol. 53, n° 3, 2008, p. 129–181, Taylor & Francis.

[TAB 03] TABIEI A., IVANOV I.
Fiber Reorientation in Laminated and Woven Composites for Finite Element Simulations. *Journal of Thermoplastic Composite Materials*, vol. 16, n° 5, 2003, p. 457–474.

[TAB 14] TABATABAEI S., LOMOV S., VERPOEST I.
Assessment of embedded element technique in meso-FE modelling of fibre reinforced composites. *Composite Structures*, vol. 107, 2014, p. 436–46.

[TOS 13] TOSCANO C., MEOLA C., CARLOMAGNO G. M.
Porosity Distribution in Composite Structures with Infrared Thermography. *Journal of Composites*, vol. 2013, 2013, p. 1–8.

[Van 91] VAN DER WEEËN F.
Algorithms for draping fabrics on doubly-curved surfaces. *International Journal for Numerical Methods in Engineering*, vol. 31, n° 7, 1991, p. 1415–1426.

[VAN 96] VANDEURZEN P., IVENS J., VERPOEST I.
A three-dimensional micromechanical analysis of woven-fabric composites : II. Elastic analysis. *Composites Science and Technology*, vol. 56, n° 11, 1996, p. 1317–1327.

[VID 11] VIDAL-SALLÉ E.
Mesoscopic approaches for understanding the mechanical behaviour of reinforcements in composites. BOISSE P., Ed., *Composite reinforcements for optimum performance*, Chapitre 16, p. 486-523 Elsevier, 2011.

[WAL 12] WALBRAN W., VERLEYE B., BICKERTON S., KELLY P.
Prediction and experimental verification of normal stress distributions on mould tools during Liquid Composite Moulding. *Composites Part A : Applied Science and Manufacturing*, vol. 43, n° 1, 2012, p. 138–149.

[WAN 97] WANG C., SUN C.
Experimental characterization of constitutive models for PEEK thermoplastic composite at heating stage during forming. *Journal of composite materials*, vol. 5, 1997.

[WAN 12] WANG P., HAMILA N., PINEAU P., BOISSE P.
Thermomechanical analysis of thermoplastic composite prepregs using bias-extension test. *Journal of Thermoplastic Composite Materials*, vol. 5, 2012, page 0892705712454289.

[WEN 13] WENDLING A.
Simulation à l'échelle mésoscopique de la mise en forme de renforts de composites tissés. Thèse de doctorat, INSA DE LYON, 2013.

[WEN 14] WENDLING A., HIVET G., VIDAL-SALLÉ E., BOISSE P.
Consistent geometrical modelling of interlock fabrics. *Finite Elements in Analysis and Design*, vol. 90, 2014, p. 93–105.

[WEN 15] WENDLING A., DANIEL J. L., HIVET G., VIDAL-SALLÉ E., BOISSE P.
Meshing Preprocessor for the Mesoscopic 3D Finite Element Simulation of 2D and Interlock Fabric Deformation. *Applied Composite Materials*, vol. 22, n^o 6, 2015, p. 869–886, Springer Netherlands.

[WIL 08] WILLEMS A., LOMOV S., VERPOEST I.
Optical strain fields in shear and tensile testing of textile reinforcements. *Composites Science and*, vol. 68(3), 2008.

[XUE 03] XUE P., PENG X., CAO J.
A non-orthogonal constitutive model for characterizing woven composites. *Composites Part A : Applied Science and Manufacturing*, vol. 34, n^o 2, 2003, p. 183–193.

[YAN 14] YANG B., JIN T., BI F., LI J.
A Geometry Information Based Fishnet Algorithm for Woven Fabric Draping in Liquid Composite Molding. *Materials Science*, vol. 20, n^o 4, 2014, p. 513–521.

[YOU 05] YOUSSEF S., MAIRE E., GAERTNER R.
Finite element modelling of the actual structure of cellular materials determined by X-ray tomography. *Acta Materialia*, vol. 53, n^o 3, 2005, p. 719–730.

[YU 02] YU W. R., POURBOGHRAT F., CHUNG K., ZAMPALONI M., KANG T. J.
Non-orthogonal constitutive equation for woven fabric reinforced thermoplastic composites. *Composites Part A : Applied Science and Manufacturing*, vol. 33, n^o 8, 2002, p. 1095–1105.

FOLIO ADMINISTRATIF

THÈSE DE L'UNIVERSITÉ DE LYON OPÉRÉE AU SEIN DE L'INSA DE LYON

NOM : WANG DATE de SOUTENANCE : 03 Novembre 2016

Prénoms : Dawei

TITRE : MESOSCOPIC MODELING AND SIMULATION ON THE FORMING PROCESS OF TEXTILE COMPOSITE

NATURE : Doctorat Numéro d'ordre : 2016LYSEI108

École doctorale : MEGA

Spécialité : Mécanique - Génie Mécanique - Génie Civil

RÉSUMÉ :

Ce travail de thèse est consacré à l'étude des renforts textiles techniques 2D à l'échelle mésoscopique. La méthode des éléments finis est utilisée pour résoudre un problème aux limites, fortement non linéaire, dans le domaine du renfort fibreux. Deux nouveaux modes de déformations pour le comportement des mèches de renforts ont été développés et caractérisés. Le premier mode est la compression longitudinale, qui permet de traduire la faible rigidité des mèches lorsqu'elles subissent une dilatation négative dans le sens des fibres. La relation conflictuelle sur le plan numérique entre la rigidité en tension, très forte, et la rigidité en compression longitudinale, très faible, peut être résolue via trois méthodes : réduction du pas de temps critique, addition de la contribution en tension ou avec une nouvelle stratégie pour l'actualisation du champ de contrainte. Le second mode de déformation est la dilatation transversale des mèches considérée comme conséquence directe de la compression longitudinale. Ce phénomène d'expansion de matière dans les directions transverses peut être observé avec un essai de compression longitudinale in-situ sous tomographie X et est communément ignorer. Un protocole expérimental a été mise en place pour mesurer cette dilatation transversale des mèches et un coefficient de Poisson a pu être caractérisé par identification inverse. Une campagne expérimentale a permis d'identifier les paramètres matériau du modèle mésoscopique et les résultats de simulations sont comparés aux images issues d'essai mécanique in situ sous tomographe.

MOTS-CLÉS : Composites, renforts tissés, mise en forme, propriétés mécaniques, méthode par éléments finis, modélisation mésoscopique, hypoélasticité, tomographie, compression longitudinale, dilatation transversale

Laboratoire(s) de recherche : Laboratoire de Mécanique des Contacts et des Solides
UMR CNRS 5259 - INSA de Lyon
20, avenue Albert Einstein
69621 Villeurbanne Cedex FRANCE

Directeur de thèse : Philippe BOISSE

Composition du jury : Philippe BOISSE
Marie-Ange BUENO
Olivier POLIT
Francois BOUSSU
Naim NAOUAR
Emmanuelle Vidal-Sallé